University of Nevada, Reno

Oxidation Resistance Enhancement of Metallic Materials in Nuclear Reactors Environment

A dissertation submitted in partial fulfillment of the

requirements for the degree of Doctor of Philosophy in

Materials Science and Engineering

by

Jing Zhang

Dr. Qi An/Dissertation Advisor

December 2021

THE GRADUATE SCHOOL

We recommend that the dissertation
prepared under our supervision by

Jing Zhang

entitled

Oxidation Resistance Enhancement of Metallic Materials in Nuclear Reactors Environment

be accepted in partial fulfillment of the
requirements for the degree of

Doctor of Philosophy

Qi An

Advisor

Dhanesh Chandra

Committee Member

Bin Li

Committee Member

Leslie T. Mushongera

Committee Member

Yan Wang

Graduate School Representative

David W. Zeh, Ph.D., Dean
Graduate School

December, 2021

Abstract

The research in my dissertation aims at a better understanding of the corrosion mechanism of alloys applied in nuclear reactors and potential methods to enhance their corrosion resistance based on reliable computational simulations. First-principles based calculations and density functional theory (DFT) simulations are taken to investigate the chemical reaction between nuclear structural materials and corrosive coolants.

Zirconium (Zr) based cladding materials are widely used in commercial light water nuclear reactors and it is essential to prevent them from water oxidation to avoid serious safety issues in nuclear power plants such as Fukushima nuclear accident. To provide guidelines to design novel Zr alloys with enhanced water oxidation resistance, we performed a first-principles high-throughput screening (HTS) search that is based on the water dissociation mechanism over Zr basal plane. 53 metal dopants, including transition and non-transition metals, were selected to determine the promising dopants in Zr-X binary alloys with significantly improved resistance of water oxidation. Firstly, the adsorption and dissociation mechanisms of water molecules on the zirconium basal (0001) surface are determined using the density functional theory (DFT) calculations. Then the water dissociation barrier is used as a descriptor for the HTS approach. Next, the neutron cross-section is considered for the realistic applications of Zr-X alloys as cladding materials in nuclear reactions. Finally, the stability is checked for the possibility of processing these binary Zr-X alloys experimentally. Al, Zn, Ge, As, Sn, Sb, Pb, and Bi are singled out as promising dopants that could improve the corrosion resistance of zirconium alloys. In fact, aluminum alloys have already been used as fuel cladding, and

Zr alloys such as Zircaloy, ZIRLO, which contain 1% ~ 1.5% Sn, have been used as fuel cladding for PWRs and BWRs for decades.

Eutectic LiCl-KCl molten salt is often used in molten salt reactors as the primary coolant due to its high thermal capacity and high solubility of fission products. Thermophysical properties, such as density, heat capacity, and viscosity, are important parameters for engineering applications of molten salts, but may be significantly influenced by metal solute from corrosion of metallic structural materials. The behavior of the LiCl-KCl eutectic composition is well-researched, yet the effects on these properties due to chlorocomplex formation from metals dissolved in the salt are less well known. These properties are often difficult to accurately measure from experimental methods due to issues arising from the dissolved species such as volatility. Here we applied a combination of quantum mechanics molecular dynamics (QM-MD) and deep machine learning force field (DP-FF) molecular dynamics simulations to investigate the structure and thermophysical properties of LiCl-KCl eutectic as well as the influence of dissolved transition metal chlorocomplexes $NiCl_2$ and $CrCl_3$ at low concentrations. We find that the dissolution of Ni and Cr in the LiCl-KCl system forms the local tetrahedral $(NiCl_4)^{2-}$ and octahedral $(CrCl_6)^{3-}$ chlorocomplexes, respectively, which do not have a significant impact on the overall liquid salt structures. In addition, the thermodynamic properties including diffusion constant and specific heat capacity are not significantly affected by these chlorocomplexes. However, the viscosity is significantly changed in the temperature range of 673 ~ 773 K. This study thus provides essential information for evaluating the effects of dissolved metals on the thermophysical and transport properties of molten salts.

Acknowledgment

First and foremost, I would like to express my deepest gratitude to my advisor, Dr. Qi An, for his support and guidance throughout my Ph.D. study. He is very gentle and knowledgeable, he never likes to push me too much, but encourages me to learn how to do my research independently. He is patient with his students, whenever we have questions, he always explains everything clearly to us. I have enjoyed the discussion with him and was impressed with his knowledge in this field. This invaluable experience under his supervision will benefit my future academic research.

I also would like to thank Dr. Bin Li, Dr. Dhanesh Chandra, Dr. Leslie Mushongera, and Dr. Yan Wang, who are acknowledged for the help and valuable advice in my thesis, as well as for serving as the committee members.

I also would like to thank the current and former members of our group, who have helped me in the course study, research, and daily life, including Yidi Shen, Jon Fuller, Dezhou Guo, and Hongwei Wang.

Finally, I would like to thank my beloved family. Thanks for the unconditional and constant love from my parents. Thanks for the understanding and support from my husband, Mr. Yang Yang.

Table of Contents

List of Tables

List of Figures

Chapter 1. Introduction

1.1 Motivation

Energy is one of the most important issues that drive the development of modern technology and society. As a clean and sustainable energy source, nuclear energy has been studied since its first development in the 1960s. Nuclear power has been attracted more and more attention in recent years due to the high energy efficiency, sustainable and environmentally friendly features, and 20% of electricity generation in the United States comes from the nuclear power [2]. However, the safety issue of nuclear power plants remains to be the biggest concern. For example, nuclear accidents resulting from the corrosion of structure materials have a profound effect on the industry and our lives [3]. In order to provide guidelines on designing new alloys with better corrosion resistance, we study the corrosion behavior of these metallic materials in different conditions and improve their corrosion resistance using various theoretical approaches. Based on the nuclear reactors operating nowadays, my research is focusing on two nuclear power plants, light water nuclear reactors, and molten salt reactors.

Light water nuclear reactors, normally referred to as pressurized nuclear reactors and boiling water reactors, are taking more than 90% of all the running nuclear power plants all over the world as a result of their intrinsic safety feature [4]. In light water reactors, normal (light) water, opposite to heavy water, is used as the coolant to remove the heat from the nuclear core and moderator that is essential to reduce the speed of fast neutrons produced by the fission reaction. The coolant water is separated from the nuclear fuel by

the cladding materials. Zirconium alloys are widely used as the fuel cladding in water nuclear reactors start in the 1950s because of their high strength and ductility, low neutron absorption cross-section, and relatively good oxidation resistance [5]–[7]. However, zirconium cladding can still react with water at high temperature, which produces hydrogen gas and lead to the failure of fuel cladding and even the explosion of the nuclear plant. In order to improve Zr alloys for nuclear applications, figuring out the reaction mechanism of zirconium and water is necessary. After completely understanding the chemical reaction between zirconium cladding and coolant water, we can design new zirconium alloys through modeling or experimental methods, such as a high-throughput screening (HTS) approach based on building a large database, then applying multiple selection criteria to sift out qualified materials.

The molten salt reactor is one of the Generation IV designs of advanced nuclear reactors aiming at reducing waste production, enhancing fuel efficiency, meeting stringent standards of safety and proliferation resistance while also remaining economically competitive [1]. The precise designs of molten salt reactors remain under Research & Development, but the basic working principles are already clear [1], [8]–[10]. As indicated by the name, molten salts are the most important components in MSRs, serving as the primary coolant and/or the fuel delivery mechanism in which the fission products are dissolved directly in the molten salt composition for transport to the core [8], [11], [12]. Different from the traditional nuclear reactors, the fission fuel is directly dissolved in the coolant salt at around 1000 °C under atmospheric pressure [11], [13]. The working pressure of molten salt reactors is much lower than that of BWRs, especially PWRs, which makes

MSRs safer. There are no cladding materials in molten salt reactors, but the chemical reaction of the piping materials in corrosive salt is not negligible. Both fluoride and chloride salts are proposed to be promising candidates due to their high boiling points and high heat capacity. Comparing to fluoride salt, which normally contains toxic Be element, chloride salt has even lower melting points and higher boiling points. A lot of research was focused on the fuel solubility in LiCl-KCl, and more theoretical studies are performed recently as the development of computational simulations that save more time and cost [14]–[22]. Ab initio molecular dynamics simulations are proved to be a reliable tool to study the corrosion mechanism of the structural metallic materials in the molten salt environment [23]–[31].

1.2 Research Objective and Outlines

Our current research is mainly focusing on determining the corrosion mechanism of metallic materials in nuclear reactors and furthermore investigating strategies that can enhance the corrosion resistance of these metallic materials, as well as improve the safety performance of nuclear plants. As for now, there are more than 400 nuclear power plants all over the world producing about 20% of electricity energy, while water nuclear reactors account for 90% of operating nuclear power plants. For the next-generation nuclear reactors, molten salt reactors attract a lot of attention due to their intrinsic safety features. Besides, the wide applications of different types of molten salts are interesting to investigate. Based on this, the following objectives are expected to achieve:

1. Select promising dopants in Zr alloys with significantly improved resistance of water oxidation using a reaction-mechanism-based high-throughput screening approach. Firstly, the adsorption and dissociation properties of a water molecule on Zr basal (0001) surface were examined by first-principles calculations. Based on the water dissociation mechanism, the HTS was applied on 53 possible doping elements to screen out the elements that could enhance the reaction barrier of water dissociation. Next, the neutron cross-section of doping elements was used to determine whether these doping elements can be used in cladding materials. Finally, the stability of the Zr-X alloy was examined to single out elements that could be synthesized experimentally. Promising elements are supposed to be determined through the HTS process.

2. Study the structure and thermophysical properties of eutectic molten LiCl-KCl and investigate the effect on these properties through the dissolution of Ni and Cr ions. QM-MD and DP-FF MD simulations were applied to examine the structures and thermodynamic properties of LiCl-KCl salt systems including Ni and Cr, from which the coordination environment of the resulting chlorocomplexes was observed and useful thermophysical properties, such as heat capacity and viscosity, of these systems are determined.

Chapter 2. Background and Literature Review

2.1 Development of Nuclear Power Industry

Nuclear energy started to be used for electricity generation in the 1950s. After World War II, scientists realized that the tremendous heat produced from the nuclear fission reaction can be directly used or redirected to the production of electricity [32]. With the increase of the global population, the energy demand all over the world has increased a lot. Meanwhile, energy security becomes an important element. In addition, global climate-changing is more severe in recent decades, which brings carbon emission to the concern of energy production [2], [32]. As a result of all these factors, the development of the nuclear power industry entered a rapid rising stage. Cost effectivity, energy efficiency, air pollution reduction also benefits from the application of nuclear energy [2], [4]. At present, there are 441 nuclear power plants operating in 31 countries and produced power from nuclear energy over 390 GWe [4], [10], [33]. Nowadays, electricity generated from nuclear energy is taking over 10% of the world's electricity and 20% for the United States [2], [11], [33], as indicated in Figure 2.1.

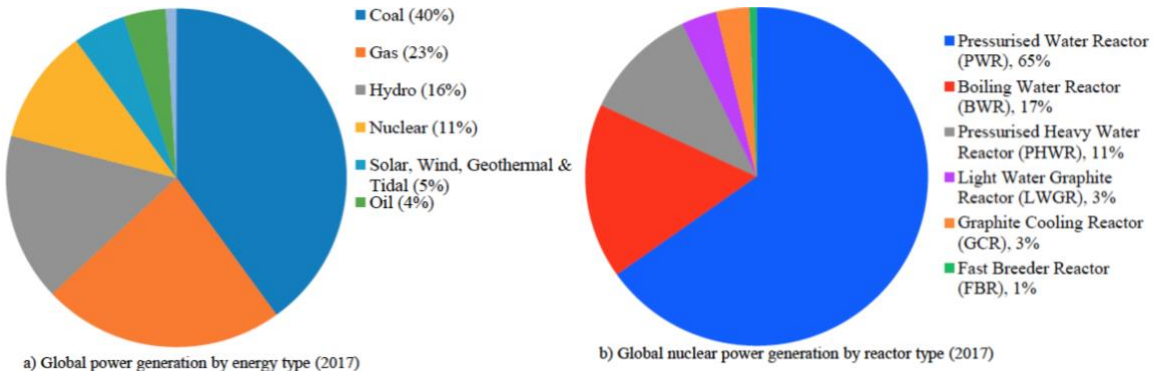

Figure 2.1. Power generation by energy type & nuclear power by reactor type [4].

As of 2020, nearly 69% of nuclear power reactors are Pressurized Water Reactors (PWRs), which were first developed to power the US Navy submarine in 1953 and the design gets improved over these years for more efficient and safer power generation [32], [33]. Boiling Water Reactors (BWRs) account for about 20% of the nuclear energy, the rest is shared by Pressurized Heavy Water Reactors (PHWRs), Gas-cooled reactors (AGRs), Light water graphite reactors (LWGRs), and Fast neutron reactors (FBRs). Details about the existing nuclear reactors in the world are indicated in Figure 2.1 and Table 1.

Table 1. Nuclear power plants in commercial operation or operable in the world [34].

Reactor type	Main countries	Number	GWe	Fuel	Coolant	Moderator
Pressurized water reactor (PWR)	USA, France, Japan, Russia, China, South Korea	299	283	enriched UO_2	water	water
Boiling water reactor (BWR)	USA, Japan, Sweden	65	65	enriched UO_2	water	water
Pressurized heavy water reactor (PHWR)	Canada, India	48	24	natural UO_2	heavy water	heavy water
Gas-cooled reactor (AGR)	UK	14	8	natural U (metal), enriched UO_2	CO_2	graphite
Light water graphite reactor (LWGR)	Russia	13	9	enriched UO_2	water	graphite
Fast neutron reactor (FBR)	Russia	2	1.4	PuO_2 and UO_2	liquid sodium	none
	TOTAL	441	390			

2.2 Nuclear Power Reactors

2.2.1 Light Water Reactors

PWRs and BWRs are accounting for about 90% of the global nuclear power plants because of their ease of operation as well as their outstanding safety during operation. Both BWRs and PWRs use ordinary (light) water as coolant and moderator (works to slow down the neutrons released from the fission reaction so they can cause more fission), therefore they are also categorized as Light Water Reactors (LWRs). As indicated in Figure 2.1 and Table 1, pressurized water reactors are the most popular nuclear reactors, and generate 65% of global nuclear power energy. The primary working principle of water nuclear reactors is using the heat released from the nuclear fission reaction to heat up the water in order to generate steam that is used to drive the turbines to produce electricity. The schematic of PWRs and BWRs can be demonstrated by Figure 2.2 [33].

As indicated in Figure 2.2, the design of PWRs and BWRs are very similar in structures, the only difference is that two water cooling circuits exist in PWRs whereas BWRs only have one single cooling circuit. As shown in Figure 2.2 (a), in pressurized water reactors, the primary cooling circuit flows through the nuclear core, where the temperature could reach 325 °C, under a 150 times atmospheric pressure environment produced by the pressurizer to prevent the water from boiling, that is the reason this type of reactors named as pressurized water reactors. Then the cooling water flows to the secondary circuit, where the pressure is much lower so that water can boil and generate steam in the steam generator and drive the turbines for electricity production. Compared to pressurized water reactors,

the pressure in boiling water reactors is much lower, which is about 75 times atmospheric pressure. Cooling water in the single circuit flows through the nuclear core and is heated up to 285 °C there to produce steam that drives the turbine to generate electricity. The flow direction of the cooling circuit in boiling water reactors [33], [35], [36] is indicated using arrows in Figure 2.2 (b).

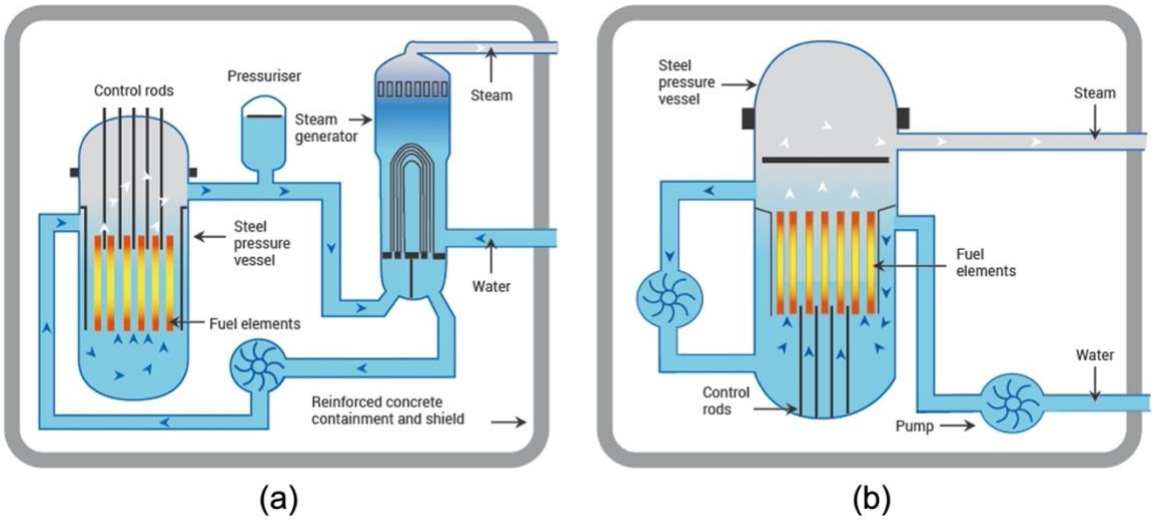

Figure 2.2. Schematic of (a) pressurized water reactors (PWRs), (b) boiling water reactors (BWRs).

Light water reactors are inherently safe during operation as a result of the expansion of fuels and moderators at high temperatures, which leads to the passive reduction in power since less fuel and moderator per volume [11]. However, the high temperature and pressure inside water nuclear reactors may cause some safety issues of nuclear power that was revealed by three major nuclear accidents, the Three Mile Island accident (USA, 1979), the

Chernobyl accident (Ukraine,1986), and the most recent one is the Fukushima Daiichi Accident (Japan, 2011).

The nuclear power reactors operating in Fukushima and Three Mile Island are BWRs and PWRs, respectively [37], [38]. Both the Fukushima Daiichi accident and the Three Mile Island accidents are caused by the reaction of cladding materials and high-temperature steam that are produced by the severe overheating of the core due to the loss of cooling. For the Three Mile Island accident that happened in the USA in 1979, a malfunction in the secondary cooling circuit of the PWR caused the temperature in the primary coolant to rise rapidly, which lead to the automatic shut down of the reactor. At this point, a relief valve failed to close so the primary coolant almost drained away. As a result of that, the decay heat can not be removed. The temperature inside the reactor keeps rising and finally leads to the melting of the core. Later that day, a sudden rise of the pressure was noticed because of the burn of the H_2 gas produced by the chemical reaction between the cooling water and Zr cladding under high temperature [2], [38]–[41]. In the Fukushima accident, all the boiling water reactors were automatically shut down due to the earthquake, which is also the inducement to the outage of electricity used to power the cooling system at the same time. As a result of that, the temperature of the nuclear core increased dramatically which led to the transformation from coolant water to high-temperature steam. The steam reacted with cladding Zr alloy and produced a large amount of H_2 gas. In boiling water reactors, the H_2 gas accumulates in the pressure vessel right above the nuclear core, where thousands of radioactive fuel rods assembled, and eventually lead to the explosion and completely destroy the nuclear plant. A large amount of radioactive nuclear fuel leaks out from the

reactor because of the explosion, and severely damaged the environment near the nuclear plant [37], [39], [42]–[46]. After that, a lot of investigation is performed to figure out better compositions of Zr alloys or alternative cladding materials for water nuclear reactors to prevent the happening of this kind of accident.

In nuclear reactors, the fuel and fission products are confined by four sequent physical barriers to prevent radiation: the fuel matrix, the fuel cladding, the coolant boundary, and the containment building. The fuel cladding is laying between the fuel and coolant working to retain the radioactive fission products and prevent the direct contact of nuclear fuel and coolant, which makes it the most important safety barrier in nuclear reactors [46], [47]. Thus, the improvement of current cladding design and the development of new cladding materials have remained a hot topic. Fundamentally, in order to improve the safety of water nuclear reactors, it is necessary to investigate the reaction mechanism between the cladding materials and cooling water.

2.2.2 Fuel Cladding

With the increase of global population and the development of society and technology, global warming caused by the worldwide emission of carbon dioxide is becoming a severe problem that has dramatic impacts all over the world, such as accelerating the melting of the iceberg, rising of sea level, and even more excessive weather conditions [2]. In order to cut the emission of carbon dioxide gas, clean energy resources like solar, wind, hydro, and nuclear power are sharing more and more proportion of total electricity generation. As a result of the development of technology, the nuclear power industry is concentrated in

developed countries, only 10 percent of nuclear power plants are operating in developing countries. In the past two decades, the growth of the nuclear power industry is mainly focused on developing countries due to its high efficiency, low cost, and some other attractive features. The main concern of nuclear power is its safety issue revealed by two major nuclear accidents in Fukushima and Three Miles Island. Both the two accidents are the result of the intense reaction between the cooling water and fuel cladding under high temperature inside of water nuclear reactors [46]–[49].

The primary working principle of light water nuclear reactors is using the heat generated from the fission reaction of nuclear fuels to heat up the cooling water and produce steam, which drives the turbine to generate electricity. As the most important part of a nuclear reactor, the assemble of nuclear fuel is demonstrated in Figure 2.3 [49]. Radioactive fuel, such as uranium and fissile plutonium, are normally synthesized as fuel pellets and held in metal rods, bundles of these fuel rods stacked together to form a fuel assembly that can be treated as a unit of nuclear fuel [50]–[52], as shown in Figure 2.3.

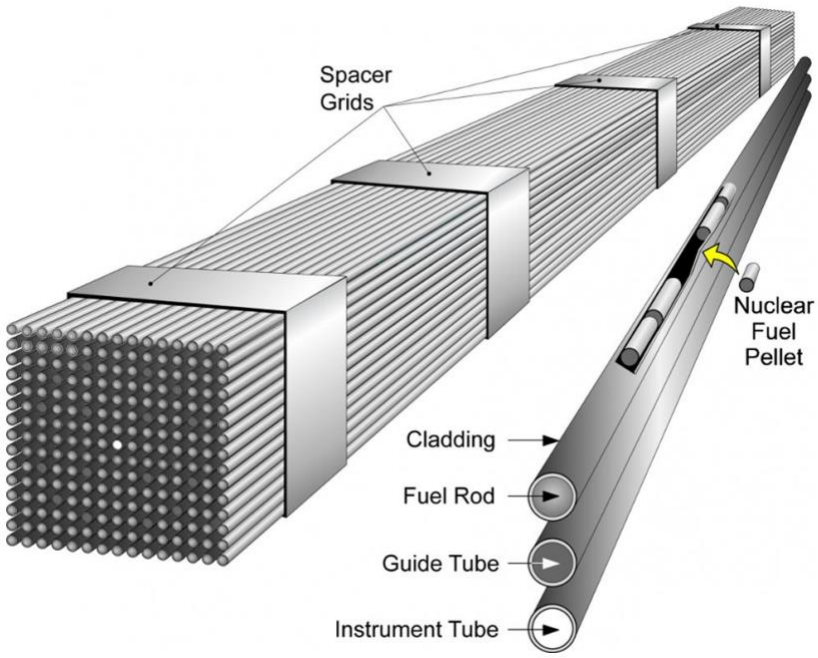

Figure 2.3. The assembly schematic of nuclear fuel [49].

As the core of nuclear reactors, highly radioactive fuels are held by four barriers: the fuel matrix, the fuel cladding, the coolant system, and the containment of nuclear plants. Fuel cladding is the out layer of fuel rods that contain nuclear fuel pellets that separate the nuclear fuel and the water coolant. There are three main functions of fuel cladding, first gives the physical configuration by housing fuel pellets; second prevents direct contact between coolant and fuel; third prevents radioactive fission fragments from escaping the fuel into the coolant and contaminating it, which makes fuel cladding the most important safety barrier in reactors [47].

Based on the function of fuel cladding, the selection criteria can be summarized as follows: high strength to hold the fuel, high service temperature to increase the thermal efficiency, and low neutron cross-section to maximize the fission reaction. A material with a large neutron cross-section will absorb many neutrons when they hit the wall, reducing the efficiency of the chain reaction. Therefore, the cladding must be as transparent as possible to neutrons.

Zirconium-based alloys have been widely applied as the fuel cladding materials for light water nuclear reactors because of their high strength, high thermal conductivity, especially, excellent corrosion resistance, and low neutron absorption cross-sections. Zirconium-tin-based alloys, the Zircaloy family, are widely used in PWRs and BWRs in the United States from the 1950s to the 1990s [3]. As the development of alloy design, advanced alloys, such as ZIRLO ®, OPT-ZIRLO ™, AXIOM ™, M5, and J-alloys have replaced some conventional Zr-Sn alloys in PWRs [48], [53]–[55].

As a result of the intrinsic water oxidation of Zr alloys that can lead to the generation of hydrogen gas, which may cause severe safety issues under high-temperature environments in nuclear reactors, alternative cladding materials have been developed to improve the safety features of light water nuclear reactors. Advanced stainless steel, Ni-base alloys, Mo-based alloys, and ceramic materials SiC, are competitive candidates that may have better performance on better corrosion resistance, higher temperature tolerance, and a higher level of neutron radiation [1], [56], [57].

2.2.3 Molten Salt Reactors

As one of the six Generation IV designs of advanced reactors, molten salt reactor (MSR) is different from the conventional nuclear reactors mentioned above. Currently, there are 18 different design concepts of molten salt reactors, but the main concept is dissolving the fissile and fertile fuel in molten fluoride or chloride salts, which work as the coolant for MSRs [1], [58]. In this case, the heat from the fission reaction can be directly transferred to the salt and fuel mixture and generate the steam used for electricity generation through the heat exchanger [8], [11], [13], [59]–[61], as shown in Figure 2.4.

Molten salt reactors are considered to be one of the most promising next-generation nuclear reactors due to their unique characteristics. The working temperature of MSRs is higher than that of light water nuclear reactors (LWRs), which in turn reduces the possibility of thermochemical hydrogen generation. Besides, the low vapor pressure of molten salts enables a nearly atmospheric pressure environment inside an MSR, which means the stresses on the inner components, such as vessels and piping system, are much lower than other reactors. The design of MSRs makes it possible to perform refuel, processing, and spent fuel removal online [1], [8], [11], [12], [59], [62], [63]. All these features mentioned above indicated that the design of MSRs is remarkable in safety. In addition, there is no fuel cladding in MSRs, since the fuel is directly dissolved in molten salt, which leads to less neutron absorption and higher energy efficiency.

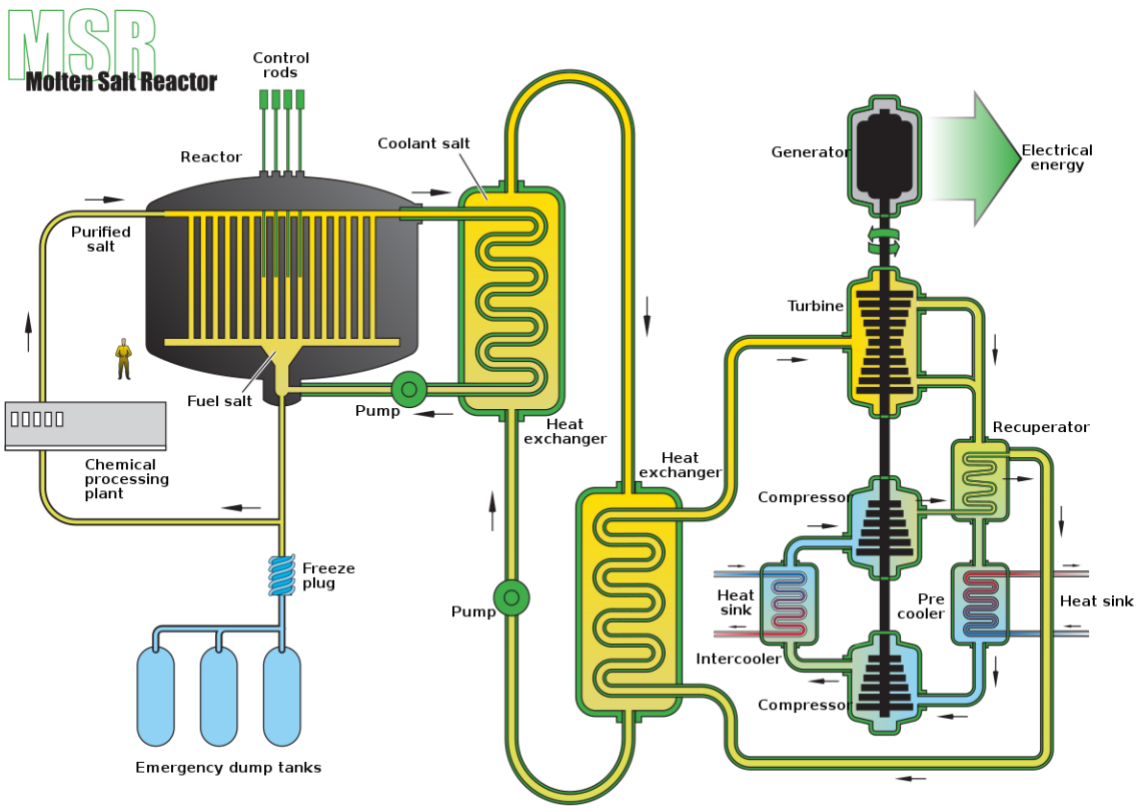

Figure 2.4. The main design concept of a molten salt reactor [1].

Molten salt is a phase change material that is commonly used for thermal energy storage. Molten salts are solid at room temperature and atmospheric pressure, but change to a liquid when thermal energy is transferred to the storage medium. They have low vapor pressure under high temperature, higher heat capacity than the same volume of water, good heat transfer properties, are not damaged by radiation and do not react with water or air. And two kinds of molten salt normally used in MSRs are fluoride and chloride molten salt. Fluoride salts are proposed to be used as a coolant due to their low melting point and high boiling point. But the beryllium element that is normally added to fluoride salts to lower their melting point is toxic. Considering the protection of the environment, some research

start to focus on the application of chloride salt. Compare with fluoride salts, chloride salts have an even lower melting point, and higher solubility for actinides.

On the other hand, problems do exist. One is the corrosion reaction of the Ni-based structural materials remains unclear. Next, the design of the fuel and salt are not settled yet. Extensive testing is required to find a stable mixture of fuel and molten salt. For now, eutectic LiCl-KCl salt is commonly used on the electrorefining of nuclear fuel.

2.3 Corrosion of Structural Metallic Materials in Nuclear Reactors

2.3.1 Oxidation of Zirconium alloys in Water Nuclear Reactors

Zirconium is a transition metal element that was discovered in 1789 and firstly got isolated in 1824. In 1947, the production process of zirconium materials was improved by the US Bureau of Mines and then selected to be used in nuclear reactors for submarines as structural materials. Starting from the 1950s, the application of zirconium has become commercial and started to be used in various severe corrosion environment [5]. Due to their excellent mechanical properties, such as high strength and ductility, low neutron absorption cross-section, especially the excellent corrosion resistance in moderate high temperature (300 ~ 400 °C), zirconium alloys are widely used in water nuclear reactors as the cladding materials [3], [5], [7], [46]. However, one of the safety issues in the usage of zirconium alloys as the fuel cladding material is their inclination to react with oxidants like water [3], [5], [64]. Zirconium alloys will lose their corrosion resistance under high temperatures (> 400 ºC) as a result of hydrogen uptake [7], [65], [66].

The Fukushima nuclear accident that happened in 2011 was most likely caused by the explosion of hydrogen gas produced by the reaction between zirconium alloys and the high-temperature steam [39], [45]. In this accident, electricity used to power the cooling system was shut down due to the earthquake, which then leads to the rapid increase in the temperature of the nuclear core. Cladding zirconium alloys reacted with the high-temperature steam and produced a large amount of hydrogen which eventually lead to the explosion of the nuclear plant [39], [45]. Therefore, it is essential to develop novel zirconium-based cladding materials that can suppress the oxidation from water.

Even the oxidation layers of Zr alloys could protect the metal alloys from reacting with H_2O to a certain extent. The oxygen anions in H_2O could migrate through these oxide layers and react with Zr at the Zr/Zr_2O interface so that the protective oxide keeps growing in the water environment. As the oxide layer grows, the stress inside the oxide layer increases due to the volume expansion, leading to crack formation. Therefore, the water penetrates these oxide layers and reacts with Zr [3]. The purpose of this study is to find promising dopants that inhibit the oxidation of zirconium alloy so that the waterless reaction with Zr after penetrating the crack in the protective layers.

The reaction mechanisms between zirconium alloys and water have been investigated experimentally for several decades [3], in order to understand the complex corrosion mechanism and develop better zirconium-based alloys to improve their corrosion properties. It was proposed that the corrosion resistance of zirconium is obtained from the protective oxide layer formed by the reaction between zirconium and water [3],

$$Zr + 2H_2O = ZrO_2 + 2H_2$$

Previous studies have indicated that existing cracks inside the protective oxide layer can be promoted by hydrogen pick up and keep growing until break the oxide layer, then lead to the failure of zirconium cladding [3], [7], [46], [65], [67].

Density functional theory (DFT) simulations provide a clear view of the adsorption process at an atomic level. The adsorption behavior of water molecules on the zirconium surface was examined by Wang *et al.* [68] and Nie *et al.* [69] using first-principles simulations. They found that the azimuthal orientation of flat-lying water molecules has a small effect on the adsorption energy and the upright water configuration is more favorable for dissociation. Through computing the water absorption energy from various zirconium (Zr) doped systems, Nie et al. [69] proposed that dopants, such as Ge, Sn, Sb, Zn, Ga, Ru, Rh, Pd, Ag, Cr, Mn, Fe, Co, Ni, Cu, Nb, and Mo, could be considered as promising doping elements to improve their resistance of water oxidation. However, it remains unknown how these dopants influence the water dissociation process and mechanism. Particularly, the reaction barrier may not linearly depend on the absorption energy.

The main disadvantage of conventional alloy design and evaluation of alloy systems is high cost and low efficiency because of the need for huge design space for possible compositions and many conflicting design goals. Particularly, the corrosion tests on various Zr alloys are very expensive and time-consuming. Nowadays, tremendous efforts have been devoted to rational design strategies guided by virtual screening, which requires the development of advanced modeling methods. Especially, The high-throughput computational materials design has become very popular in recent years and has been

widely used in lithium batteries [70], CO_2 capture materials [71], catalysts [72], [73], alloys with improved mechanical properties [74], and others. It is expected that the Zr alloys design could also be accelerated using the high-throughput computational methods.

2.3.2 Molten Alkaline Salt in MSRs

With the development of technology and materials, scientists and engineers are developing new nuclear reactors that can provide higher energy efficiency, reduction in waste production, and better safety standards to meet the energy needs of the world. This project is known as the Generation IV International Forum [1]. There are six designs including Gas-cooled Fast Reactor (GFR), Lead-cooled Fast Reactor (LFR), Molten Salt Reactor (MSR), Supercritical Water-cooled Reactor (SCWR), Sodium-cooled Fast Reactor (SFR), and Very High Temperature Reactor (VHTR) [1]. Though these designs are under R&D, molten salt reactors (MSRs) are receiving more and more attention recently because of their intrinsic safety features [8]. The basic idea of MSR is dissolving the nuclear fuel in the coolant – liquid molten salt at high temperature (700 ~ 740 °C) and atmosphere pressure [9], [13]. The attractive properties of molten salts are their high heat capacity and boiling point. Both fluoride and chloride salts have been proposed to be a candidate coolant for MSRs with different compositions.

Molten salts are ionic salts that have relatively low melting points and thus enter the liquid phase at elevated temperatures [75]. Molten salts are effective for many different applications due to their excellent thermophysical properties, such as high-temperature stability, low vapor pressure, good conductivity, low viscosity, etc [24], [76]–[78]. Many

different combinations of nitrate, fluoride and chloride molten salts have been used in various applications such as concentrating solar power, energy storage, production of non-ferrous metals, fuel cells, and the recycling of nuclear fission products (pyro-processing) [8], [79], [80]. The most remarkable feature of molten salts is their high heat capacity that is similar to water; unlike water, however, neither significantly expand nor generate steam that creates a high pressure inside the reactor while heating, which makes them ideal coolant compositions for use in molten salt nuclear reactors [75]. Molten salts are also highly electrolytic and thus efficient for the separation of materials; pyro-processing takes advantage of this property to separate actinide products from transition metals and lanthanides in nuclear waste [81]. The electrolytic nature of molten salt compositions also makes them highly corrosive, introducing unique engineering challenges for their use in various applications [82], [83].

The molten salt reactor (MSR) is one of the Generation IV designs of advanced nuclear reactors designed for the primary goals of reducing waste production, enhancing fuel efficiency, meeting more stringent standards of safety, and nuclear proliferation resistance while also remaining economically competitive. Highly effective modern molten salt reactor designs are still under development, but the basic working principles are already clear from previous research [1], [8]–[10]. As indicated by the name, molten salts are an important component in MSRs, serving as the primary coolant and/or the fuel delivery mechanism in which the fission products are dissolved directly in the molten salt composition for transport to the core [8], [11], [12]. Fluoride salts are generally favored in the proposed MSR design for primary cooling based on their low vapor pressure under

high temperature, higher heat capacity than the same volume of water, good heat transfer properties, resistance to damage by radiation, and resistance to reactions with water or air [13].

Chloride salts have even lower melting points and higher solubility for actinides than fluoride salts [13]. In addition, the corrosion of metallic structural materials in molten salts is a challenging issue for MSRs since the molten salt directly contacts both the pipes and pumps involved in the circulation of the salt throughout the reactor system. Compared to fluoride salt compositions, corrosion reactions between structural alloys and chloride salts are less thermodynamically favorable [31], [84]. Nevertheless, the corrosion of alloys in chloride salts is more complicated and harder to predict because chlorine has several different oxidation states including +1, +3, +5, and +7 [84], [85]. This leads to additional complexity in the bonding behavior of metal ions dissolved in chloride salt compositions, which can alter the local coordination environment drastically. Both LiCl-KCl and NaCl-$MgCl_2$ are common chloride-based molten salts used as the primary coolant in MSR designs and the pyrochemical reprocessing of spent nuclear fuel [86]–[88]. Ni-based superalloys, e.g. Inconel and INOR alloys, are widely used for the piping and heat exchange equipment in MSRs because of their high strength and corrosion resistance to salts [59], [89]. As two primary compositional elements of Ni-based superalloys, some Ni and Cr ions from corrosion reactions will dissolve into the molten salt and form chlorocomplexes such as $NiCl_2$ and $CrCl_3$. These chlorocomplexes may affect the physical and thermal properties of molten salts.

Investigation of the structure and properties of chloride molten salts, which is necessary for the effective development of next-generation molten salt reactor designs, is difficult through experimental methods because of the relatively high operating temperature of MSRs (up to 700 ºC – 900 ºC) as well as the complexity of the purification of salt mixtures [89]. Recently, computational methods have been employed to avoid these problems. Bengtson's work proved first-principles molecular dynamics (FPMD) approach is capable to predict the structure and thermo-kinetic properties (e.g. volume, thermal expansion, bulk modulus, and diffusivity) of LiCl, KCl, and eutectic LiCl-KCl molten salt, and proposed the possibility of applying FPMD to predict the behavior of solutes in LiCl-KCl [25]. FPMD simulations have been applied to calculate the redox potentials of actinides and other metallic cations in LiCl-KCl eutectic reported by Song [16] and Zhang [14], which provide prospects of application of FPMD in the pyro-processing of spent nuclear fuels. Additionally, the local structures and transport properties of various molten alkali chlorides are investigated using MD simulations.[23], [27] Galamba *et al.* [90], [91]. accurately reported the viscosity and thermal conductivity of molten pure KCl and NaCl using equilibrium and nonequilibrium molecular dynamics (MD) simulations, suggesting that MD simulations are an applicable method to predict the properties of molten chloride salts.

Fluoride salts are favored in MSR primary cooling based on their low vapor pressure under high temperature, higher heat capacity than the same volume of water, good heat transfer properties, not being damaged by radiation, and not reacting with water or air [13]. Nevertheless, the beryllium element in the current molten fluoride salt (LiF-BeF_2), which

has a lower melting point and higher boiling point than the other fluoride salts, is toxic. Compare with fluoride salts, chloride salts have an even lower melting point and higher solubility for actinides. NaCl is proposed to be a promising candidate due to its good nuclear, chemical and physical properties, while its high melting temperature can be lowered by blending with other chloride salts. The chloride salt we are interested in is the eutectic LiCl-KCl with 58% LiCl and 42% KCl, which is a common molten salt used in electrorefining of spent nuclear fuel to separate actinides and other fission products [25], [88], [92].

In molten salts, the activity of metallic elements is determined by dissolution. Based on NASA's study, the inclination for common alloying constituents that are likely to corrode in molten fluoride salt increases in this order: Ni, Co, Fe, Cr, and Al [93]. According to the literature and thermodynamics data, Ni is normally immune to corrode in molten fluoride salt but lacks the strength of structural materials used for piping and other heat exchange equipment. Whereas Cr tends to dissolve in a salt environment and leads to the weight loss of the alloy. This phenomenon was observed both in fluoride and chloride salts. The corrosion behavior of a Ni-plating alloy in molten FLiNaK salt at 850 °C was studied by K. Sridharan et al. in order to evaluate the corrosion resistance of Ni alloys with different compositions and estimate the diffusion rate of Cr through the Ni-plating. Their results indicated that the Ni-plating can effectively limit the diffusion of Cr to the molten salt [94].

Current research is focusing on the development of the optimum solution for molten salt with suitable compositions that can maintain required properties such as operating temperatures, neutronic properties, fission product solubility, and so on. Despite the design

of coolant, the corrosion of metallic containers by molten salt is also a big problem to solve. Therefore, the corrosion mechanism of alloys in molten salt is important to investigate so that the corrosion behavior can be controlled by designing alloys or molten salts with different compositions. The first-principles molecular dynamics simulations have been proved to be applicable to predict the properties of eutectic LiCl-KCl molten salt [25].

Chapter 3. Computational Simulation Details and Analysis Methods

3.1 Density Functional Theory Simulations

All the calculations were performed using density functional theory (DFT), as implemented in the Vienna ab initio simulation package (VASP) [95]. The Perdew–Burke–Ernzerhof (PBE) GGA exchange correlation functional is applied, accounting for the electronic exchange-correlation interactions [96]. The wave functions are expanded in plane wave basis sets with a kinetic energy cutoff of 500 eV. The convergence criteria for the electronic and ionic relaxation are 10^{-5} eV and 0.01 eV/Å, respectively. The electron partial occupation was accounted using the Methfessel-Paxton scheme with 0.1 eV width of the smearing. The vdW interaction was accounted using the DFT-D3 approach [96].

To examine the water absorption and dissociation processes over Zr surface, we constructed a Zr (0001) slab model with the vacuum along z direction, as shown in Figure 3.1. The unit cell was expanded to a 2 × 2 supercell along x and y directions, respectively, so that the top surface contains four Zr atoms to interact with a water molecule. Five atomic Zr layers were adopted in the slab model with the bottom two layers fixed and three top layers are free to relax in simulations. The 5-layers model is enough to study the water dissociation mechanism on Zr (0001) surface [68]. A 20 Å vacuum region was applied in the slab model to avoid the interaction between replicated images. The water molecule is placed on the slab and a dipole correction is applied to compensate for the induced dipole moment. The configurations of the adsorption system will be explained in detail.

Integrations over the Brillion Zone is performed using the Monkhorst–Pack [97] scheme with 7 × 7 × 1 k-points in the slab calculations. Spin polarization calculations were performed for all the doping elements.

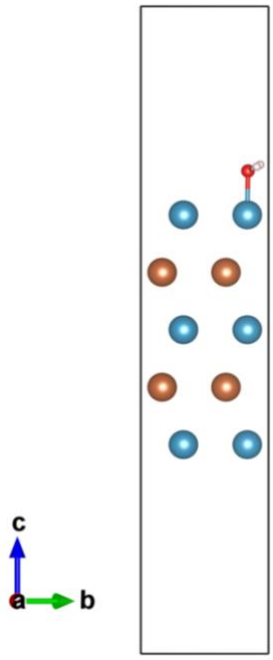

Figure 3.1. Structure of the adsorption system, one H_2O molecule on the top of Zr (0001) surface. The blue and brown spheres represent the top and the second layer, respectively.

3.2 Quantum Mechanics Molecular Dynamics

QM-MD simulations have been demonstrated to be a reliable method to predict the properties of molten salts [25], All QM-MD calculations in the present study were performed using the Vienna Ab-Initio Simulation Package (VASP) [95], [98], [99]. The Perdew–Burke–Ernzerhof (PBE) GGA exchange-correlation functional was applied,

accounting for the electronic exchange-correlation interactions [96]. The PAW-PBE potentials were used for Li, Cl, K, Ni, and Cr by treating $2s^1$, $3s^23p^5$, $3p^64s^1$, $3s^23p^63d^84s^2$ and $3d^54s^1$ as valence electrons, respectively. The cutoff energy and convergence criterion for the electronic relaxation were set to be 400 eV and 10^{-4} eV, respectively. A 1 × 1 × 1 k-point mesh was used for sampling the first Brillouin zone. Spin polarization was considered for systems including the Ni and Cr elements, utilizing a magnetic moment, obtained by calculation, of 2.0 and 3.0 for Ni and Cr, respectively. We tested various dispersion corrections methods including PBE-D2 [100], PBE-D3 (Becke-Johnson) [101], and PBE-D3 (Grimme) [102]. PBE-D3 (Grimme) was found to give the closest density to that determined by experimental methods [103], as shown in Figure 3.2 and Table 2.

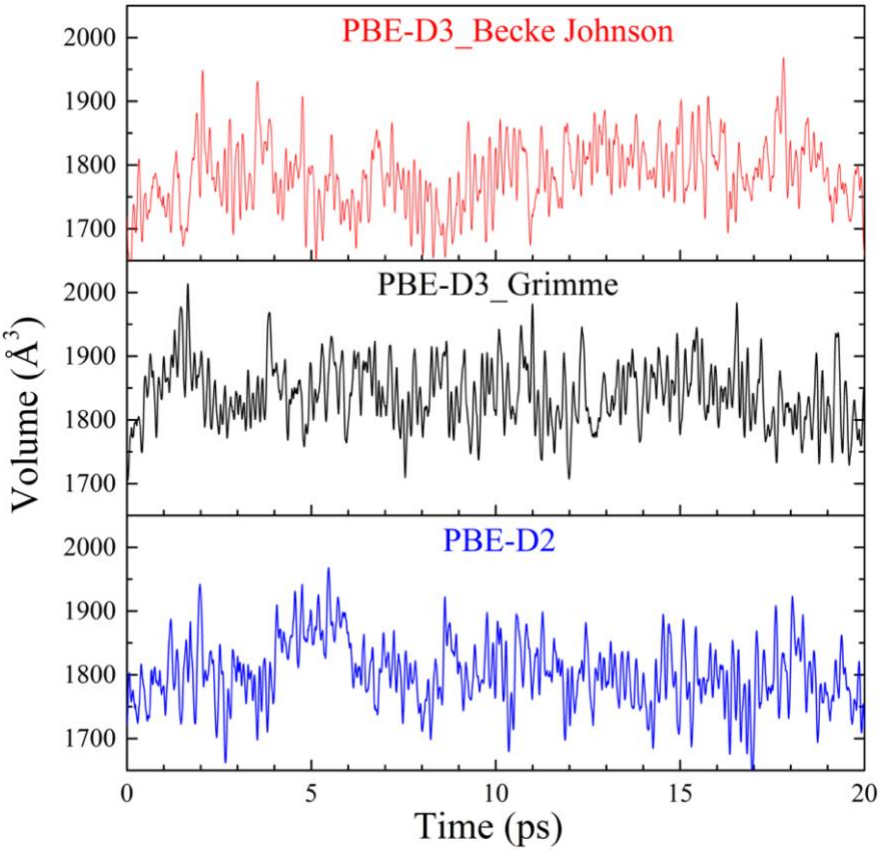

Figure 3.2. NPT volume changes of LiCl-KCl supercell for PBE-D2, PBE-D3 Becke Johnson, and PBE-D3 Grimme dispersion corrections.

Table 2. The density of LiCl-KCl salt system for vdW corrections compared with experimentally measured data.

Functional	**Density (g/cm^3)**	**Atomic Volume (Å/atom)**
PBE	1.5149	30.39
PBE-D2	1.6438	28.01
PBE-D3_Grimme	1.6062	28.67
PBE-D3_Becke Jonson	1.6363	28.14
Experiment	1.6213 [22] 1.6189 [25]	28.67 [25]

The initial structure of LiCl-KCl molten salt was constructed as a 64-atom supercell, which was proven suitable for studying the structure and thermokinetic properties by the previous study [25]. The composition of eutectic LiCl-KCl molten salt is 59.4 mol% LiCl, 40.6 mol% KCl, therefore the supercell was designed to match this composition by containing 19 Li atoms, 13 K atoms, and 32 Cl atoms, randomly distributed in the box, as shown in Figure 3.3 (a). The initial supercell was then heated up to 2000K, which is well above the melting point of eutectic LiCl-KCl, in order to obtain the well-equilibrated liquid structure. The system was equilibrated for 20 picoseconds using the isothermal–isobaric (NPT) ensemble. In the NPT ensemble, the pressure is controlled using the Parrinello-Rahman [104], [105] method where the fictitious mass and the friction coefficient are 30 amu and 10 ps^{-1}, respectively, for the lattice degrees-of-freedom. The temperature is controlled using the Langevin thermostat [106] with the friction coefficients of 10 ps^{-1} for

atomic degrees-of-freedom. We used a timestep of 1.0 femtosecond in integrating the equations of motion.

For the LiCl-KCl molten salt with Ni solute, one Li atom and one K atoms were removed to keep the charge balance for the addition of Ni^{2+}. Similarly, for the LiCl-KCl system with Cr solute, a single Cr^{3+} was introduced in the LiCl-KCl system by the replacement of one K and the removal of two Li atoms. After the equilibration process at 2000 K, the liquid was quenched to the target temperature using an ultrafast cooling rate of 3.5×10^{13} (K/s) to examine the structural and thermophysical properties at various temperatures.

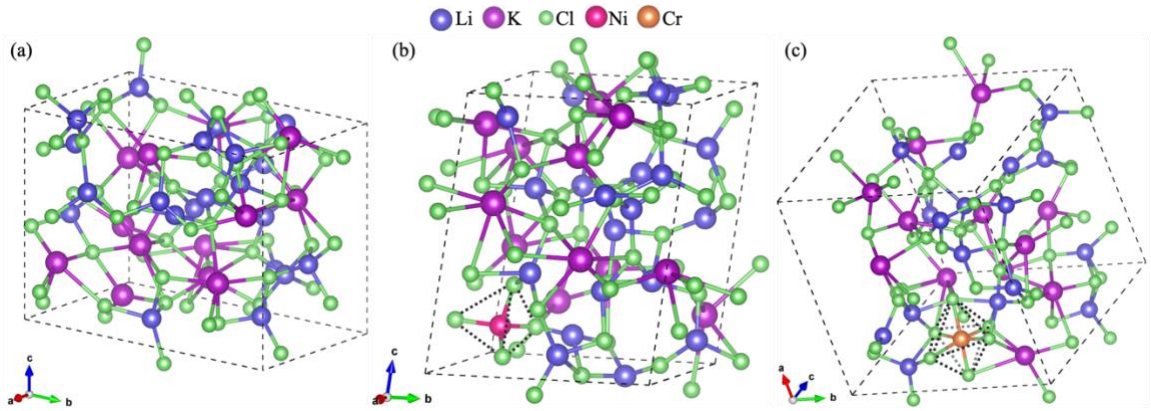

Figure 3.3. QM-MD models of LiCl-KCl molten salt at 773 K. (a) eutectic LiCl-KCl system with 64 atoms, a trinclinic crystal cell with a = 11.74 Å, b = 13.16 Å, c = 12.63 Å, α = 93.18°, β = 73.46°, γ = 101.06°; (b) $NiCl_2$-LiCl-KCl with one Ni in the 63-atom supercell, a = 11.70 Å, b = 11.99 Å, c = 13.46 Å, α = 78.12°, β = 83.39°, γ = 74.22°; (c) $CrCl_3$-LiCl-KCl with one Cr in the 62-atom supercell, a = 14.59 Å, b = 11.93 Å, c = 12.65 Å, α = 58.35°, β = 92.67°, γ = 107.26°. The blue, purple, green, magenta, and orange spheres represent Li, K, Cl, Ni, and Cr atoms, respectively.

Due to the working temperature of eutectic LiCl-KCl molten salt in reactors and pyro-processing applications (500 ºC and above), the temperature range of our simulation was selected from 673 to 1073 K [107]. The timestep for integrating the equation of motion in QM-MD was set to 1.0 fs. The liquid salt was quenched from 2000 K to these temperatures and equilibrated at the target temperature for another 20 ps using the NPT ensemble. The last 10 ps trajectory in the equilibrium NPT simulations was adopted to determine the density at various temperatures. Figure 3.3 displays the equilibrated atomistic structure of three LiCl-KCl systems at 773 K after 20 ps MD simulations, with cell parameters provided in the figure caption. Additionally, a trajectory was obtained from a subsequent 20 ps canonical (NVT) ensemble simulation from which structural and thermodynamic property analysis was performed. The average pressure of the NVT simulations for all temperatures is close to zero. Figure 3.4 exhibits one example of eutectic LiCl-KCl at 973 K and the average pressure is ~ 0.06 kbar after equilibrium.

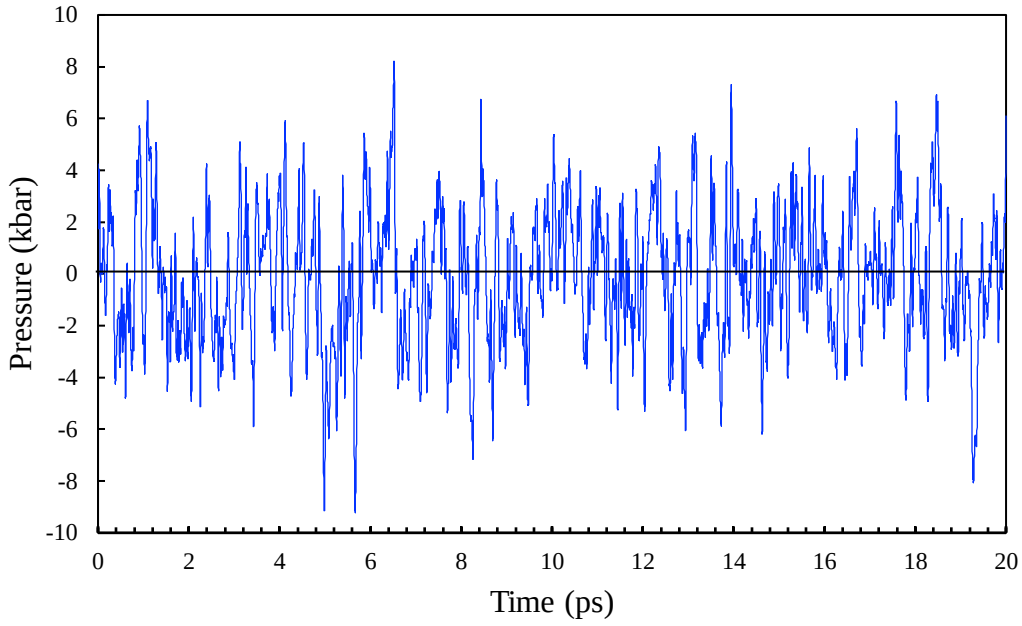

Figure 3.4. The pressure curve of the 20 ps NVT simulation for eutectic LiCl-KCl salt at 973K. The average pressure of the last 10 ps NVT simulation is 0.06 kbar.

3.3 Deep-Learning Force Field Molecular Dynamics

Machine learning (ML) methods have been applied to describing the PES of atomistic systems with many successful applications [108]–[114], demonstrating the accuracy of using ML methods, particularly neural network models, to represent the PES. For example, the bonds-in-molecules neural network method (BIM-NN) uses empirical information on the chemical bonds as input [113]. Another example is the Gradient domain machine learning (GD-ML) scheme using a global descriptor for the whole molecular pattern [112]. In addition, the Behler-Parrinello neural network (BP-NN) model uses hand-crafted local symmetry functions as descriptors [114], requiring human intervention. The recent studies

using ML-FF on molten salt systems [30], [115]–[117] proved the local structure, thermophysical properties, and transport properties of some alkaline chlorides predicted by ML developed deep potentials agree well with AIMD and experimental results, suggesting that these properties can be accurately predicted using the ML-FF based MD simulations.

Accurately describing the interatomic potential energy surface (PES) is essential to effectively apply MD simulation techniques to investigate the structural and thermophysical properties of molten salt systems. QM-MD simulations based on the PBE functional have been widely used to investigate various molten salt compositions [25], [118], [119]. However, the spatial- and time- scales of QM simulations are limited to hundreds of atoms and within 100 picoseconds time frames, making it impractical to simulate the thermophysical properties that rely on either larger system scales or longer timespans, such as viscosity and thermal conductivity. Here we apply the recently developed deep potential model that represents the PES as a sum of "atomic" energies [110], [111]. The atomic energy depends on the coordinates of the atoms in each atomic environment in a symmetry-preserving way. The potential energy of each atomic configuration is a sum of "atomic energies" $E = \sum_i E_i$, where E_i is determined by the local environment of atom i within a cutoff radius R_c [110]. The environmental dependence of E_i is complex and nonlinear, and the neural network (NN) is able to capture the analytical dependence of E_i on the coordinates of the atoms in the environment in terms of the composition of the sequence of mappings associated with the individual hidden layers. The smooth edition of this deep potential (DeepPot-SE) uses a smooth cutoff parameter that allows the interactions within the cutoff region to smoothly go to zero at the boundary of

the local region defined by cutoff radius R_c [120]. By training the energy, atomic force, and viral stress of the systems from the QM-MD simulations, this DeepPot-SE has been successfully applied to various systems such as H_2O [110], small organic molecules, metal, metal oxide, as well as high entropy alloys [120].

To develop the DP-FF, we trained the NN parameters using a training set of QM-MD simulations on the liquid salts from 673 to 2000 K, which are generated using VASP software. In the QM-MD simulations, the energy of the supercell, the force on each atom, and the viral stress tensor of the supercell were saved at every timestep (1.0 fs) for a total of 20 ps run. Then we trained the DP-FF parameters to match the energy and the viral stress of the supercell, as well as the force on each atom from QM-MD simulations. The liquid salts include single compound systems: LiCl, and KCl; binary systems: LiCl-KCl, LiCl-$NiCl_2$, and KCl-$NiCl_2$, LiCl-$CrCl_3$, and KCl-$CrCl_3$; and the ternary system: LiCl-KCl-$NiCl_2$, and LiCl-KCl-$CrCl_3$. The QM-MD trajectories (20 ps) of liquid salts were generated at 673 K, 773 K, 873 K, 973 K, 1073 K, 1200 K, 1400 K, and 2000 K using NPT ensemble. We also generated the heating trajectory from 673 to 2000 K, as well as quenching trajectory from 2000 K to 300 K, both within 20 ps. As metal ions Cr and Ni are incorporated into these systems, the QM data on the crystalline phase (300 K) and liquid phase (2000 K) of these metal salt systems, e.g., $NiCl_2$ and $CrCl_3$, were also included in the training set.

In the DP-FF training process, we set up the cut-off radius for neighbor searching as 6.0 Å and the smoothing starting from 5.8 Å. Three layers of neural networks were applied, and the size of each hidden layer was 120, 120, and 120 respectively in the fitting. We used

a varying learning rate starting from 0.001 and ending at $3.51e^{-8}$ with exponential decay. A total of 1,000,000 steps were set up in the training process. The loss function in the training process is composed of energy error, force error, and virial error, and they are shown in Figure 3.5. These loss functions for the validation dataset are displayed in Figure 3.6, which is consistent with the training dataset. We also tested our force field by directly comparing the DFT data using 100 data points. We find that the differences between DFT and DP-FF for energy, force, and virial stress are ~ 2.1×10^{-3} eV/atom, ~ 3.6×10^{-2} eV/Å, and ~ 9.8×10^{-3} kbar, respectively, demonstrating the accuracy of the developed force field.

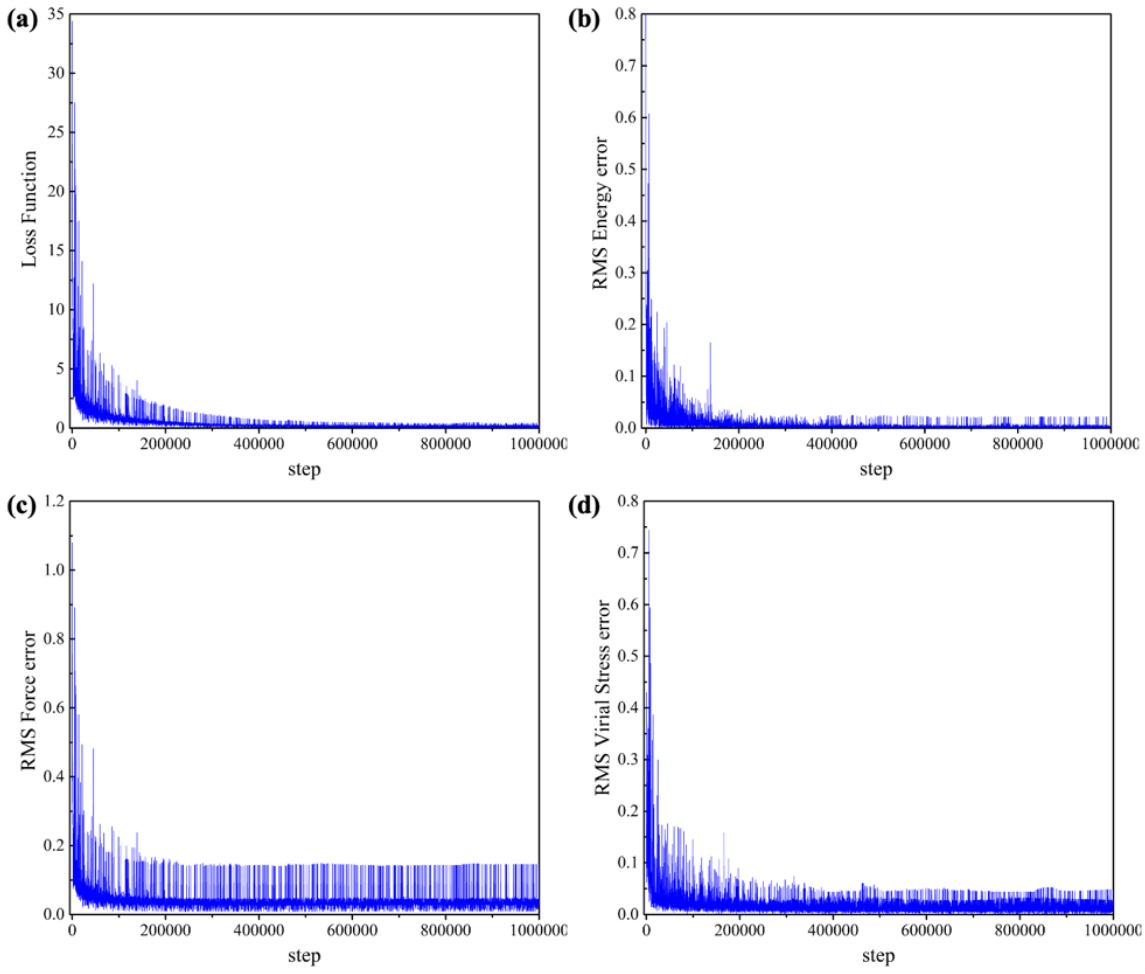

Figure 3.5. The loss function in the training process of DP-FF. (a) loss function, (b) root mean square (RMS) energy error, (c) RMS force error, and (d) RMS virial stress error.

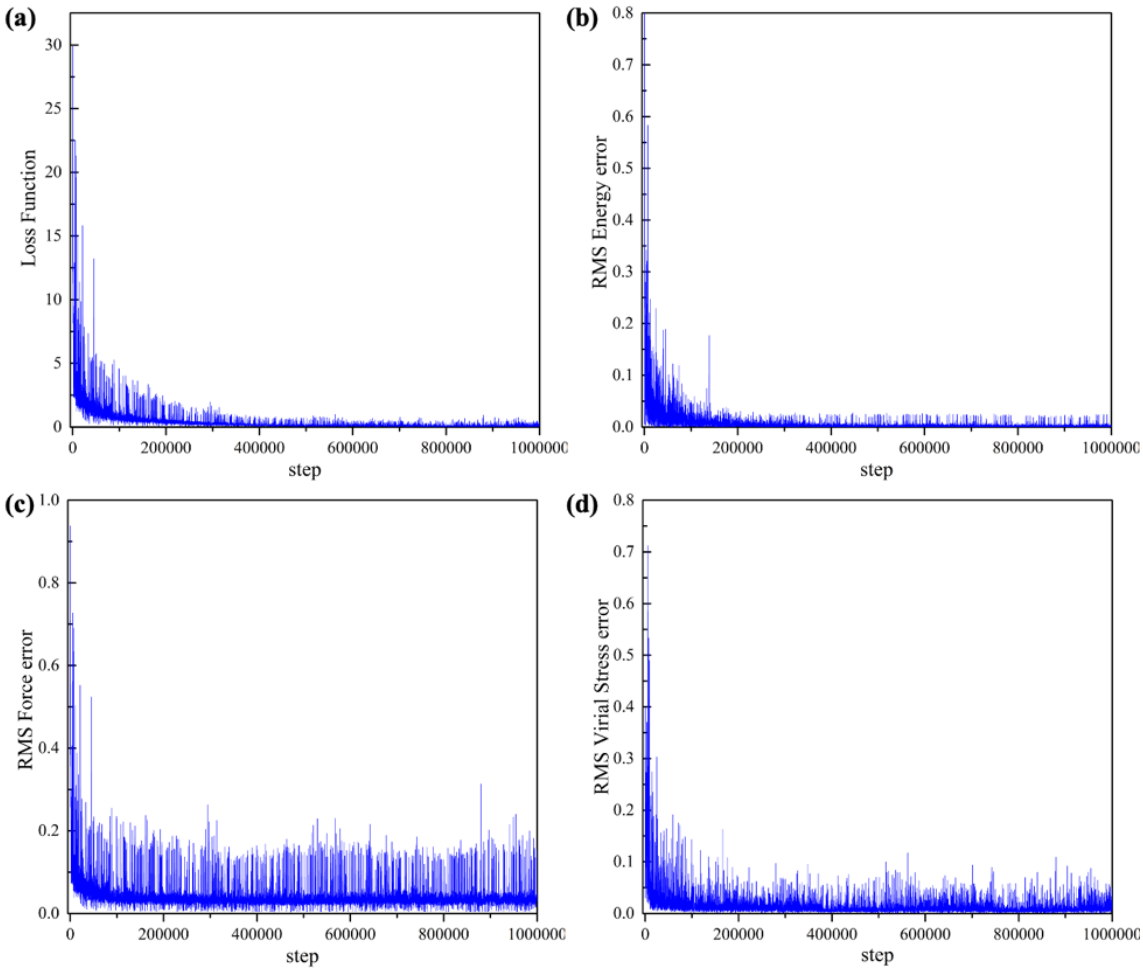

Figure 3.6. The loss function for the validation dataset. (a) loss function, (b) root mean square (RMS) energy error, (c) RMS force error, and (d) RMS virial stress error.

After the DP-FF was well trained, we performed the MD simulations using this force field on a much larger system than QM-MD simulations. The supercells have 4096, 4032,

and 3968 atoms with dimensions of ~ 4.8 nm along with three directions for LiCl-KCl, $NiCl_2$-LiCl-KCl, and $CrCl_3$-LiCl-KCl systems, respectively. The concentrations of Ni and Cr in eutectic composition are the same as the QM-MD simulations for consistent comparison. The periodic boundary condition was applied to eliminate the surface effects and a timestep of 1.0 fs was used in the integration of motion. The NPT ensemble was used to equilibrate the liquid phases at target temperatures from 673 to 1073 K. The Nose-Hoover thermostat and barastat were applied to control the temperature and pressure in the simulations with the coupling constant of 100 fs and 1000 fs, respectively. To compute the viscosity, the NVE ensemble was used with a total of trajectory corresponding to 1 nanosecond.

3.4 Analysis Methods

3.4.1 Climbing Image Nudged Elastic Band and Dimer

The water dissociation mechanism was determined using the climbing image nudged elastic band (CI-NEB) approach that simulates the minimum energy path between the initial and final minimum energy states and finds out the saddle point along this path [121], [122]. The CI-NEB simulations were carried out to determine the reactions pathways, transition states, and reaction barriers. In CI-NEB calculations, eight images were generated for the undoped system, and four images were used for the doped systems. The energy and force criteria for the convergence of CI-NEB calculations were set to 1×10^{-5} eV and 2×10^{-3} eV/Å, respectively.

The transition state (TS) structure is essential to determine the energy barrier of a chemical reaction, which is the energy difference between the stable state and the transition state [123]. In order to get a more accurate TS of the reaction path, the dimer method was applied and the initial structure for the dimer calculation was generated from the CI-NEB calculations. In the dimer calculation, the saddle point was achieved by rotating the TS structure until it find the lowest curvature mode of the potential energy [123], [124]. The maximum number of rotation steps was set to 10, and the convergence criteria for dimer calculations were set to 1×10^{-7} eV for the energy and -0.01 eV/Å for the force, respectively.

To examine the temperature effect, we computed the free energy correction at reactor working conditions (633 K). The free energy correction was computed from the phonon modes assuming the harmonic approximation. The phonon modes were derived from the density functional perturbation theory (DFPT) [125]. Then the energy (E) of phonon systems can be derived from the phonon frequency. Using the thermodynamic relations, entropy (S), and Helmholtz free energy (F = E – TS) can be computed as functions of temperature. Our results showed that the energy barrier at 633 K is just 0.0089 eV higher than that at 0 K (0.1686 eV). Therefore, the temperature effect on DFT simulations is small in the water dissociation reaction on Zr and it will not be considered for the alloy systems.

3.4.2 Reaction Mechanism Based High Throughput Screening Approach

High throughput screening (HTS) is in general a materials design strategy that combines the computational thermodynamic methods and data analysis [126]. So far, the HTS

approach has been already applied in biological areas, such as drug discovery. Whereas the application of HTS is not limited to a certain area, and the benefits of HTS have been demonstrated in various research fields, for example, high-throughput DFT is an effective tool that makes the computational test of thousands of compounds possible. In computational materials science, previous HTS studies consist of three main stages: i) materials collection; ii) materials calculation; iii) characterization and selection [127]–[131]. Here we extended the traditional HTS approach and proposed a reaction mechanism based HTS approach. The key steps for our HTS are displayed in Figure 3.7.

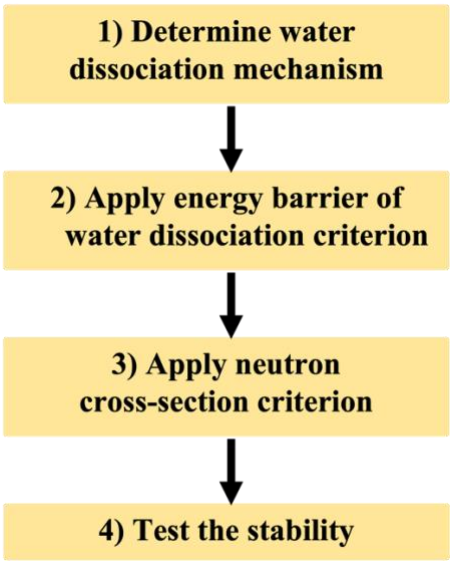

Figure 3.7. Four stages of HTS approach criterion.

In order to sift out qualified alloyed elements to improve the resistance of water oxidation for Zr alloys, we proposed the reaction mechanism based HTS approach consisting of the following stages in a decreasing order of importance: (1) Determining the

water dissociation reaction mechanism and calculating the energy barrier of water dissociation; (2) Using energy barrier of water dissociation to screen out the doping elements that can increase the dissociation barrier; (3) Applying neutron absorption cross-section (σ) criterion on the elements from step (2) to screen the elements have low neutron absorption cross-sections to minimize the neutron loss in nuclear reactors; and (4) Checking the stability of the alloying systems from previous steps to make sure the alloy can be synthesized experimentally.

It is worth noting that neutron absorption cross-section is a measurement of the possibility of a nuclear reaction occurring or not. In nuclear reactors, the lower the absorption cross-section of nuclear cladding, the less neutron loss, so that the chain reactions in nuclear reactors are sustainable. The fuel cladding material is an intermediate layer between the nuclear fuel and coolant to prevent the direct contact of these two parts, and to keep the radioactive fission products isolated. Therefore, a proper cladding is supposed to minimize the neutron loss [46]. A potential doping element should have a similar neutron absorption cross-section to zirconium.

3.4.3 Local Orbital Basis Suite Towards Electronic-Structure Reconstruction

To illustrate the physical origin of the modified water dissociation barrier from dopants, we analyzed the Zr-O bond strength in the most promising system and compared it with the undoped Zr system. The chemical interaction between the water molecule (O atom) and the surface metal atoms is analyzed using LOBSTER (Local Orbital Basis Suite

Towards Electronic-Structure Reconstruction) based on periodic plane-wave (PAW) output [132]. LOBSTER is a program that extracts the projected crystal orbital Hamilton population (pCOHP) based on the projected plane waves achieved from the DFT simulations to reveal the orbital-pair interactions [132]–[135]. Projected COHP gives the bonding information in terms of band structure energy, and the integrated pCOHP (IpCOHP) indicates the bond strength by integrating the band structure energy to the Fermi energy [136]–[139]. A larger absolute value of IpCOHP indicates a stronger bond interaction [137], [140], [141].

3.4.4 Radial Distribution Function

Radial distribution function (RDF) analysis was applied to investigate the structures of LiCl-KCl salt and the influence of Ni and Cr solutes on the structure. RDF is normally used for describing a liquid phase, which is defined as:

$$g_{\alpha\beta}(r) = \frac{1}{4\pi\rho_{\beta}r^2}\left[\frac{dN_{\alpha\beta}(r)}{dr}\right] \qquad (1)$$

where, ρ_{β} is the number density of species β, and $N_{\alpha\beta}(r)$ is the mean number of β-type ions lying in a sphere of radius r centered on an α-type [23], [142]–[144]. To obtain better statistics in the QM-MD simulations, the trajectory average of over 2000 snapshots was used to obtain the RDF.

3.4.5 Green-Kubo Formalism

Diffusion constant and viscosity are important transport properties for molten salts. For MD simulations, the Green-Kubo (GK) equation based on the velocity autocorrelation functions (VAF) is an accurate method to calculate these transport properties [106], [145]–[148].

Diffusion is a kinetic process that describes the movement of atoms in materials that is related to phase transformations. In MD simulations, the diffusion constant D can be calculated by integrating the velocity autocorrelation functions $VAF(t)$ using the GK formula below:

$$D = \frac{1}{3}\int_0^\infty VAF(t)dt \qquad (2)$$

As another important transport property of molten salts, viscosity shows a reverse relationship with the diffusion constant. The shear viscosity can be calculated by the shear stress autocorrelation function (SACF) $\langle \prod^{\alpha\beta}(t)\prod^{\alpha\beta}(0)\rangle$ using the GK formula:

$$\eta = \frac{\Omega}{k_B T}\int_0^\infty \langle \prod^{\alpha\beta}(t)\prod^{\alpha\beta}(0)\rangle dt \qquad (3)$$

where $\prod^{\alpha\beta}(t)$ represents the off-diagonal part ($\alpha \neq \beta$) of the stress tensor that contains the dynamical variables of all particles, K_B is the Boltzmann constant, T is the temperature, and Ω is the volume [149].

3.4.6 Two-Phase Thermodynamics Analysis

The Two-Phase Thermodynamics (2PT) is designed to accurately calculate the entropy and free energy of complex liquid systems using an MD trajectory [150]. The 2PT method obtains the vibrational density of states (DoS) from the Fourier transform of the velocity autocorrelation functions from short 20-picoseconds segments of the QM-MD. 2PT analysis partitions the system into a solid-like component (with 0 states at zero frequency) leading to the partition function used for the thermodynamics of the system plus a phase with diffusional modes at zero frequency that is damped at a higher frequency. Finally, the thermodynamic properties are obtained by applying quantum statistics to the solid component and hard-sphere thermodynamics to the diffusional component. The 2PT method is capable of calculating thermodynamic properties of equilibrated and metal-stable systems, as well as their absolute entropies, quantum effects, thermal effects, and quantum specific heat capacities [150]–[152].

In the present work, the MD trajectories used for 2PT analysis were obtained from the equilibrium NVT ensemble simulation (20-ps), and the output frequency of the MD snapshots was set to every 4 fs. Thermophysical properties of LiCl-KCl molten salt including zero-point energy, total energy, entropy, free energy, heat capacity, and fluidicity were calculated using the 2PT method. The fluidicity represents the proportion of diffusional components to the overall thermal properties.

Chapter 4. Enhancing Corrosion Resistance of Zirconium Alloys

4.1 Introduction

Zirconium (Zr) based cladding materials are widely used in commercial nuclear reactors and it is essential to prevent them from water oxidation to avoid serious safety issues in nuclear power plants such as Fukushima nuclear accident. To provide guidelines to design novel Zr alloys with enhanced water oxidation resistance, we performed a first-principles high-throughput screening (HTS) search that is based on the water dissociation mechanism over Zr basal plane. We apply this HTS approach to 53 metal dopants, including transition and non-transition metals, to determine the promising dopants in Zr-X binary alloys with significantly improved resistance to water oxidation. Firstly, the adsorption and dissociation properties of a water molecule on zirconium basal (0001) surface are determined using the density functional theory (DFT) calculations. Then the water dissociation barrier is used as a descriptor for the HTS approach. Next, the neutron cross-section is considered for the realistic applications of Zr-X alloys as cladding materials in nuclear reactions. Finally, the stability is checked for the possibility of processing these binary Zr-X alloys experimentally. According to this study, eight elements Al, Zn, Ge, As, Sn, Sb, Pb, and Bi are screened out as realistic dopants to enhance the water oxidation resistance of Zr-based cladding materials. Particularly, Bi-doped Zr alloy exhibits excellent water oxidation by improved reaction barrier by ~ 0.36 eV.

4.2 Results and Discussion

4.2.1 Water adsorption on Zr (0001) surface

To examine the interaction between water and Zr, we first constructed the water molecule and bulk Zr and then optimized their structures using the PBE-D3 approach. The structure of a free water molecule was optimized in a 10 Å × 10 Å × 10 Å cubic box. The optimize O-H bond distance and H-O-H angle are 0.97 Å and 104.4°, which agree very well with the experimental values of 0.96 Å and 104.4°, respectively [153]. For the hexagonal closest packed (hcp) Zr, the calculated lattice constants are a = 3.16 Å and c = 5.45 Å, which are consistent with the experimental data of a = 3.23 Å and c = 5.15 Å, respectively [154]. Then the Zr (0001) slab model was constructed, as shown in Figure 4.1, with 20 Zr atoms in the slab model.

We first determine the most plausible water adsorption sites on Zr (0001) surface. Both physical and chemical adsorptions are considered for water adsorption. The physical absorption represents the undissociated H_2O molecule on Zr surface while the chemical adsorption means that H and OH species are adsorbed on the surface. Four possible adsorption sites are shown in Figure 4.1(a) are considered for the physical adsorption: (1) top-b, (2) top-h, (3) top-f, and (4) bri (the bridge site between two neighboring Zr atoms). The three top sites represent that an H_2O molecule is located just above a Zr atom, lying flat and facing to the bridge site (top-b), to the hcp stacking site (top-h), and to the fcc stacking site (top-f), respectively, as shown as Figure 4.1 (c-e). For the bri site, the H_2O molecule is standing upright between two Zr atoms, as illustrated in Figure 4.1(b).

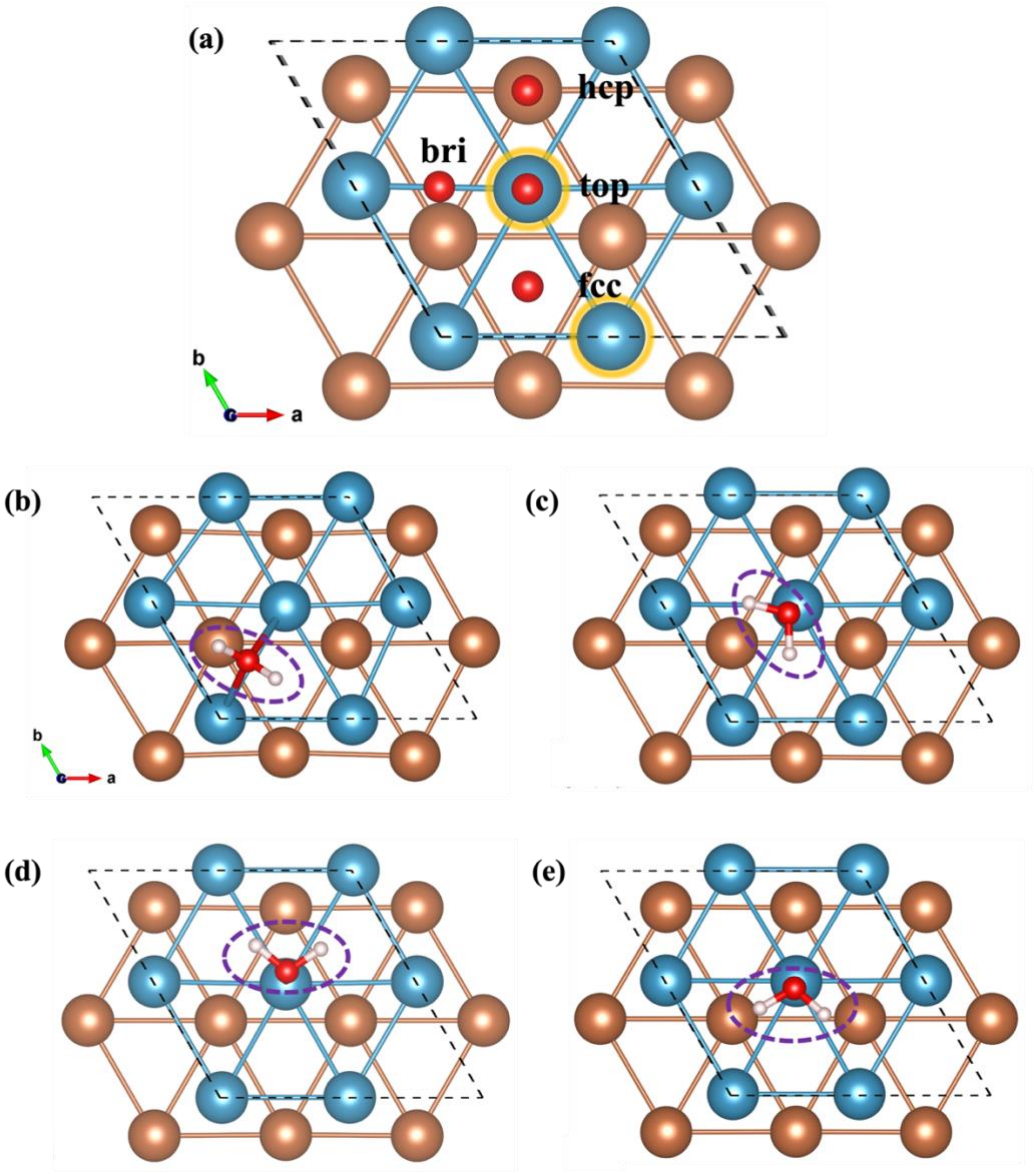

Figure 4.1. (a) Four possible adsorption sites for H_2O molecule showed by the red spheres. The blue and brown spheres represent the top and the second layer, respectively. The two atoms circled by yellow lines indicate the two doping sites that applied to check the favorable adsorption sites of the system; (b-e) The most plausible H_2O molecule configurations on the bridge and top adsorption sites: (b)bri, (c) top-

bri, (d) top-hcp, (e) top-fcc. Water molecules are circled using dashed lines, and the red and white spheres represent O and H atoms, respectively.

The adsorption energy of a water molecule on Zr (0001) surface is defined as

$$E_{ad} = E_{H_2O/Zr(0001)} - E_{H_2O} - E_{Zr(0001)} \qquad (4)$$

where, E_{H_2O} is the energy of a free H_2O molecule in vacuum, $E_{Zr(0001)}$ is the energy of the zirconium slab, and $E_{H2O/Zr(0001)}$ represents the total energy of the whole adsorption system. According to the definition, a negative value of E_{ad} indicates that the adsorption is exothermic (stable), and a system with a lower E_{ad} should be more stable. On the opposite, if E_{ad} is positive, then the absorption reaction is endothermic and not favorable thermodynamically. For the physical adsorption, no O-H bond breaks in the water molecule, leading to a small E_{ad} from -0.650 to -0.634 eV for 4 possible adsorption sites, as listed in Table 3. The structure parameters for different absorption sites are also listed in Table 3.

Table 3. The calculated structural parameters and adsorption energy for a water molecule physically adsorbed on Zr (0001) surface. E_{ad} (eV) represents the physical adsorption energy, z_O (Å), d_{O-H} (Å), and θ (°) are the vertical height of the O atom from the surface, the O-H bond length, and the bond angle of the adsorbed water molecule, respectively.

Adsorption site	**E_{ad} (eV)**	**z_O (Å)**	**d_{O-H} (Å)**	**θ (°)**
top-b	-0.638	2.32	0.988	106.0
top-h	-0.638	2.32	0.988	106.0
top-f	-0.634	2.32	0.988	106.1

bri	-0.650	1.99	0.987	110.8

The energetic differences among these four adsorption states are very small with the E_{ad} of -0.638 eV, -0.638 eV, -0.634 eV, and -0.650 eV for top-b, top-h, top-f, and bri sites, respectively. Therefore, the bridge site is the most stable adsorption site for the water molecule. For the bridge site, the bond angle of the H_2O molecule is 110.8°, which is much larger than that of a free H_2O molecule of 104.4º. This indicates that there is a charge redistribution between the water molecule and the zirconium surface. The O-H bond lengths (0.988 Å) and bond angle (106°) of the H_2O molecule on other sites are relatively close to that of a free H_2O molecule, which is consistent with the relatively small E_{ad}. Previous DFT study [68] without considering van der Waals correction indicated that the top-h adsorption site is more stable than other possible sites. The difference between our simulations and previous studies may arise from the consideration of van der Waals interactions.

Chemical absorption can be divided into two types depending on breaking one or two OH bonds. If one OH bond breaks, the water molecule will break into two parts, an H atom and an OH group, leading to a much larger E_{ad} ~ - 3.0 eV. For the 2nd type of chemical adsorption, the hydroxyl group could be decomposed into one additional hydrogen atom and one oxygen atom. Therefore, it is essential to determine the H and OH binding sites to understand the water dissociation process over Zr surface. Several possible combinations of the binding sites for H and OH are considered to determine the most stable structure after the water dissociation process. As listed in Table 4, the H and OH prefer to occupy

the fcc and hcp sites, respectively. Here we focus on the first type of chemical adsorption, where only one OH bond breaks. The adsorption energy for three adsorption sites are calculated to be - 3.069 eV, - 3.115 eV, and - 3.069 eV for top-h, top-f, and bri sites, respectively. There is no difference in the adsorption energy of top-h and bri sites because the final positions of H and OH for top-h and bri are the same: H atom moves to the fcc hollow site and OH group moves to the hcp site. This is consistent with previous study [69]. The H and OH configuration of the top-f site is different from the other two sites, leading to a more energy release on the top-f site.

Table 4. Adsorption energy for the final H + OH configurations (chemical adsorption) and the dissociation barriers of a water molecule on Zr (0001) surface. E_{ad} is the chemical adsorption energy for the first type of chemical adsorption (H + OH); $E_{barrier}$ (eV) represents the energy barrier of water dissociation; H Site and OH site indicate the plausible adsorption positions for H atom and OH group, respectively.

site	E_{ad} (eV)	$E_{barrier}$ (eV)	H site	OH site
top-h	-3.069	0.1667	fcc	hcp
top-f	-3.115	0.2564	hcp	fcc
bri	-3.069	0.1686	fcc	hcp

4.2.2 Water dissociation on Zr (0001) surface

For the water dissociation process, only the first step $H_2O \rightarrow H^+ + OH^-$ is considered. According to the adsorption energies of H_2O, OH, and H species, three dissociation paths of the H_2O molecule on the Zr (0001) surface are calculated. The initial states are the H_2O

molecule adopted on three possible sites, top-h, top-f, and bri sites, respectively, as shown in Figure 4.1. After the water molecule is dissociated, the H atom and OH group could occupy the hollow fcc or hcp sites around the surface Zr atom. For the top-h and bri path, the H atom and OH group end up at fcc and hcp sites, respectively. Whereas H atom moves to hcp site and OH group moves to fcc site for the top-f path. CI-NEB method is used to determine the minimum energy paths that can reveal the movement and dissociation of a water molecule on zirconium (0001) surface. Figure 4.2 demonstrates the energy profile of the water dissociation process for three different paths. The energy barriers of water dissociation on bri, top-h, and top-f sites are 0.1686 eV, 0.1667 eV, and 0.2564 eV, respectively. The top-h path has the lowest reaction barrier among these three possible paths. However, the water adsorption energy on the top-h site is 0.0119 eV higher than the ground state bri H_2O adsorption configuration, leading to an overall energy barrier of 0.1786 eV. Therefore, the bri dissociation path is the lowest in energy and the top-h site is the second lowest dissociation barrier of 0.1786 eV. This agrees well with the previous DFT study which suggested that the lowest energy path is the bri site dissociation [68].

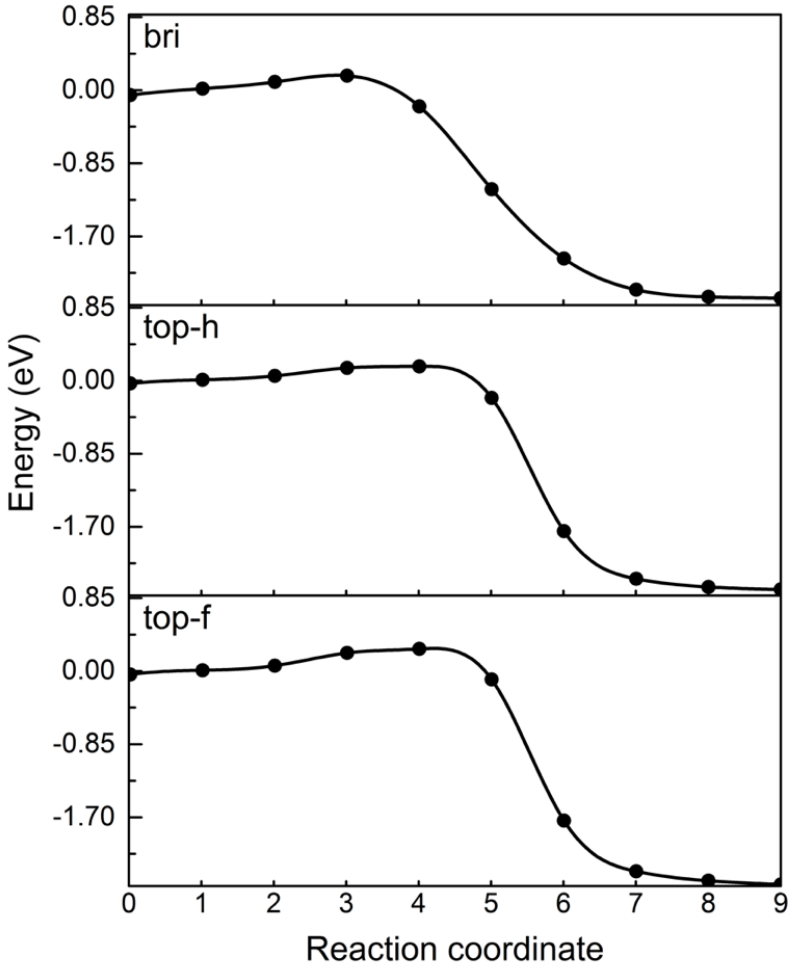

Figure 4.2. CI-NEB energy profile of water dissociation along bri, top-h, and top-f paths. The dissociation energy barriers of bri, top-h and top-f are 0.1686 eV, 0.1667 eV and 0.2582 eV, respectively. Eight images were used in the CI-NEB calculations.

The structure images of the CI-NEB paths are plotted in Figure 4.3 – 4.5. For the bri path, the H_2O molecule first slightly moves towards the hcp site and tilts, as shown in Figure 4.3 (a-c). Then the H_2O molecule reaches the transition state (TS) and starts to decompose (Figure 4.3 (d,e)). Finally, the broken H and OH move to fcc hollow site and

hcp site, respectively (Figure 4.3 (f-j)). For the transition state, the bond length of the longer OH is 1.11 Å and the H-O-H bond angle is 109.83º. At the same time, the distance between the O atom and three nearest surface Zr atoms are 2.44 Å, 2.45 Å, and 2.93Å, respectively.

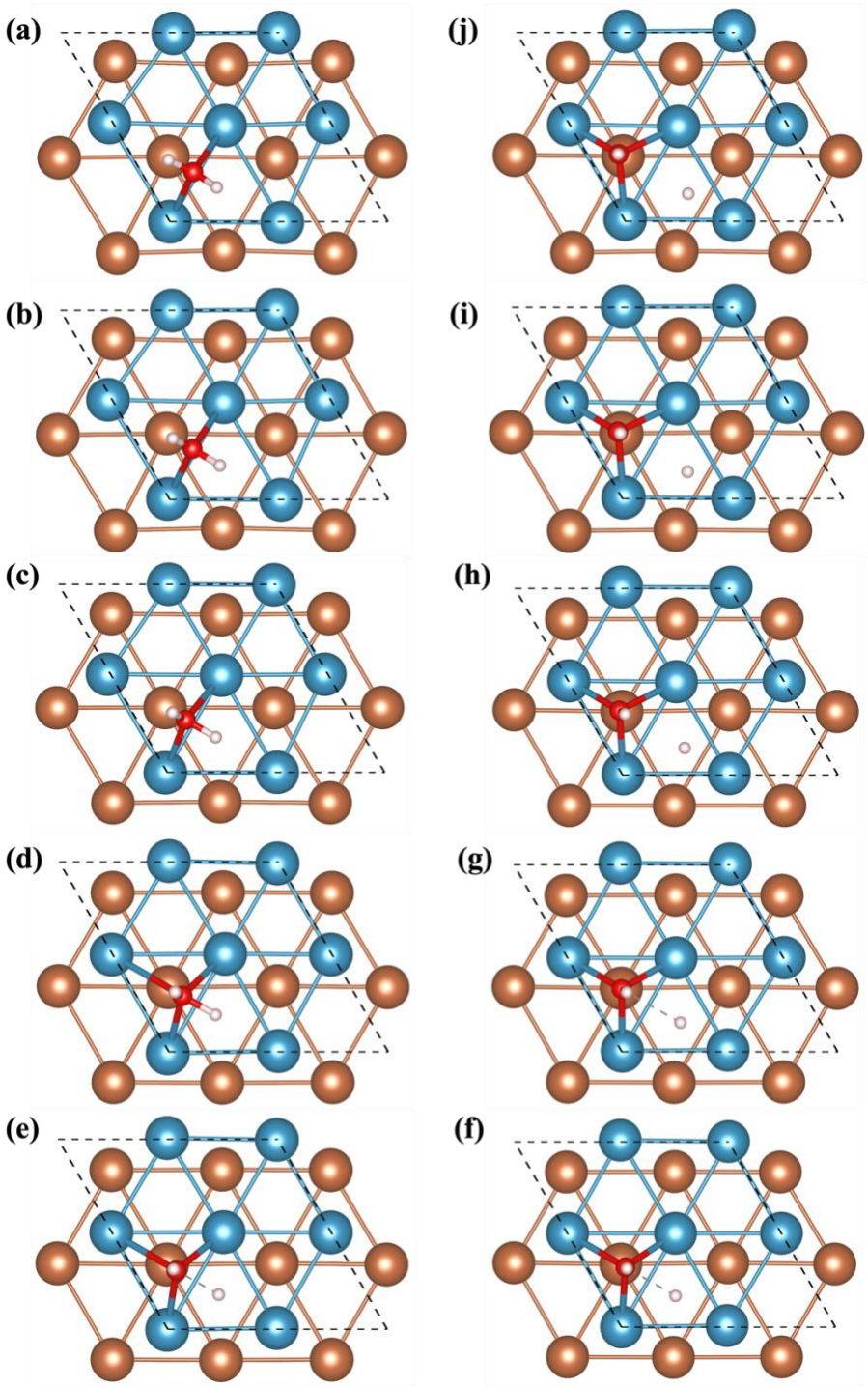

Figure 4.3. CI-NEB images of water dissociation process for bri path. (a-c) The movement of the water molecule toward the hcp site and tilts a little bit with the

increase of one OH bond; (d-e) It reaches the transition state, and the H_2O molecule starts to break into an H atom and an OH group; (f-j) The OH group moves to the hcp site while the H atom moves to the fcc hollow site.

Figure 4.4 displays the CI-NEB path along the top-h path. Firstly, the H_2O molecule moves towards the nearby bri site and rotates around the O atom from a flat-lying configuration to an upright configuration, as shown in Figure 4.4 (a-d). Then the H_2O molecule reaches the TS and starts to dissociate, as shown in Figure 4.4 (f). For the TS structure shown in Figure 4.4 (f), the bond length of the breaking OH bond is 1.02 Å and the H-O-H bond angle is 111.84º. The OH bond length in the TS state is smaller than that in the bri path, while the H-O-H bond angle is larger, leading to a slightly smaller energy barrier. The bond lengths of three Zr-O bonds are 2.34 Å, 2.93 Å, and 3.05 Å, which are less than the corresponding Zr-O bond lengths in the bri path.

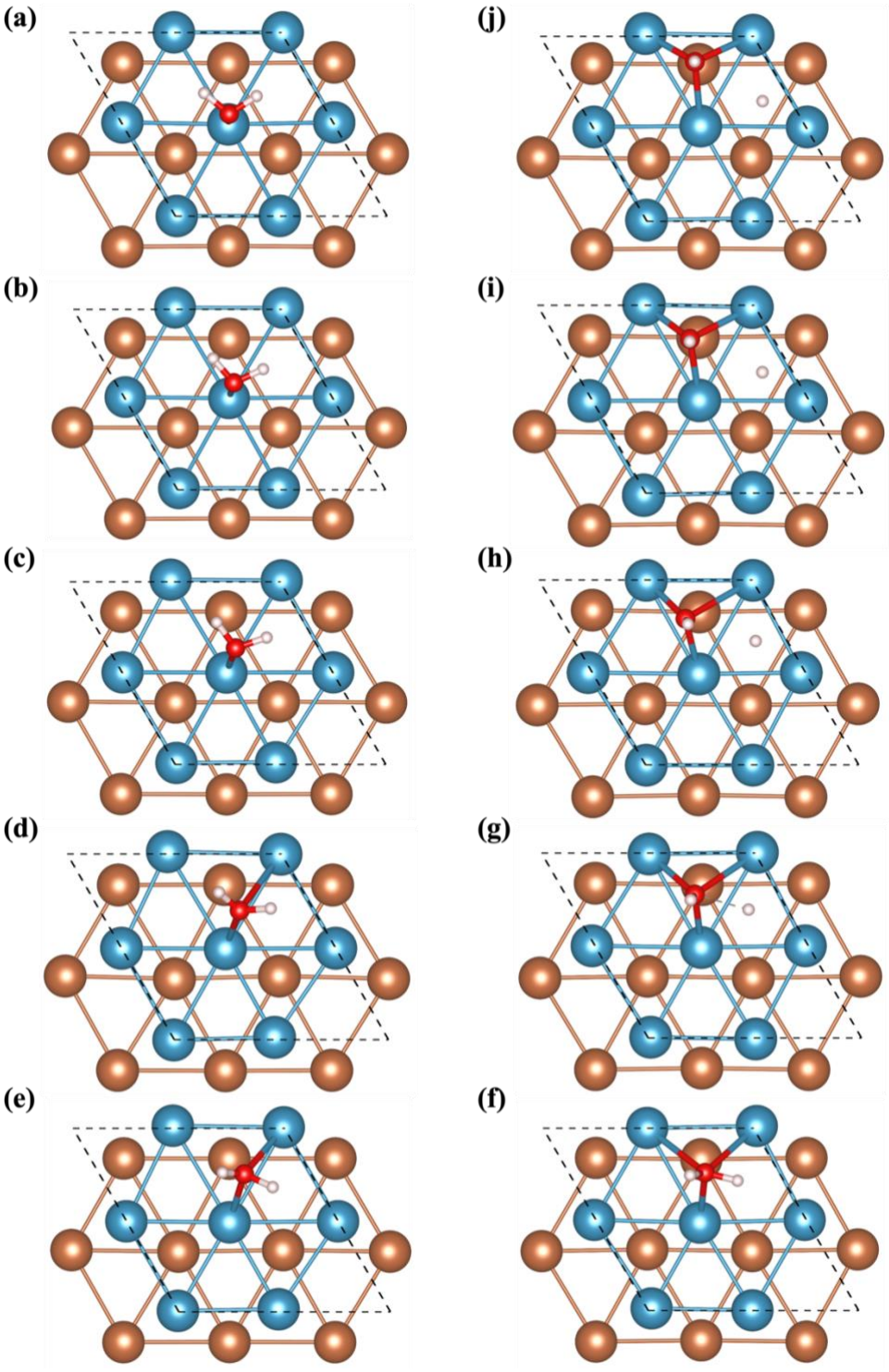

Figure 4.4. CI-NEB images of water dissociation process for the top-h path. (a-d) The movement of H_2O molecule from top-h towards bri site; (e-f) It reaches the transition

state, and the H_2O molecule starts to break; (g-j) The broken H atom and OH group move to the fcc and hcp site, respectively.

The dissociation path of the top-f path is similar to that along the top-h path, as shown in Figure 4.5. In the TS structure, the bond length of the breaking OH bond is 1.01 Å and the H-O-H bond angle is 112.18º, leading to the highest energy barrier of 0.2564 eV. According to the above analyses, the TS structures of top-h and top-f are similar. However, the distance between the O atom and Zr surface for top-h and top-f are approximately 1.95 Å and 1.98 Å, respectively, suggesting that the H_2O molecule on top-f has a weaker interaction with the surface. This leads to a higher energy barrier for water dissociation on the top-f site.

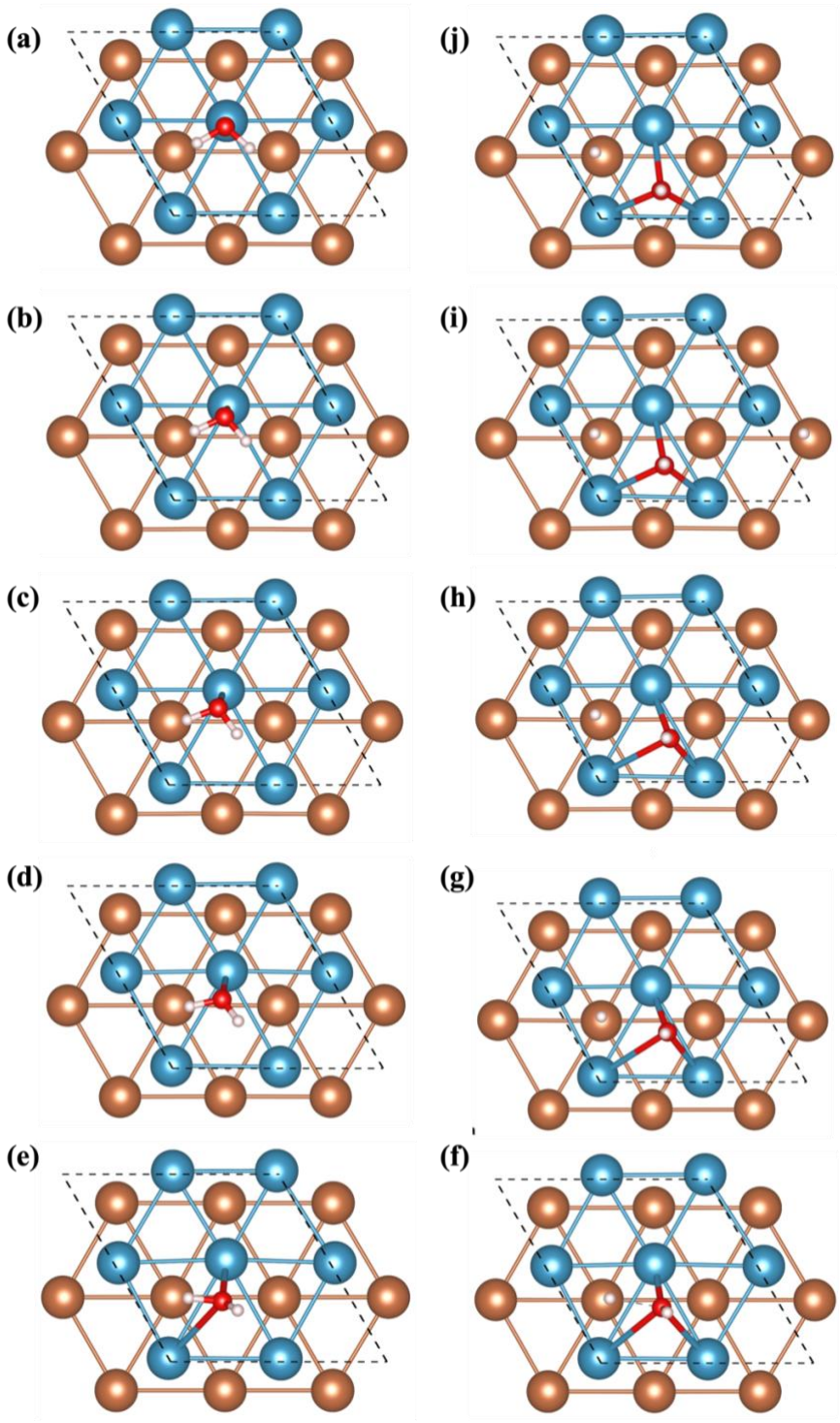

Figure 4.5. CI-NEB images of the water dissociation process for the top-f path. (a-d) similar to the top-h path, the H_2O molecule firstly moves towards the nearest bri site;

(e-f) It reaches the transition state, and the H_2O molecule starts to break; (g-j) The H atom and OH group move to the hcp and fcc sites, respectively.

4.2.3 High throughput screening (HTS)

The HTS approach, displayed in Figure 3.7, was applied to examine the doping effect aiming to screen out a better composition of zirconium alloys that can improve their corrosion resistance. The candidate elements for HTS are 53 non-radioactive metal elements listed in Figure 4.6. One of the Zr atoms on the top layer is substituted by an atom of the doping element, and then the energy barrier of H_2O dissociation was used as the criterion for HTS. The doping strategy is illustrated in Figure 4.7 in which one of the surface Zr atoms is replaced by a Bi atom.

As shown in Figure 4.6, the doping elements chosen for this project are all the metal and metalloid elements from the periodic table, and most of them are transition metals that have similar properties to zirconium. Two doping sites are considered to identify the most stable structure of the doped system: one is the atom right under the H_2O molecule, the other is the surface Zr atom next to it, as shown in Figure 4.1 (a).

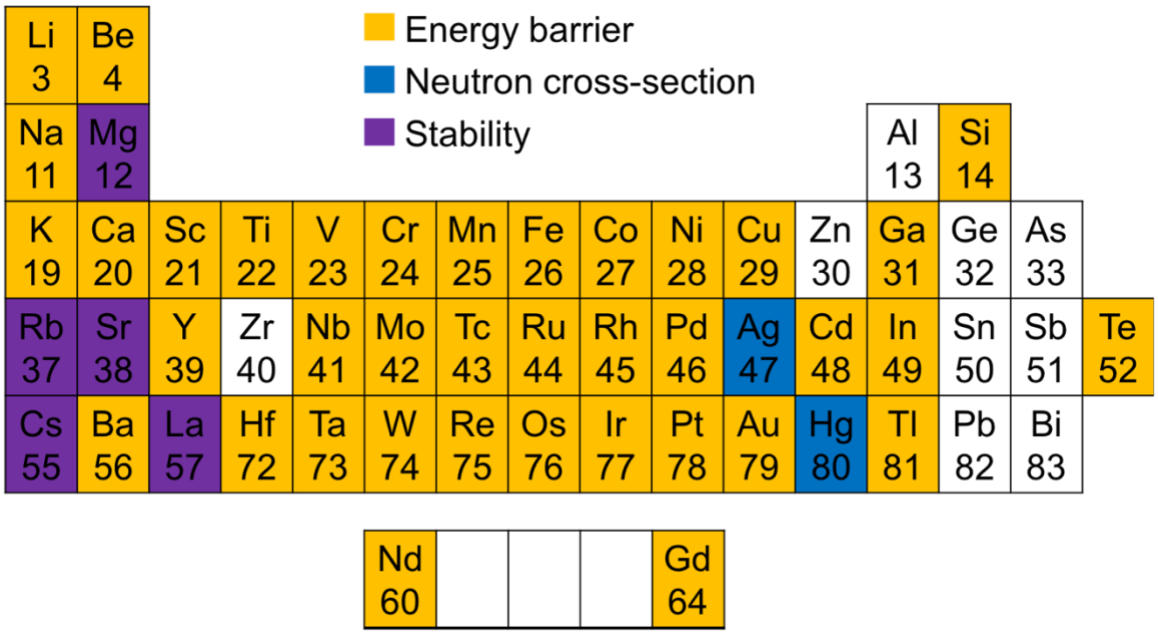

Figure 4.6. A portion of the periodic table selected for HTS. The screening criteria are indicated in colors, the elements are highlighted using the color of the criterion that has sifted them out.

Criterion – 1: Energy barrier of water dissociation

A qualified dopant should be able to prevent the water molecule from reacting with the alloy, in other words, increasing the energy barrier of the water dissociation process. A higher dissociation energy barrier means the system needs more energy to overcome, which makes the O-H bond harder to break. The overall dissociation energy barrier for pure zirconium system is 0.1686 eV, so the first screening criterion can be expressed as

$$\text{Criterion 1: } E_{barrier} \geq 0.1686 \text{ eV}$$

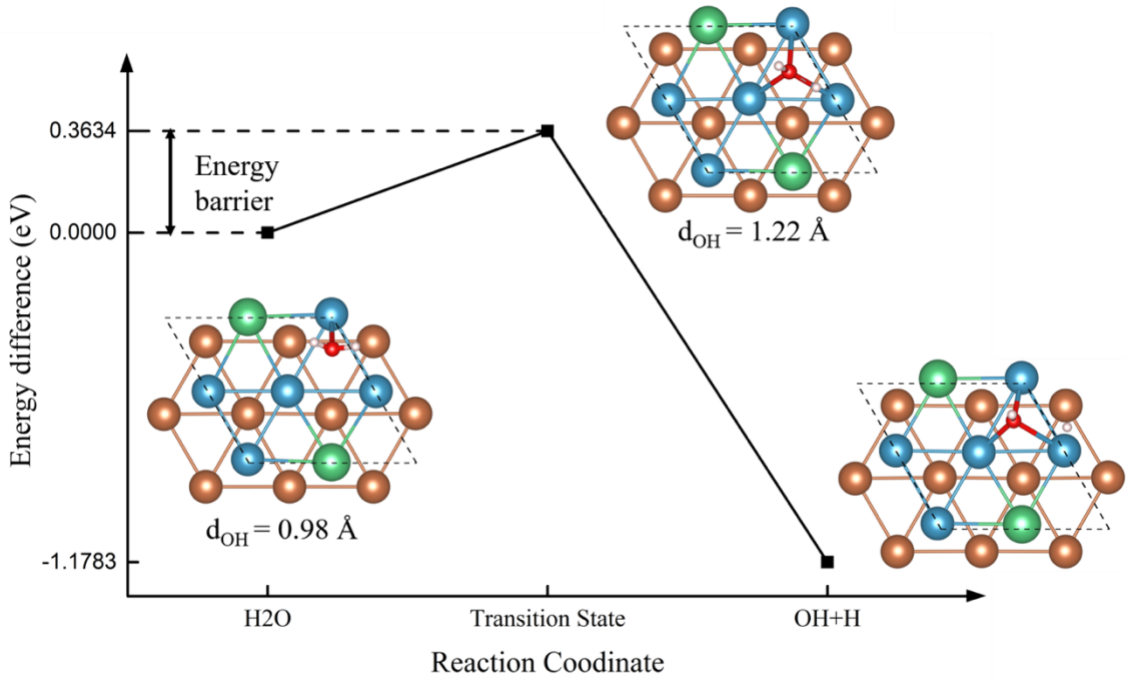

Figure 4.7. The reaction path, the energy barrier, and structures of water dissociation of the best binary doped system Zr-Bi. The green spheres represent dopant Bi atoms.

The dissociation energy barriers of the doped system are calculated for both bri and top-h dissociation paths. The top-f site is not considered here since it has a much higher barrier for pure Zr. Firstly, we determine the most stable water adsorption site (bri vs top-h) by computing the adsorption energy on both bri and top-h adsorption sites. In this process, the water molecule is directly decomposed after being added to the top-h site of Ir- and Pt-doped system, or to the bri site of Ca-, Ba-, W-, and Rh-doped systems, suggesting that the water dissociation barrier is less than zero for these doped systems and these elements are eliminated. Some elements, such as Cs, are not stable on the Zr surface and move to the

vacuum. Therefore, element Cs is also eliminated. Except for these seven eliminated elements, the water molecule is stable on the other 46 elements. However, one site is much preferable to the other site for some elements and the water molecule moves to the preferable site even it is added to the other site. Particularly, the H_2O molecule moves to the top-h adsorption site even it was added to the bridge site for Ga-, Si-, Hg- and Te-doped systems. The H_2O molecule is reversely moved to the bri dissociation site from the initial top-h site for the 13 elements La, Rb, Zn, Sr, K, Mn, Re, Ni, Co, Tc, Ru, Ti, and Mo. Therefore, we only consider the dissociation path along with the favorable adsorption site for these 17 doped systems.

For the left 29 elements in which the water molecule is stable at both sites, we will consider both reaction paths, but the lowest overall barrier of water dissociation will be used in criterion – 1. However, a more efficient approach is applied here for fast screening. For the preferable doping site that has a lower water adsorption energy, we first examined the reaction barrier of water dissociation at this site. If the energy barrier does not satisfy criterion – 1, this element will be eliminated directly. The water dissociation on the higher adsorption site will only be considered if the dissociation on its preferable site satisfies criterion – 1. For example, we first consider the dissociation barrier the at bri site for the doped systems that have lower desorption energy at the bri site. If the energy barrier of the bri dissociation path is smaller than 0.1686 eV, these elements are screened out directly. If it is higher than 0.1686 eV, the water dissociation on the top-h site will be computed. For the doped elements that need to consider two dissociation paths, we will use the overall barrier that is the lowest barrier for the water dissociation. When comparing the barriers on

these two sites, it is worth noting that the energy difference between bri and top-h sites should be added to the reaction barrier.

According to the computed energy barriers, we excluded 32 elements including Tl, Gd, Y, Be, V, Ga, Sc, In, Cu, Fe, Mn, Au, Si, Nb, Ta, Mo, Cr, K, Re, Ni, Co, Tc, Ru, Ti, Nd, Te, Cd, Na, Hf, Li, Pd, and Os that are all have a lower overall barrier than 0.1686 eV. This left out 14 promising elements that have a higher overall energy barrier for water dissociation than pure Zr. These 14 remaining elements are plotted in Figure 4.8 as a function of atomic number and their overall energy barriers for water dissociation are listed in Table 5. The 38 elements highlighted with yellow in Figure 4.6 are sifted out, and this leaves 14 elements including Hg, Pb, Sb, La, Sr, Rb, Mg, As, Sn, Bi, Ag, Al, Ge, and Zn.

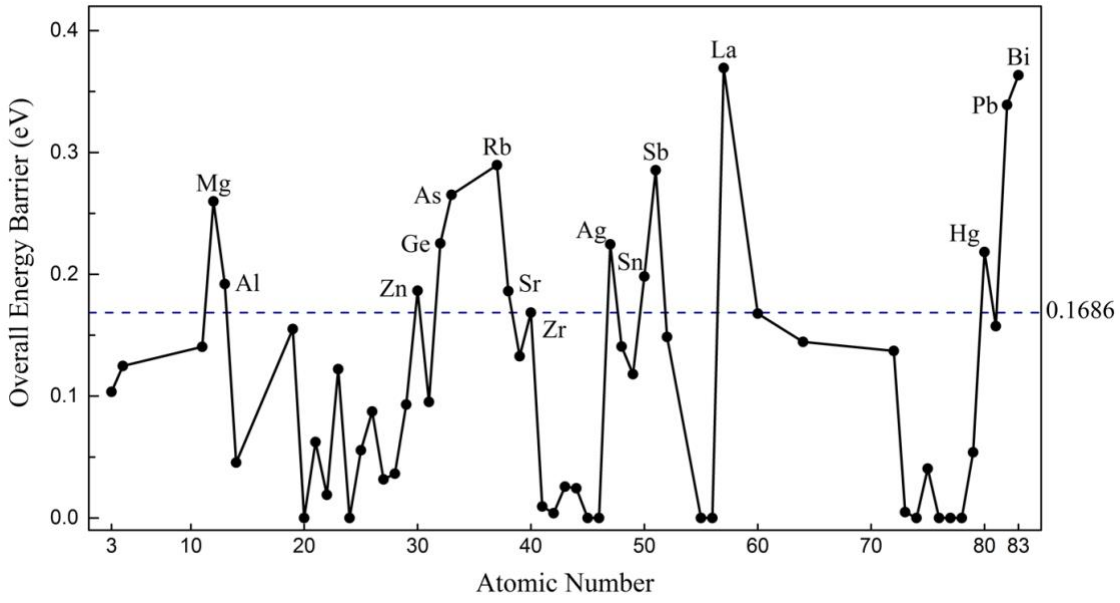

Figure 4.8. Energy barriers of water dissociation for the doped system as a function of atomic number. The Energy barrier for pure zirconium is 0.1686 eV is shown as the horizontal dotted line.

Criterion – 2: Neutron absorption cross-section

Since the designed zirconium alloys will be used as the cladding materials, neutron absorption cross-section is an important criterion to determine the proper doping elements. Cladding materials in a nuclear reactor are supposed to separate the radioactive fission products and surrounding coolants, which means they should absorb thermal neutrons as little as possible to prevent neutron losses. The pure Zr has a small neutron absorption cross-section of 0.184 barn at 0.025 eV neutron energy [155]. The neutron absorption cross-section of other cladding materials currently used in nuclear power plants is lower than 50 relatives to zirconium [46]. Therefore, the second screening criterion is to use the relative neutron absorption cross-section (σ) over pure Zr.

Criterion 2: Relative $\sigma \leq 50$

Neutron absorption cross-section data for the elements are retrieved from Wolfram Research, Inc [155] and are listed in Table 5. As a result, elements Hg and Ag, colored in blue in Figure 4.6, are excluded because of their large neutron absorption cross-sections. This leaves 12 elements including Pb, Sb, La, Sr, Rb, Mg, Sn, As, Bi, Al, Ge, and Zn.

Table 5. The overall energy barriers of water dissociation for the 14 elements pass Criterion-1, as well as their neutron absorption cross-section relative to Zr.

Elements	Overall energy barrier of water dissociation (eV)	Relative neutron absorption cross-section
La	0.3694	48.80
Bi	0.3634	0.18
Pb	0.3449	0.93
Rb	0.2896	2.07
Sb	0.2855	29.35
As	0.2653	22.83
Mg	0.2598	0.34
Ge	0.2253	11.96
Ag	0.2246	345.65
Sn	0.1982	3.37
Al	0.1920	1.27
Hg	0.1869	2032.61
Zn	0.1866	5.98
Sr	0.1862	6.52

Criterion – 3: Stability

This step is to test the stability of the Zr-X alloys in which the dopant elements pass the previous screening steps. This criterion is to determine whether these alloys are stable or have phase separation in binary systems. Therefore, we used the below equations for the stability test.

$$\text{Criterion 3: } E_{formation} = E_{Zr\text{-}X} - E_{Zr} - E_{X} \leq 0$$

where $E_{Zr\text{-}X}$, E_{Zr}, and E_X represent the energies of the doped structure, the electronic energy per atom in HCP Zr crystal, and the crystal phase of dopants, respectively. The formation energy is calculated based on the bulk unit cell so that the dopants could be inserted into bulk Zr experimentally. If $E_{formation}$ is positive, the phase separation between Zr and dopant is preferable, and the system will not be stable. Otherwise, the binary Zr-X alloys are stable and are likely to be synthesized experimentally.

The derived $E_{formation}$ was listed in Table 6 for the stability test. It was found that elements La, Sr, Rb, and Mg are eliminated based on this criterion. Therefore, the remaining elements, such as Pb, Sb, Sn, As, Bi, Al, Ge, and Zn are qualified elements passing all these screening criteria and could be applied to design new zirconium-based cladding materials with improved resistance of water oxidation. Compare with Nie's [69] conclusion that Ge, Sn, Sb, Zn, Ga, Ru, Rh, Pd, Ag, Cr, Mn, Fe, Co, Ni, Cu, Nb, and Mo can increase the oxidation resistance, the difference may result from several aspects: (1) they only considered transition metal as dopants instead of all metallic elements; (2) they compared the water adsorption energy while we compared the dissociation energy barrier; (3) the vdW correction is accounted in our DFT calculations; (4) neutron adsorption cross-sections, an important property of fuel cladding materials, are included in our screening process.

Table 6. Criteria data for the eight promising alloying elements. $E_{barrier}$ is the overall dissociation barrier; Relative σ is the relative neutron adsorption cross-sections compared to zirconium, and $E_{formation}$ represents the results of the stability test.

Elements	$E_{barrier}$ (eV)	Relative σ	$E_{formation}$ (eV)
Bi	0.3634	0.18	-0.97
Pb	0.3449	0.93	-0.61
Sb	0.2855	29.35	-1.83
As	0.2653	22.83	-1.61
Ge	0.2253	11.96	-1.35
Sn	0.1982	3.37	-1.51
Al	0.1920	1.27	-0.88
Zn	0.1866	5.98	-0.29

4.2.4 The best dopant Bi

Based on the HTS process, binary Zr-Bi has the highest water dissociation barrier of 0.3634 eV. The TS search of water dissociation on the Zr-Bi system was illustrated in Figure 4.7 and one can find the initial structure, the TS structure, and the final structure. The critical OH bond length for H_2O molecule dissociation at TS state is 1.22 Å which is larger than that in the pure Zr system. In addition, the Bi has a relatively low neutron absorption cross-section of 5.4 barns (0.184 barns for Zr). Furthermore, the Bi prefers to be mixed with Zr according to the stability calculation. Our prediction that Bi can be inserted into Zr alloy is consistent with the phase diagram shown in Figure 4.9. At the working temperature of zirconium cladding (360°C), the solubility of Bi in Zr is about 3 at% (the most right-side part of the phase diagram). The phase diagram indicated that the Zr can not be inserted into Bi, but Bi can be inserted into Zr. Therefore, our stability criterion is consistent with the phase diagram. In conclusion, Zr-Bi alloy is the best

candidate for the Zr-based cladding materials, and it is worth to be tested experimentally in the future.

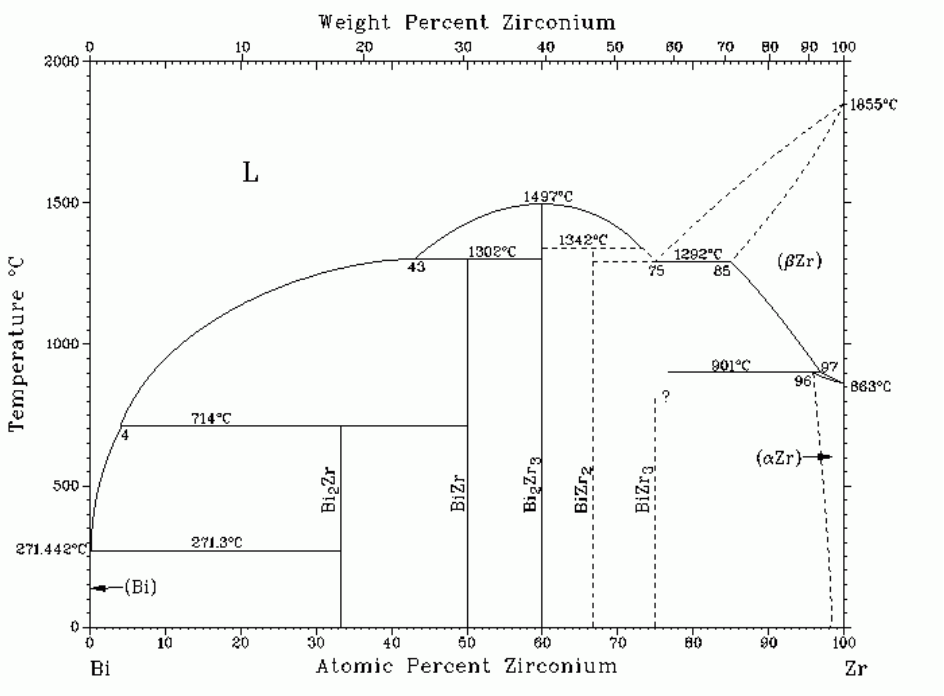

Figure 4.9. The assessed phase diagram of Bi-Zr binary system [156].

4.3 Bonding analysis

In order to illustrate the physical mechanism that why the selected dopants improve the resistance of water oxidation, we characterized the bonding interactions between the water molecule and the zirconium alloy surface using the LOBSTER. Here we select the most promising Zr-Bi alloy to perform the bonding analysis and compare it with pure Zr. Here we compared the IpCOHP value of the two systems, because the absolute value of IpCOHP is a measure of bonding energy [136], [140]. The absolute value of IpCOHP up to the Fermi

energy for Zr-O bond in Bi-doped system is 0.8293 eV, which is smaller than that of the pure Zr system (1.0197 eV). Therefore, the interaction between the surface Zr atom and the O atom is weaker in the Zr-Bi system. That may explain why Bi can improve the oxidation resistance of zirconium alloys.

To further validate the relatively weaker Zr-O bonding interaction in the Zr-Bi system, we plotted the charge density isosurfaces of the Bi-doped system and compared them with the pure Zr system, as shown in Figure 4.10. Compared with pure Zr, fewer charges are localized along the Zr-O bond center in the Zr-Bi system, suggesting that the Zr-O bond in the Bi-doped system is weaker than the undoped system. This is consistent with the IpCOHP analysis. Therefore, the desired dopants in Zr alloys need to weaken the interaction between water and alloys surfaces to suppress the water oxidation.

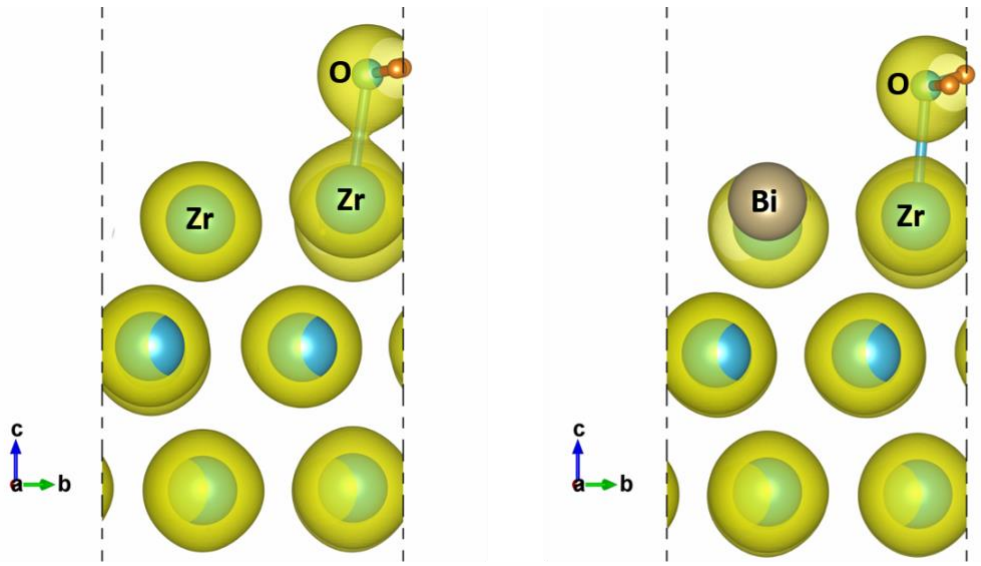

Figure 4.10. The charge density isosurfaces of pure Zr system (a) and Zr-Bi system (b) at a -0.053899 eV^{-3} isosurface level.

4.4 Summary

To investigate the oxidation mechanism of zirconium alloy, we proposed and tested a reaction mechanism-based HTS approach to single out the best binary Zr-X alloy for the cladding materials used in nuclear reactions that use water as coolant. Firstly, the adsorption properties of a water molecule on zirconium (0001) surface are examined using first-principles calculations with vdW correction. The bridge site is the most stable site for water adsorption and dissociation. Then we apply HTS on most metal elements in the periodic table by considering the water dissociation, the neutron absorption cross-section, and the stability. As a result of the HTS process, Al, Zn, Ge, As, Sn, Sb, Pb, and Bi are singled out as promising doping elements that could improve the oxidation resistance of zirconium alloys. The best binary alloy is the Zr-Bi system with the largest water dissociation barrier. Our prediction could be tested experimentally in the future. The reaction mechanism-based HTS approach could be extended to other types of nucleation reactors such as the fourth-generation molten salts reactions. The reaction between cladding materials with molten salts should be considered in this extension.

Chapter 5. Coordination and Thermophysical Properties of Transition Metal Chlorocomplexes in LiCl-KCl Eutectic

5.1 Introduction

Eutectic LiCl-KCl molten salt is often used in molten salt reactors as the primary coolant due to its high thermal capacity and high solubility of fission products. Thermophysical properties, such as density, heat capacity, and viscosity, are important parameters for engineering applications of molten salts, but may be significantly influenced by metal solute from corrosion of metallic structural materials. The behavior of the LiCl-KCl eutectic composition is well-researched, yet the effects on these properties due to chlorocomplex formation from metals dissolved in the salt are less well known. These properties are often difficult to accurately measure from experimental methods due to issues arising from the dissolved species such as volatility. Here we applied a combination of quantum mechanics molecular dynamics (QM-MD) and deep machine learning force field (DP-FF) molecular dynamics simulations to investigate the structure and thermophysical properties of LiCl-KCl eutectic as well as the influence of dissolved transition metal chlorocomplexes $NiCl_2$ and $CrCl_3$ at low concentrations. We find that the dissolution of Ni and Cr in the LiCl-KCl system forms the local tetrahedral $(NiCl_4)^{2-}$ and octahedral $(CrCl_6)^{3-}$ chlorocomplexes, respectively, which do not have a significant impact on the overall liquid salt structures. In addition, the thermodynamic properties including diffusion constant and specific heat capacity are not significantly affected by these chlorocomplexes. However, the viscosity is significantly changed in the temperature range

of 673 ~ 773 K. This study thus provides essential information for evaluating the effects of dissolved metals on the thermophysical and transport properties of molten salts.

5.2 Results and Discussion

5.2.1 Density

Density is a basic yet important structural parameter for materials. The relationship between density and temperature is essential for predicting the thermal expansion of molten salt systems. Experimentally, the density of molten salts is measured by the Archimedean technique [157]. In order to validate our QM-MD and DP-FF simulation approaches, the calculated density of the eutectic LiCl-KCl salt is compared with experimental data obtained in this manner. The equation used for the density calculation from simulations is

$$\rho = \frac{\sum N_i M_i}{N_A V} \qquad (5)$$

where N_i is the moles of component i, M_i is the molar mass of component i, N_A is the Avogadro's constant, and V is the equilibrium volume of the salt systems from NPT simulations.

The calculated densities from QM-MD simulations are plotted in Figure 5.1 (a) as a function of temperature and it is compared with experimental data [107],[158]. The calculated densities decrease from 1.64 g/cm^3 to 1.43 g/cm^3 when temperature increases from 673 to 1173K, as a result of thermal expansion. The QM-MD simulation results agree well with the National Bureau of Standards (NBS) database measured by the Archimedean technique [157]. However, the overall experimental densities measured by Ito *et al.* [107]

are ~ 3% higher than our simulations, which may be caused by the composition difference (58.8 mol% LiCl in the experiment by Ito *et al.*). Nevertheless, the slope of the density-temperature curve from our simulations is almost identical to experimental measurements. From the density-temperature relationship, we predicted that the thermal expansion coefficient (α_V) is 2.96×10^{-4} K^{-1} at 1073 K, which agrees with the experimental value of 2.96×10^{-4} K^{-1} at 1096 K [147]. We conclude that the QM-MD simulations are accurate to predict the density of eutectic LiCl-KCl molten salt. It is worth mentioning that for high temperatures (> 950 K), a larger eutectic salt system containing 128 atoms (38 Li, 64 Cl, 26 K) was used to obtain more accurate densities because of less statistical fluctuation in a larger system.

Figure 5.1 (b) indicates the influence of Ni and Cr solutes on the density of LiCl-KCl eutectic salt. As 3.28 wt% Ni or 2.93 wt% Cr are added, the salt density increases by ~ 3.4% compared to the eutectic salt at the same temperature since both Ni and Cr atoms are heavier. At 773K, the densities of eutectic LiCl-KCl, $NiCl_2$-LiCl-KCl and $CrCl_3$-LiCl-KCl are 1.61 g/cm^3, 1.67 g/cm^3 and 1.66 g/cm^3, respectively. It is interesting to notice that the density of $NiCl_2$-LiCl-KCl is slightly larger than $CrCl_3$-LiCl-KCl at temperatures below 973 K, while it becomes slightly lower at 1073 K. This may arise from the local structure changes of Ni cation at a higher temperature which will be discussed in the next section. To compare with the QM-MD simulations and experiments, DP-FF simulations were performed for obtaining the densities at the same temperature, and the results are plotted in Figure 5.1 (c). The DP-FF results agree very well with the QM-MD results and are more linear because of the large simulation cell. The densities of eutectic LiCl-KCl in QM-MD

and DP-FF simulations are almost the same, and the differences for $NiCl_2$- LiCl-KCl or $CrCl_3$-LiCl-KCl salt systems are within 2%. The density difference between $NiCl_2$-LiCl-KCl or $CrCl_3$-LiCl-KCl becomes less as temperature increases which is consistent with QM-MD, although the density of $NiCl_2$-LiCl-KCl remains larger at 1073 K. For DP-FF MD calculation, the thermal expansion coefficients for $NiCl_2$-LiCl-KCl and $CrCl_3$-LiCl-KCl are 2.90×10^{-4} K^{-1} and 2.93×10^{-4} K^{-1}, respectively, agreeing very well with QM-MD calculation (3.35×10^{-4} K^{-1} for $NiCl_2$-LiCl-KCl and 2.75×10^{-4} K^{-1} $CrCl_3$-LiCl-KCl). It is worth noting that small simulation systems (~100 atoms) were used in QM-MD simulations, leading to a relatively larger fluctuation in the volume. This may cause a relatively large difference in thermal expansion coefficient between $NiCl_2$-LiCl-KCl and $CrCl_3$-LiCl-KCl from QM-MD simulations. We consider that the simulation results from DP-FF are more accurate because of the much larger supercells in the simulations. The thermal expansion coefficient is very close for $NiCl_2$-LiCl-KCl and $CrCl_3$-LiCl-KCl systems from our DP-FF MD simulations.

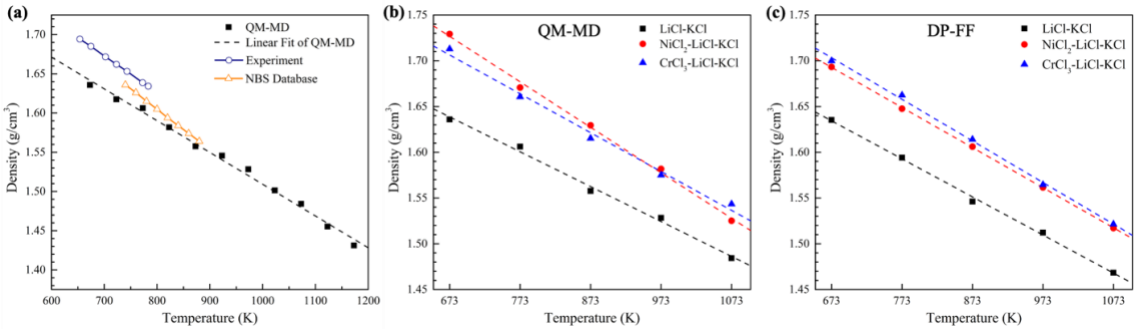

Figure 5.1. Densities (ρ) vs. temperature (T) for LiCl-KCl eutectic with/without metal solutes. (a) QM-MD derived ρ vs. T for LiCl-KCl eutectic and the comparison with experimental data and NBS database. (b) QM-MD derived ρ vs. T for LiCl-KCl

eutectic, 3.28 wt% Ni solute, and 2.93 wt% Cr solute. (c) DP-FF derived ρ vs. T for LiCl-KCl eutectic, 3.28 wt% Ni solute, and 2.93 wt% Cr solute. Dashed lines represent the linear fitting of various datasets.

5.2.2 Structure Characterization

Radial distribution function (RDF) analysis was applied to investigate the structures of LiCl-KCl salt and the influence of Ni and Cr solutes on the structure. RDF is normally used for describing a liquid phase, which is defined as:

$$g_{\alpha\beta}(r) = \frac{1}{4\pi\rho_\beta r^2}\left[\frac{dN_{\alpha\beta}(r)}{dr}\right] \qquad (6)$$

where, ρ_β is the number density of species β, and $N_{\alpha\beta}(r)$ is the mean number of β-type ions lying in a sphere of radius r centered on an α-type. To obtain better statistics in the QM-MD simulations, the trajectory average of over 2000 snapshots was used to obtain the RDF.

Figure 5.2 (a) displays the QM-derived total RDF curves of LiCl-KCl eutectic from 673 K to 1173 K, and the partial RDFs of Li-Cl and K-Cl are plotted in Figure 5.2 (b) and Figure 5.2 (c) respectively. The position of the first RDF peaks barely moved as temperature increased, indicating the mean distance of these ion pairs did not change significantly. From the RDF, we determined the average Li-Cl and K-Cl distances are ~ 2.3 and 3.2 Å (the peak of partial RDF), respectively, which are close to experimental values (2.31 and 3.08 Å) at 668 K [159]. The RDF peaks become broader when temperature

increases, which indicates a larger bond function between anion-cation pairs. As 3.28 wt% Ni or 2.93 wt% Cr solute is added, the total RDF and partial RDFs do not change significantly due to the small concentration of formed $NiCl_2$ and $CrCl_3$, as shown in Figure 5.2 (d–f) and Figure 5.2 (e–f), respectively. Therefore, the dissolved Ni and Cr have no significant influence on the overall structure of molten LiCl-KCl.

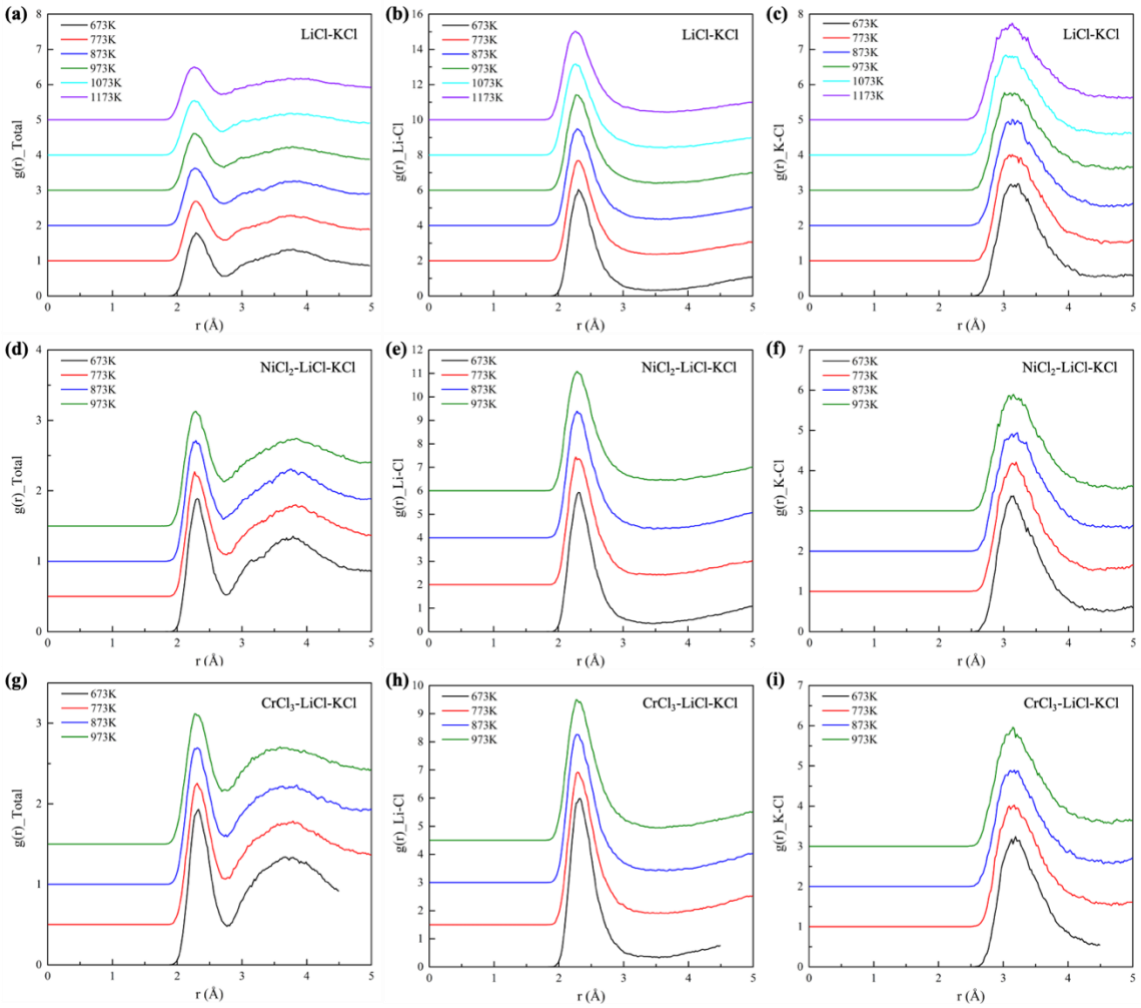

Figure 5.2. RDF curves of the total, Li-Cl, and K-Cl ion pairs for LiCl-KCl based molten salt systems calculated by QM-MD. (a-c) are for LiCl-KCl eutectic

composition, (d-f) are for 3.28 wt% Ni solute in LiCl-KCl, and (g-i) are for 2.93 wt% Cr solute in LiCl-KCl.

Figure 5.3 (a, b) shows the partial RDF of Ni-Cl and Cr-Cl in the salts, respectively, derived from the QM-MD trajectory. For comparison, the RDF was also computed from DP-FF MD simulations. The overall characters and peak positions from DP-FF are close to the QM-MD results, suggesting that the DP-FF can accurately describe the structure of the molten salts.

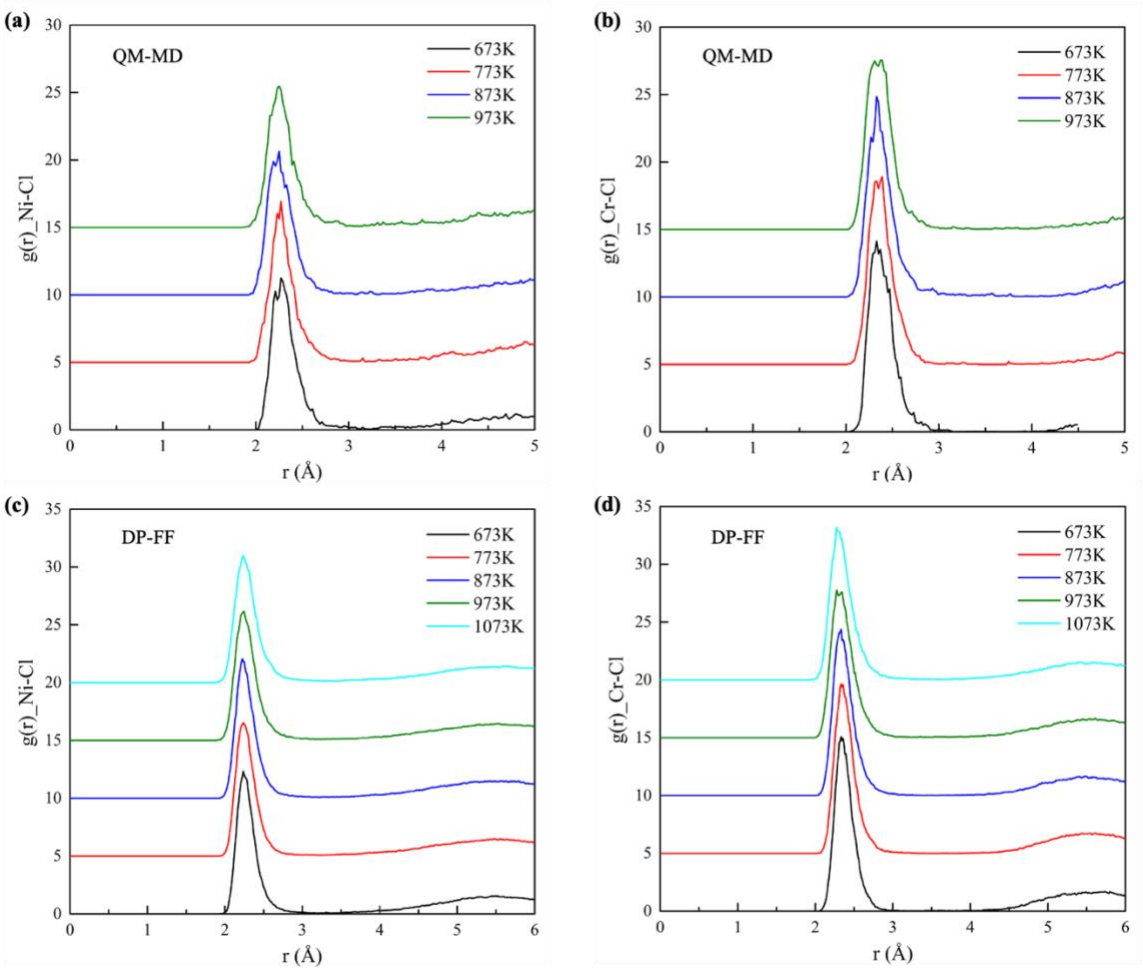

Figure 5.3. RDF analysis of Ni-Cl (a,c) and Cr-Cl (b,d) from QM-MD trajectories and DP-FF MD trajectories, respectively.

The coordination number, the number of anions surrounded at a certain distance near the cations, is a useful parameter to study the local structures of ions. The coordination number is the integration of RDF $g_{\alpha\beta}(r)$, which can be calculated using the following equation,

$$N_{\alpha\beta}(r) = 4\pi\rho_{\beta}\int_{0}^{r_{min}} g_{\alpha\beta}(r)r^2 dr \quad (7)$$

where, r_{min} is the equilibrium distance where RDF reaches the first valley, as shown in Figure 5.4 (a). The r_{min} values are then located in the coordination curve to find the coordination number, as shown in Figure 5.4 (b). For example, the r_{min} of Li-Cl, K-Cl, and Cr-Cl in $CrCl_3$-LiCl-KCl at 773K are 3.3 Å, 4.4 Å, and 3 Å, respectively (Figure 5.4 a). We then used the r_{min} value to determine the coordination numbers of Li-Cl, K-Cl, and Cr-Cl in Figure 5.4 (b), which are around 4, 7.2, and 5.6, respectively, consistent with previous MD simulations [28]. The previous MD simulations suggested that a larger coordination number of K-Cl results from a longer K-Cl bond combined with fast cation diffusion in the eutectic compared to pure KCl [28].

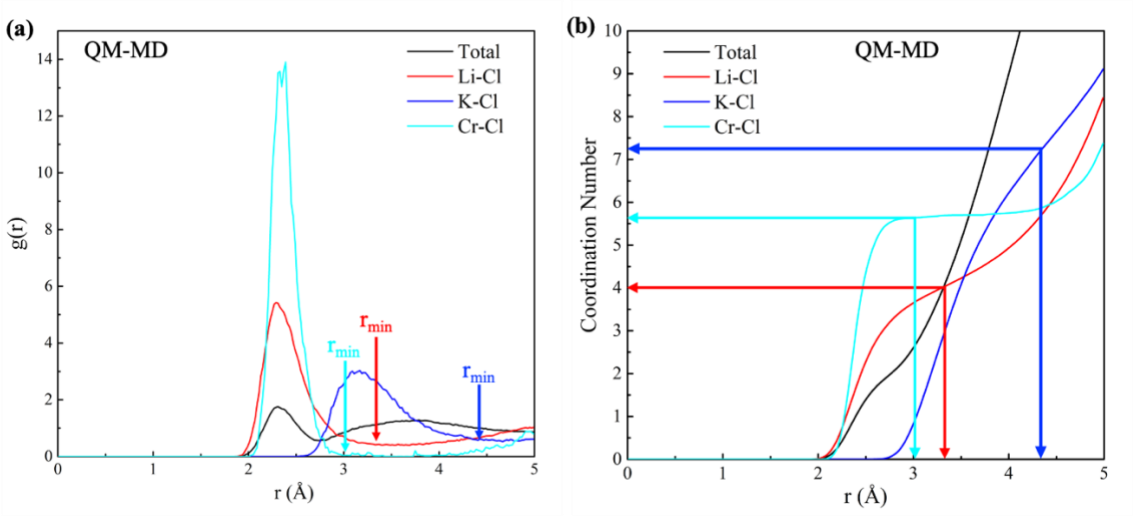

Figure 5.4. QM-MD calculated RDF and coordination number curves of $CrCl_3$-LiCl-KCl at 773K.

The coordination numbers of Li-Cl, K-Cl, Ni-Cl, and Cr-Cl at different temperatures are calculated and shown in Figure 5.5 for both QM-MD and DP-FF MD. The change of coordination numbers as a function of temperature is overall consistent between QM-MD and DP-FF MD. The coordination number decreases a little bit as temperature increases for all ion pairs. From Figure 5.5 (a) and Figure 5.5 (d), the coordination number of Li-Cl and K-Cl in eutectic LiCl-KCl are around 4 and 7, respectively, and they slightly decrease as temperature increases. It is interesting to note that the Ni-Cl coordination number decreases from ~ 4.4 to 4 between 673 K and 773 K; this supports prior observations in $ZnCl_2$ molten salt systems that $NiCl_2$ (in the form of $NiCl_4^{2-}$ that is typically observed in chloride melts) adopts a distorted tetrahedral local coordination at lower temperatures [160]. Sundheim and Harrington [161] proposed that this tetrahedral distortion should correlate to a more typical tetrahedral structure as temperature increases, which agrees well

with our results here. The coordination number of K-Cl decreases from 7.5 to 7 for both QM-MD and DP-FF simulations. As for $CrCl_3$-LiCl-KCl, the coordination of K-Cl decreases even more (~ 1) for QM-MD and DP-FF when heated to 973K. Moreover, the coordination number of Cr-Cl pairs also decreases from 6 to 5.5 as temperature increases for QM-MD, and from 5.8 to 5.2 for DP-FF. For the $CrCl_3$-LiCl-KCl system, the slight increase of the Cr coordination number at 773 K may relate to the significant decrease of the K coordination number when Cr attracts more Cl atoms from K.

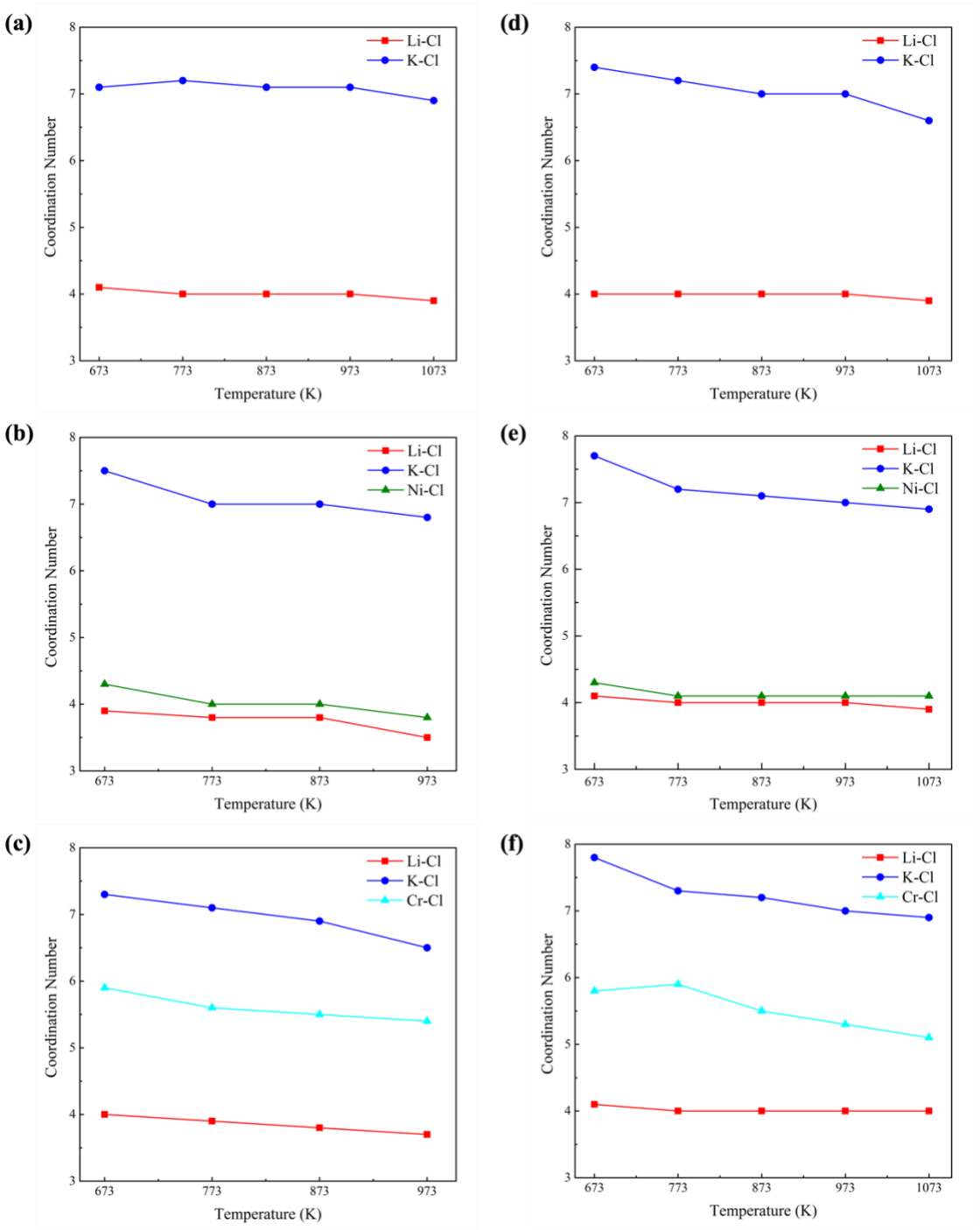

Figure 5.5. The coordination number of Li-Cl, K-Cl, Ni-Cl, Cr-Cl as a function of temperature. (a)-(c) represent results of QM-MD simulations; (d)-(f) represent results of DP-FF MD simulations.

5.2.3 Thermodynamic Properties

The thermodynamic properties of eutectic LiCl-KCl molten salt at different temperatures were analyzed using the 2PT method based on the QM-MD simulations. In Table 7, the diffusion constant, specific heat capacity, Helmholtz free energy, and fluidicity of the molten salt are listed for temperatures ranging from 673 to 1073 K. The diffusion constant describes the mobility of ions, which increase from 1.19×10^{-5} cm^2/s to 5.38×10^{-5} cm^2/s as temperature increases from 673 K to 1073 K. Similarly, fluidicity, a measurement of the percentage of the gas phase density of state (DOS) in the overall DOS, also increases with temperature. The specific heat capacity of each atom calculated by MD simulations is ~ 22.3 J/mol·K, which is consistent with the Dulong–Petit law of ~ 3R (24.9 J/mol·K), where R is the gas constant [162]. Based on the Dulong-Petit method, the specific heat capacity at constant volume (C_v) calculated by our MD simulations is 21.65 J/mol·K at 973K, and the experiment measured heat capacity of LiCl-KCl (59 - 41 mol%) at constant pressure (C_p) is 31.87 J/mol·K at 973K [12]. Considering the fact that C_p is normally larger than C_v by ~ R, our simulation results are close to the experimentally measured value.

Table 7. Thermodynamic properties of eutectic LiCl-KCl molten salt at different temperatures. T, D, C_v, and F represent temperature, diffusion constant, specific heat capacity, and Helmholtz free energy, respectively.

T (K)	D ($\times 10^{-5}$ cm^2/s)	C_v (J/mol·K)	F (kJ/mol)	Fluidicity (%)
673	1.19	22.90	-379.70	14.82
773	2.40	22.30	-385.12	20.47
873	3.12	22.11	-393.19	22.55
973	4.62	21.65	-397.78	26.59
1073	5.38	21.52	-402.44	27.79

Thermodynamic properties of the $NiCl_2$- and $CrCl_3$-LiCl-KCl salt systems were also calculated. To better visualize the influence of Ni and Cr solutes on thermodynamic properties of the LiCl-KCl molten salt, the Helmholtz free energies, specific heat capacities, diffusion constants, and fluidicity are plotted in Figure 5.6 as a function of temperature. Similar to the eutectic LiCl-KCl, Helmholtz's free energy, and specific heat capacity decrease when temperature increases, while diffusion constant and fluidicity increase as temperature increases. As indicated in Figure 5.6, Cr decreases the Helmholtz free energy of the LiCl-KCl salt system, while Ni increases the energy a small amount. The specific heat capacity, diffusion constant, and fluidicity of the system are not significantly affected by the dissolution of Ni and Cr at the low concentration used in this study.

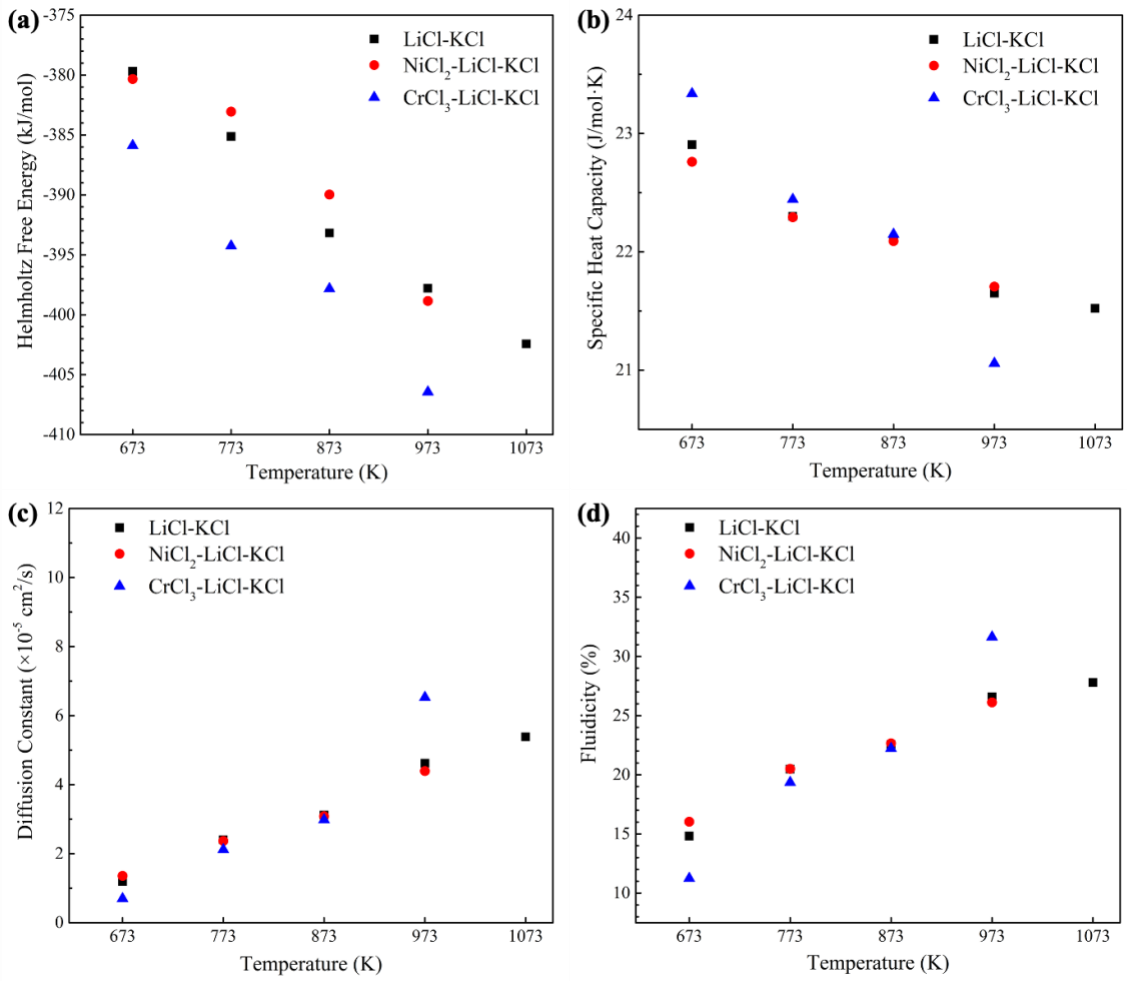

Figure 5.6. Thermodynamic properties of eutectic LiCl-KCl, $NiCl_2$-LiCl-KCl, and $CrCl_3$-LiCl-KCl molten salt systems.

5.2.4 Viscosity

Viscosity describes the resistance to the flow of a liquid, which is a very important thermophysical parameter of molten salts. Viscosity is highly dependent on the temperature of the fluid, and shows an exponential relationship with temperature expressed by the Vogel-Fulcher-Tammann (VFT) equation:

$$\eta = \eta_0 \exp\left(D\frac{T_0}{T - T_0}\right) \qquad (8)$$

where η_0 is the high-temperature limit of viscosity, T_0 is the VFT temperature, and D represents the fragility parameter. We expect that the viscosity of the molten salt decreases exponentially as temperature increases.

Here, the viscosity of LiCl-KCl molten salt at various temperatures were calculated using the DP-FF MD simulations and compared with experimental data. The viscosity of LiCl-KCl eutectic salt increases exponentially as temperature decreases, as shown in Figure 5.7 (a). Compared with experiment measurement, the average viscosity of LiCl-KCl eutectic salt at 973 K is ~ 1.4 centipoise (cP), which is 20% higher than the measured value of 1.15 cP (59.5 mol% LiCl) [163]. The viscosity measured for 58 mol% LiCl-KCl salt at 773 K is 2.2 cP, while the DP-FF MD calculation is 3.5 cP [103]. Overall, the MD simulation results of the viscosity of LiCl-KCl are consistent with experimental measurement. By fitting the VFT equation, we obtained parameters η_0, D, and T_0 of 0.04 cp, 21.2, and 185 K, respectively, for eutectic LiCl-KCl.

Figure 5.7 (b) shows the effects of Ni and Cr solute on the viscosity of eutectic LiCl-KCl. At higher temperatures above 773 K, the viscosity does not significantly change with the addition of Ni (3.28 wt%) and Cr (2.93 wt%). However, the viscosity is significantly increased as temperature decreases to 673 K. By fitting the VTF equation, the η_0, D, and T are 0.2 cP, 2.7, and 370 K for $NiCl_2$-LiCl-KCl; and are 0.44 cP, 0.82, and 507 K for $CrCl_3$-LiCl-KCl. The addition of Ni and Cr makes the eutectic LiCl-KCl salts more viscous. This may influence the MSRs significantly at low working temperatures. It is well

known that the self-diffusion coefficient and viscosity are coupled through the well-known Stokes-Einstein relationship [164], [165]. The self-diffusivity and viscosity correlate very well at high temperature (>= 773K), while at 673 K, the viscosity significantly increases with Ni/Cr while the self-diffusion coefficient does not change significantly. This may be related to the high-temperature Arrhenius behavior to low-temperature non-Arrhenius behavior in the molten salt systems. The local heterogeneity of salt systems may be increased due to the addition of Ni/Cr at low temperature, leading to the unusual viscosity behavior at 673 K. Future study is required to illustrate the physical origin of this interesting phenomenon.

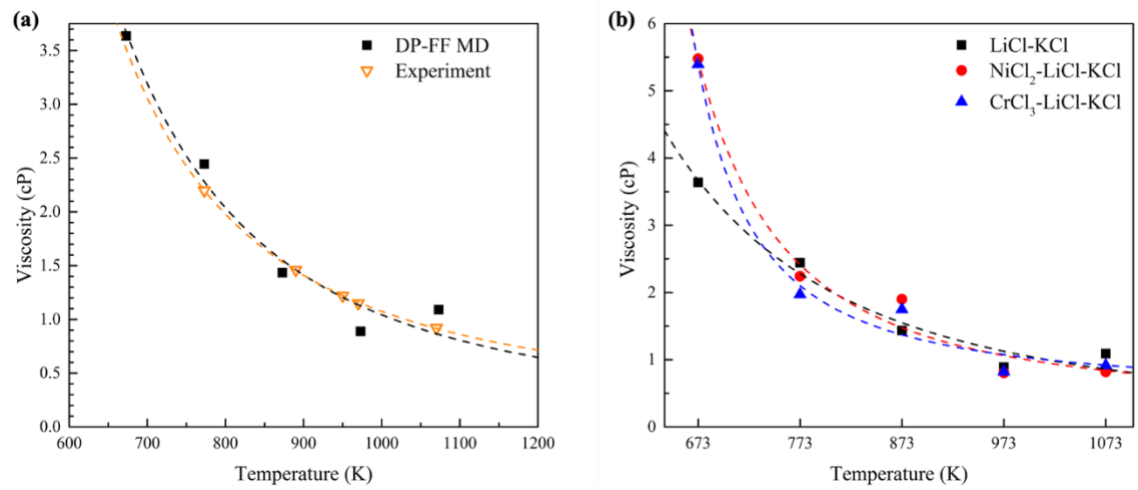

Figure 5.7. (a) Average viscosity of eutectic LiCl-KCl molten salt calculated by DP-FF MD simulations comparing with experiment measurements [103], [163]*; (b) DP-FF MD calculated viscosity of LiCl-KCl, $NiCl_2$-LiCl-KCl, and $CrCl_3$-LiCl-KCl salt systems. Dashed lines represent the exponential fit of different datasets.*

5.3 Summary

In summary, we applied QM-MD and DP-FF MD simulations to determine the density, structural properties, and thermophysical properties of eutectic LiCl-KCl molten salt, as well as the influence of Ni/Cr solutes on these properties. We found that the overall structure of eutectic LiCl-KCl has no significant changes with a lower concentration of Ni/Cr (< 4%), yet the density of the salt systems increases with Ni or Cr solute. For the thermodynamic properties, the dissolution of Ni/Cr in the LiCl-KCl system does not have a remarkable influence on the specific heat capacity, diffusion constant, and fluidicity, yet the Ni/Cr solute significantly increases the viscosity of the eutectic LiCl-KCl salt at 673 K. Our simulation results suggest that the low concentration of Ni or Cr has no significant effect on molten salt systems at high working temperature, but will significantly increase the viscosity at low working temperature, influencing the performance of salt systems at the lower range of working conditions.

Chapter 6. Conclusions

In this dissertation, the corrosion mechanism of metallic materials in nuclear reactors is investigated by combining first-principles calculations and molecular dynamics simulations, including the oxidation of zirconium alloys in a high temperature water environment, and the influence of Ni/Cr solute on the thermodynamic properties of eutectic LiCl-KCl molten salt.

For the enhancement of corrosion resistance of zirconium alloy, we proposed and tested a reaction mechanism based HTS approach to single out the best binary Zr-X alloy for the cladding materials used in nuclear reactions that use water as coolant.

1. The adsorption properties of a water molecule on zirconium (0001) surface are examined using first-principles calculations with vdW correction. It turns out the bridge site is the most stable site for water adsorption and dissociation. The energy barriers of water dissociation are calculated for pure zirconium and Zr-X alloy.

2. 53 transition metal elements are applied to examine the doping effect aiming to screen out a better composition of zirconium alloys that can improve their corrosion resistance. As a result of the HTS process considering the water dissociation, the neutron absorption cross-section, and the stability, Al, Zn, Ge, As, Sn, Sb, Pb, and Bi are singled out as the promising doping elements that could improve the oxidation resistance of zirconium alloys. The best binary alloy is the Zr-Bi system with the largest water dissociation barrier.

The prediction above could be tested experimentally in the future. In addition, the reaction mechanism based HTS approach could be extended to other types of nucleation reactors such as the fourth-generation molten salts reactions. The reaction between cladding materials with molten salts should be considered in this extension.

For the coordination and thermophysical properties of transition metal chlorocomplex in eutectic LiCl-KCl, QM-MD and DP-FF MD simulations are applied to determine the density, structural properties, and thermophysical properties of eutectic LiCl-KCl molten salt, as well as the influence of Ni/Cr solutes on these properties.

1. The DP-FF MD results agree very well with the QM-MD results and are more linear because of the large simulation cell. The densities of eutectic LiCl-KCl in QM-MD and DP-FF simulations are almost the same, and the differences for $NiCl_2$- LiCl-KCl or $CrCl_3$-LiCl-KCl salt systems are within 2%.

2. The overall structure of eutectic LiCl-KCl has no significant changes with a lower concentration of Ni/Cr (< 4%), yet the density of the salt systems increases with Ni or Cr solute. For the thermodynamic properties, the dissolution of Ni/Cr in the LiCl-KCl system does not have a remarkable influence on the specific heat capacity, diffusion constant, and fluidicity, whereas the Ni/Cr solute significantly increases the viscosity of the eutectic LiCl-KCl salt at 673 K.

3. The simulation results suggest that the low concentration of Ni or Cr has no significant effect on molten salt systems at high working temperature, but will

significantly increase the viscosity at low working temperature, influencing the performance of salt systems at the lower range of working conditions.

References

[1] U. DoE, “A Technology Roadmap for Generation IV Nuclear Energy Systems Executive Summary,” Science and Technology (NE), Mar. 2003. doi: 10.2172/859105.

[2] A. Adamantiades and I. Kessides, “Nuclear power for sustainable development: Current status and future prospects,” *Energy Policy*, vol. 37, no. 12, pp. 5149–5166, 2009, doi: 10.1016/j.enpol.2009.07.052.

[3] A. T. Motta, A. Couet, and R. J. Comstock, “Corrosion of Zirconium Alloys Used for Nuclear Fuel Cladding,” *Annu. Rev. Mater. Res.*, vol. 45, no. 1, pp. 311–343, Jul. 2015, doi: 10.1146/annurev-matsci-070214-020951.

[4] F. Alam, R. Sarkar, and H. Chowdhury, “Nuclear power plants in emerging economies and human resource development: A review,” *Energy Procedia*, vol. 160, no. 2018, pp. 3–10, Feb. 2019, doi: 10.1016/j.egypro.2019.02.111.

[5] D. O. Northwood, “The Development and Applications of Zirconium Alloys,” *Mater. Des.*, vol. 6, no. 2, pp. 58–70, 1985, [Online]. Available: https://doi.org/10.1016/0261-3069(85)90165-7.

[6] M. K. Asundi and S. Banerjee, “Zirconium Alloys as Cladding and Structural Materials for Water Cooled Reactors,” *Mater. Sci. Forum*, vol. 48–49, pp. 201–220, Jan. 1991, doi: 10.4028/www.scientific.net/MSF.48-49.201.

[7] B. Cox, “Some thoughts on the mechanisms of in-reactor corrosion of zirconium

alloys," *J. Nucl. Mater.*, vol. 336, no. 2–3, pp. 331–368, 2005, doi: 10.1016/j.jnucmat.2004.09.029.

[8] J. Serp *et al.*, "The molten salt reactor (MSR) in generation IV: Overview and perspectives," *Prog. Nucl. Energy*, vol. 77, pp. 308–319, Nov. 2014, doi: 10.1016/j.pnucene.2014.02.014.

[9] World Nuclear Association, "Generation IV Nuclear Reactors: WNA - World Nuclear Association," *WNA Info Library*, 2019. .

[10] F. Gralla, D. J. Abson, A. P. Møller, D. J. Lang, and H. von Wehrden, "Energy transitions and national development indicators: A global review of nuclear energy production," *Renew. Sustain. Energy Rev.*, vol. 70, no. September 2015, pp. 1251–1265, Apr. 2017, doi: 10.1016/j.rser.2016.12.026.

[11] M. Ho, E. Obbard, P. A. Burr, and G. Yeoh, "A review on the development of nuclear power reactors," *Energy Procedia*, vol. 160, pp. 459–466, Feb. 2019, doi: 10.1016/j.egypro.2019.02.193.

[12] J. W. Mcmurray *et al.*, "Multi-Physics Simulations for Molten Salt Reactor Evaluation: Chemistry Modeling and Database Development," Oak Ridge, TN (United States), Jun. 2018. doi: 10.2172/1492183.

[13] World Nuclear Association, "Molten Salt Reactors - World Nuclear Association," *World Nuclear Association*, 2016. .

[14] Y. Zhang *et al.*, "First principles calculation of redox potential for tetravalent actinides in molten LiCl–KCl eutectic based on vertical substitution and

relaxation," *Electrochim. Acta*, vol. 293, pp. 466–475, 2019, doi: 10.1016/j.electacta.2018.10.016.

[15] Y. Sakamura *et al.*, "Measurement of standard potentials of actinides (U,Np,Pu,Am) in LiCl-KCl eutectic salt and separation of actinides from rare earths by electrorefining," *J. Alloys Compd.*, vol. 271–273, pp. 592–596, 1998, doi: 10.1016/S0925-8388(98)00166-2.

[16] J. Song, X. Li, S. Shi, L. Yan, T. Jiang, and S. Peng, "Towards the calculations of redox potentials in molten LiCl-KCl eutectic by ensemble averages based on first principles molecular dynamics," *Electrochim. Acta*, vol. 248, pp. 462–469, 2017, doi: 10.1016/j.electacta.2017.07.090.

[17] P. Masset, R. J. M. Konings, R. Malmbeck, J. Serp, and J. P. Glatz, "Thermochemical properties of lanthanides (Ln = La, Nd) and actinides (An = U, Np, Pu, Am) in the molten LiCl-KCl eutectic," *J. Nucl. Mater.*, vol. 344, no. 1–3, pp. 173–179, 2005, doi: 10.1016/j.jnucmat.2005.04.038.

[18] J. Song, S. Shi, X. Li, and L. Yan, "First-principles molecular dynamics modeling of UCl3 in LiCl-KCl eutectic," *J. Mol. Liq.*, vol. 234, pp. 279–286, 2017, doi: 10.1016/j.molliq.2017.03.099.

[19] P. Masset *et al.*, "Electrochemistry of Uranium in Molten LiCl-KCl Eutectic," *J. Electrochem. Soc.*, vol. 152, no. 6, p. A1109, 2005, doi: 10.1149/1.1901083.

[20] Y. H. Cho, S. E. Bae, Y. J. Park, S. Y. Oh, J. Y. Kim, and K. Song, "Electronic Structure of U (III) and U (IV) Ions in a LiCl-KCl eutectic melt at 450°C,"

Microchem. J., vol. 102, pp. 18–22, 2012, doi: 10.1016/j.microc.2011.05.006.

[21] K. Fukasawa, A. Uehara, T. Nagai, N. Sato, T. Fujii, and H. Yamana, "Thermodynamic properties of trivalent lanthanide and actinide ions in molten mixtures of LiCl and KCl," *J. Nucl. Mater.*, vol. 424, no. 1–3, pp. 17–22, 2012, doi: 10.1016/j.jnucmat.2012.01.009.

[22] R. D. Mariani and D. Vaden, "Modeled salt density for nuclear material estimation in the treatment of spent nuclear fuel," *J. Nucl. Mater.*, vol. 404, no. 1, pp. 25–32, 2010, doi: 10.1016/j.jnucmat.2010.06.022.

[23] J. X. Dai, W. Zhang, C. L. Ren, H. Han, X. J. Guo, and Q. N. Li, "Molecular dynamics investigation on the local structures and transport properties of uranium ion in LiCl-KCl molten salt," *J. Nucl. Mater.*, vol. 511, pp. 75–82, 2018, doi: 10.1016/j.jnucmat.2018.08.052.

[24] J. Wu, J. Wang, H. Ni, G. Lu, and J. Yu, "The influence of NaCl concentration on the (LiCl-KCl) eutectic system and temperature dependence of the ternary system," *J. Mol. Liq.*, vol. 253, pp. 96–112, 2018, doi: 10.1016/j.molliq.2017.11.068.

[25] A. Bengtson, H. O. Nam, S. Saha, R. Sakidja, and D. Morgan, "First-principles molecular dynamics modeling of the LiCl–KCl molten salt system," *Comput. Mater. Sci.*, vol. 83, pp. 362–370, Feb. 2014, doi: 10.1016/j.commatsci.2013.10.043.

[26] M. Hofmeister, L. Klein, H. Miran, R. Rettig, S. Virtanen, and R. F. Singer,

"Corrosion behaviour of stainless steels and a single crystal superalloy in a ternary LiCl-KCl-CsCl molten salt," *Corros. Sci.*, vol. 90, pp. 46–53, 2015, doi: 10.1016/j.corsci.2014.09.009.

[27] J. Wang, J. Wu, Z. Sun, G. Lu, and J. Yu, "Molecular dynamics study of the transport properties and local structures of molten binary systems (Li, Na)Cl, (Li, K)Cl and (Na, K)Cl," *J. Mol. Liq.*, vol. 209, pp. 498–507, 2015, doi: 10.1016/j.molliq.2015.06.021.

[28] M. M. Walz and D. Van Der Spoel, "Direct Link between Structure, Dynamics, and Thermodynamics in Molten Salts," *J. Phys. Chem. C*, vol. 123, no. 42, pp. 25596–25602, Oct. 2019, doi: 10.1021/acs.jpcc.9b07756.

[29] A. Bengtson, H. O. Nam, S. Saha, R. Sakidja, D. Morgan, and D. Morgan, "Molten Salt System," vol. 83, pp. 362–370, 2014.

[30] W. Liang, G. Lu, and J. Yu, "Machine-Learning-Driven Simulations on Microstructure and Thermophysical Properties of MgCl 2 –KCl Eutectic," *ACS Appl. Mater. Interfaces*, vol. 13, no. 3, pp. 4034–4042, Jan. 2021, doi: 10.1021/acsami.0c20665.

[31] Manohar S. Sohal, Matthias A. Ebner, Piyush Sabharwall, and Phil Sharpe, "Engineering Database of Liquid Salt Thermophysical and Thermochemical Properties," Mar. 2010. doi: 10.2172/980801.

[32] "World Nuclear Association. Outline History of Nuclear Energy." https://www.world-nuclear.org/information-library/current-and-future-

generation/outline-history-of-nuclear-energy.aspx.

[33] “World Nuclear Association. Nuclear power reactors.” .

[34] “Nuclear Power Reactors - World Nuclear Association.” https://world-nuclear.org/information-library/nuclear-fuel-cycle/nuclear-power-reactors/nuclear-power-reactors.aspx (accessed Nov. 04, 2021).

[35] P. Breeze, “Nuclear Power,” in *Power Generation Technologies*, no. FEBRUARY, Elsevier, 2019, pp. 399–429.

[36] United States Nuclear Regulatory Commission, “Boiling Water Reactors | NRC.gov,” 2015. https://www.nrc.gov/reactors/bwrs.html (accessed Nov. 21, 2021).

[37] C. J. Rhodes, “The Fukushima Daiichi Nuclear Accident,” *Sci. Prog.*, vol. 97, no. 1, pp. 72–86, Mar. 2014, doi: 10.3184/003685014X13904938571454.

[38] United States Nuclear Regulatory Commission, “Backgrounder on the Three Mile Island Accident,” *United States Nucl. Regul. Comm. Libr.*, 2018.

[39] Tokyo Electric Power Company Inc., “Fukushima nuclear accident analysis report,” 2012. [Online]. Available: https://www.tepco.co.jp/en/press/corp-com/release/betu12_e/images/120620e0104.pdf.

[40] “Three Mile Island: On the 1979 Accident and Its Decommissioning Forty Years Later | American Institute of Physics.” https://www.aip.org/history-programs/niels-bohr-library/ex-libris-universum/three-mile-island-1979-accident-and-its (accessed Nov. 21, 2021).

[41] United States Nuclear Regulatory Commission, “Backgrounder on the Three Mile Island Accident,” *United States Nuclear Regulatory Commission Library*, 2018. https://www.nrc.gov/reading-rm/doc-collections/fact-sheets/3mile-isle.html%0Ahttp://www.nrc.gov/reading-rm/doc-collections/fact-sheets/3mile-isle.html (accessed Nov. 21, 2021).

[42] S. M. Becker, “The Fukushima Dai-Ichi Accident,” *Health Phys.*, vol. 105, no. 5, pp. 455–461, Nov. 2013, doi: 10.1097/HP.0b013e31829c351d.

[43] World Nuclear Association, “Fukushima Accident - World Nuclear Association,” *World Nuclear Association*, 2016. .

[44] I. A. E. A. (IAEA), “The Fukushima Daiichi Accident Report by the Director General,” 2015. Accessed: Nov. 21, 2021. [Online]. Available: https://www-pub.iaea.org/mtcd/publications/pdf/pub1710-reportbythedg-web.pdf.

[45] I. Charit, “Accident Tolerant Nuclear Fuels and Cladding Materials,” *Jom*, vol. 70, no. 2, pp. 173–175, 2018, doi: 10.1007/s11837-017-2701-3.

[46] C. R. F. Azevedo, “Selection of fuel cladding material for nuclear fission reactors,” *Eng. Fail. Anal.*, vol. 18, no. 8, pp. 1943–1962, Dec. 2011, doi: 10.1016/j.engfailanal.2011.06.010.

[47] Z. Duan *et al.*, “Current status of materials development of nuclear fuel cladding tubes for light water reactors,” *Nucl. Eng. Des.*, vol. 316, pp. 131–150, May 2017, doi: 10.1016/j.nucengdes.2017.02.031.

[48] K.-T. Kim, “Evolutionary developments of advanced PWR nuclear fuels and

cladding materials," *Nucl. Eng. Des.*, vol. 263, pp. 59–69, Oct. 2013, doi: 10.1016/j.nucengdes.2013.04.013.

[49] United States Department of Energy, "Anatomy of a Fuel Assembly." https://www.energy.gov/nnsa/downloads/anatomy-fuel-assembly1-19-12pdf (accessed Nov. 21, 2021).

[50] "How is used nuclear fuel managed? ," *World Nuclear Association*. https://world-nuclear.org/our-association/publications/technical-positions/how-is-used-nuclear-fuel-managed.aspx (accessed Dec. 02, 2021).

[51] "Nuclear Power Plants." https://whatisnuclear.com/reactors.html (accessed Dec. 02, 2021).

[52] "Ten years after Fukushima: could new fuels make nuclear power safer? – Physics World." https://physicsworld.com/a/ten-years-after-fukushima-could-new-fuels-make-nuclear-power-safer/ (accessed Dec. 02, 2021).

[53] G. L. Garner, B. A. Hilton, and E. Mader, "Performance of alloy M5® cladding and structure," in *American Nuclear Society - 2007 LWR Fuel Performance/Top Fuel*, 2007, pp. 176–182, Accessed: Dec. 03, 2021. [Online]. Available: http://inis.iaea.org/Search/search.aspx?orig_q=RN:40094652.

[54] A. M. Garde *et al.*, "Advanced Zirconium Alloy for PWR Application," in *Zirconium in the Nuclear Industry: 16th International Symposium*, 100 Barr Harbor Drive, PO Box C700, West Conshohocken, PA 19428-2959: ASTM International, 2012, pp. 784–800.

[55] C. Duriez, T. Dupont, B. Schmet, and F. Enoch, “Zircaloy-4 and M5® high temperature oxidation and nitriding in air,” *J. Nucl. Mater.*, vol. 380, no. 1–3, pp. 30–45, Oct. 2008, doi: 10.1016/j.jnucmat.2008.07.002.

[56] Y. Katoh *et al.*, “Current status and critical issues for development of SiC composites for fusion applications,” *J. Nucl. Mater.*, vol. 367–370, no. SPEC. ISS., pp. 659–671, Aug. 2007, doi: 10.1016/j.jnucmat.2007.03.032.

[57] D. Carpenter, “Comparison of Pellet-Cladding Mechanical Interaction for Zircaloy and Silicon Carbide Clad Fuel Rods in Pressurized Water Reactors,” *Ocw.Edu.Ht*, p. 20, 2006, Accessed: Dec. 03, 2021. [Online]. Available: http://ocw.edu.ht/courses/nuclear-engineering/22-314j-structural-mechanics-in-nuclear-power-technology-fall-2006/projects/carpenter.pdf.

[58] A. M. Pauzi, A. Cioncolini, and H. Iacovides, “Parametric study of natural circulation flow in molten salt fuel in molten salt reactor,” 2015, vol. 1659, p. 030004, doi: 10.1063/1.4916852.

[59] R. N. Wright and T.-L. Sham, “Status of Metallic Structural Materials for Molten Salt Reactors,” Idaho Falls, ID (United States), May 2018. doi: 10.2172/1467482.

[60] W. R. Grimes, “Molten-Salt Reactor Chemistry,” *Nucl. Appl. Technol.*, vol. 8, no. 2, pp. 137–155, Feb. 1970, doi: 10.13182/NT70-A28621.

[61] G. Zheng and K. Sridharan, “Corrosion of Structural Alloys in High-Temperature Molten Fluoride Salts for Applications in Molten Salt Reactors,” *Jom*, vol. 70, no. 8, pp. 1535–1541, 2018, doi: 10.1007/s11837-018-2981-2.

[62] G. F. Flanagan, B. W. Patton, J. C. Gehin, and T. J. Harrison, *Fast Spectrum Molten Salt Reactor Options, ONRL/TM-2011/105*, no. July. 2011.

[63] G. L. Fredrickson, G. Cao, R. Gakhar, and T.-S. Yoo, "Molten Salt Reactor Salt Processing – Technology Status," Idaho Falls, ID (United States), Aug. 2018. doi: 10.2172/1484689.

[64] G. P. Sabol, "ZIRLO™ - An alloy development success," *J. ASTM Int.*, 2005, doi: 10.1520/stp37500s.

[65] B. Cox and Y. M. Wong, "Hydrogen uptake micro-mechanism for Zr alloys," *J. Nucl. Mater.*, vol. 270, no. 1, pp. 134–146, 1999, doi: 10.1016/S0022-3115(98)00898-8.

[66] D. Olander and A. Motta, "Chapter 17 . Zirconium Alloys," in *Light Water Reactor Materials*, 2011.

[67] S. S. Yardley *et al.*, "An investigation of the oxidation behaviour of zirconium alloys using isotopic tracers and high resolution SIMS," *J. Nucl. Mater.*, vol. 443, no. 1–3, pp. 436–443, 2013, doi: 10.1016/j.jnucmat.2013.07.053.

[68] S. X. Wang, P. Zhang, P. Zhang, J. Zhao, and S. S. Li, "Adsorption and dissociation of H 2O on Zr(0 0 0 1) with density-functional theory studies," *J. Nucl. Mater.*, vol. 424, no. 1–3, pp. 51–56, 2012, doi: 10.1016/j.jnucmat.2012.02.007.

[69] Y. Nie and W. Xiao, "Chemical and physical adsorption of a H2O molecule on a metal doped Zr (0 0 0 1) surface," *J. Nucl. Mater.*, vol. 452, no. 1–3, pp. 493–499,

2014, doi: 10.1016/j.jnucmat.2014.05.066.

[70] J. C. Kim, C. J. Moore, B. Kang, G. Hautier, A. Jain, and G. Ceder, “Synthesis and Electrochemical Properties of Monoclinic LiMnBO[sub 3] as a Li Intercalation Material,” *J. Electrochem. Soc.*, vol. 158, no. 3, p. A309, 2011, doi: 10.1149/1.3536532.

[71] L. C. Lin *et al.*, “In silico screening of carbon-capture materials,” *Nat. Mater.*, vol. 11, no. 7, pp. 633–641, 2012, doi: 10.1038/nmat3336.

[72] M. McDonald, J. Fuller, A. Fortunelli, W. A. Goddard, and Q. An, “Highly Efficient Ni-Doped Iron Catalyst for Ammonia Synthesis from Quantum-Mechanics-Based Hierarchical High-Throughput Catalyst Screening,” *J. Phys. Chem. C*, vol. 123, no. 28, pp. 17375–17383, 2019, doi: 10.1021/acs.jpcc.9b04386.

[73] Q. An, Y. Shen, A. Fortunelli, and W. A. Goddard, “QM-Mechanism-Based Hierarchical High-Throughput in Silico Screening Catalyst Design for Ammonia Synthesis,” *J. Am. Chem. Soc.*, vol. 140, no. 50, pp. 17702–17710, 2018, doi: 10.1021/jacs.8b10499.

[74] Y. Shen, H. Wang, B. Li, and Q. An, “First principles high-throughput screening to enhance the ductility of lightweight magnesium alloys,” *Phys. Rev. Mater.*, vol. 3, no. 5, pp. 1–9, 2019, doi: 10.1103/PhysRevMaterials.3.053603.

[75] B. Hoglund, “Molten Salt Energy Technologies.” https://moltensalt.org/.

[76] J. Wang, Z. Sun, G. Lu, and J. Yu, “Molecular dynamics simulations of the local structures and transport coefficients of molten alkali chlorides,” *J. Phys. Chem. B*,

vol. 118, no. 34, pp. 10196–10206, 2014, doi: 10.1021/jp5050332.

[77] K. Sridharan, S. Martin, M. Mohammadian, J. Sager, T. Allen, and M. Simpson, "Thermal properties of LiCl-KCl molten salt for nuclear waste separation," *Trans. Am. Nucl. Soc.*, vol. 106, no. 09, pp. 1240–1241, 2012.

[78] J. Ding *et al.*, "Theoretical prediction of the local structures and transport properties of binary alkali chloride salts for concentrating solar power," *Nano Energy*, vol. 39, no. June, pp. 380–389, 2017, doi: 10.1016/j.nanoen.2017.07.020.

[79] X. Lv, A. Dong, Y. Dai, J. Wang, D. Shu, and B. Sun, "Temperature and concentration dependence of the physical properties and local structures of molten NaCl-KCl-LiCl mixtures," *J. Mol. Liq.*, vol. 229, pp. 330–338, 2017, doi: 10.1016/j.molliq.2016.12.091.

[80] W. Wang, B. Guan, X. Wei, J. Lu, and J. Ding, "Cellular automata simulation on the corrosion behavior of Ni-base alloy in chloride molten salt," *Sol. Energy Mater. Sol. Cells*, vol. 203, no. July, 2019, doi: 10.1016/j.solmat.2019.110170.

[81] J. Zhang, "Electrochemistry of actinides and fission products in molten salts—Data review," *J. Nucl. Mater.*, vol. 447, no. 1–3, pp. 271–284, Apr. 2014, doi: 10.1016/j.jnucmat.2013.12.017.

[82] K. Sridharan and T. R. Allen, "Corrosion in Molten Salts," in *Molten Salts Chemistry*, Elsevier, 2013, pp. 241–267.

[83] J. C. Gomez-Vidal and R. Tirawat, "Corrosion of alloys in a chloride molten salt (NaCl-LiCl) for solar thermal technologies," *Sol. Energy Mater. Sol. Cells*, vol.

157, pp. 234–244, Dec. 2016, doi: 10.1016/j.solmat.2016.05.052.

[84] G. Fredrickson, G. Cao, R. Gakhar, and T. Yoo, “Molten Salt Reactor Salt Processing – Technology Status,” no. August, 2018, [Online]. Available: Idaho National Laboratory; INL/EXT-18-51033; Revision 0.

[85] D. F. Williams, “Assessment of Candidate Molten Salt Coolants for the Advanced High Temperature Reactor (AHTR),” Oak Ridge, TN, Mar. 2006. doi: 10.2172/885975.

[86] E. Mullen, R. Harris, D. Graham, C. Rhodes, and Z. Hodgson, “Transfer characteristics of a lithium chloride–potassium chloride molten salt,” *Nucl. Eng. Technol.*, vol. 49, no. 8, pp. 1727–1732, 2017, doi: 10.1016/j.net.2017.09.001.

[87] J. L. Willit, W. E. Miller, and J. E. Battles, “Electrorefining of uranium and plutonium - A literature review,” *Journal of Nuclear Materials*. 1992, doi: 10.1016/0022-3115(92)90515-M.

[88] Y. SAKAMURA *et al.*, “Separation of Actinides from Rare Earth Elements by Electrorefining in LiC1-KC1 Eutectic Salt,” *J. Nucl. Sci. Technol.*, vol. 35, no. 1, pp. 49–59, Jan. 1998, doi: 10.1080/18811248.1998.9733819.

[89] J. W. Ambrosek, “Molten Chloride Salts for Heat Transfer in Nuclear Systems.,” *Ph.D. Thesis Univ. Wisconsin, Madison, WI.*, pp. 93–95, 2011.

[90] N. Galamba, C. A. Nieto de Castro, and J. F. Ely, “Shear viscosity of molten alkali halides from equilibrium and nonequilibrium molecular-dynamics simulations,” *J. Chem. Phys.*, vol. 122, no. 22, p. 224501, Jun. 2005, doi: 10.1063/1.1924706.

[91] N. Galamba, C. A. Nieto de Castro, and J. F. Ely, “Equilibrium and nonequilibrium molecular dynamics simulations of the thermal conductivity of molten alkali halides,” *J. Chem. Phys.*, vol. 126, no. 20, p. 204511, May 2007, doi: 10.1063/1.2734965.

[92] J. L. Willit, W. E. Miller, and J. E. Battles, “Electrorefining of uranium and plutonium — A literature review,” *J. Nucl. Mater.*, vol. 195, no. 3, pp. 229–249, Nov. 1992, doi: 10.1016/0022-3115(92)90515-M.

[93] A. K. Misra and J. D. Whittenberger, “FLUORIDE SALTS AND CONTAINER MATERIALS FOR THERMAL ENERGY STORAGE APPLICATIONS IN THE TEMPERATURE RANGE 973 TO 1400 K.,” 1987.

[94] L. Olson, K. Sridharan, M. Anderson, and T. Allen, “Nickel-plating for active metal dissolution resistance in molten fluoride salts,” *J. Nucl. Mater.*, 2011, doi: 10.1016/j.jnucmat.2011.01.032.

[95] G. Kresse and J. Furthmüller, “Efficient iterative schemes for ab initio total-energy calculations using a plane-wave basis set,” *Phys. Rev. B*, vol. 54, no. 16, pp. 11169–11186, Oct. 1996, doi: 10.1103/PhysRevB.54.11169.

[96] G. Kresse and D. Joubert, “From ultrasoft pseudopotentials to the projector augmented-wave method,” *Phys. Rev. B*, vol. 59, no. 3, pp. 1758–1775, Jan. 1999, doi: 10.1103/PhysRevB.59.1758.

[97] H. J. Monkhorst and J. D. Pack, “Special points for Brillouin-zone integrations,” *Phys. Rev. B*, vol. 13, no. 12, pp. 5188–5192, Jun. 1976, doi:

10.1103/PhysRevB.13.5188.

[98] G. Kresse and J. Furthmüller, “Efficiency of ab-initio total energy calculations for metals and semiconductors using a plane-wave basis set,” *Comput. Mater. Sci.*, vol. 6, no. 1, pp. 15–50, Jul. 1996, doi: 10.1016/0927-0256(96)00008-0.

[99] G. Kresse and J. Hafner, “Ab initio molecular dynamics for liquid metals,” *Phys. Rev. B*, vol. 47, no. 1, pp. 558–561, Jan. 1993, doi: 10.1103/PhysRevB.47.558.

[100] S. Grimme, “Semiempirical GGA-type density functional constructed with a long-range dispersion correction,” *J. Comput. Chem.*, vol. 27, no. 15, pp. 1787–1799, Nov. 2006, doi: 10.1002/jcc.20495.

[101] S. Grimme, S. Ehrlich, and L. Goerigk, “Effect of the damping function in dispersion corrected density functional theory,” *J. Comput. Chem.*, vol. 32, no. 7, pp. 1456–1465, May 2011, doi: 10.1002/jcc.21759.

[102] S. Grimme, J. Antony, S. Ehrlich, and H. Krieg, “A consistent and accurate *ab initio* parametrization of density functional dispersion correction (DFT-D) for the 94 elements H-Pu,” *J. Chem. Phys.*, vol. 132, no. 15, p. 154104, Apr. 2010, doi: 10.1063/1.3382344.

[103] G. J. Janz, C. B. Allen, N. P. Bansal, R. M. Murphy, and R. P. T. Tomkins, “Physical properties data compilations relevant to energy storage :,” Gaithersburg, MD, 1979. doi: 10.6028/NBS.NSRDS.61p2.

[104] M. Parrinello and A. Rahman, “Crystal Structure and Pair Potentials: A Molecular-Dynamics Study,” *Phys. Rev. Lett.*, vol. 45, no. 14, pp. 1196–1199, Oct. 1980, doi:

10.1103/PhysRevLett.45.1196.

[105] M. Parrinello and A. Rahman, “Polymorphic transitions in single crystals: A new molecular dynamics method,” *J. Appl. Phys.*, vol. 52, no. 12, pp. 7182–7190, Dec. 1981, doi: 10.1063/1.328693.

[106] M. P. Allen and D. J. Tildesley, *Computer Simulation of Liquids*, vol. 1. Oxford University Press, 2017.

[107] H. Ito, Y. Hasegawa, and Y. Ito, “Densities of eutectic mixtures of molten alkali chlorides below 673 K,” *J. Chem. Eng. Data*, vol. 46, no. 5, pp. 1203–1205, 2001, doi: 10.1021/je010092n.

[108] M. Rupp, A. Tkatchenko, K. R. Müller, and O. A. Von Lilienfeld, “Fast and accurate modeling of molecular atomization energies with machine learning,” *Phys. Rev. Lett.*, vol. 108, no. 5, p. 058301, Jan. 2012, doi: 10.1103/PhysRevLett.108.058301.

[109] Y. Huang, J. Kang, W. A. Goddard, and L.-W. Wang, “Density functional theory based neural network force fields from energy decompositions,” *Phys. Rev. B*, vol. 99, no. 6, p. 064103, Feb. 2019, doi: 10.1103/PhysRevB.99.064103.

[110] L. Zhang, J. Han, H. Wang, R. Car, and E. Weinan, “Deep Potential Molecular Dynamics: A Scalable Model with the Accuracy of Quantum Mechanics,” *Phys. Rev. Lett.*, vol. 120, no. 14, p. 143001, Apr. 2018, doi: 10.1103/PhysRevLett.120.143001.

[111] J. Han, L. Zhang, R. Car, and W. E, “Deep Potential: A General Representation of

a Many-Body Potential Energy Surface," *Commun. Comput. Phys.*, vol. 23, no. 3, pp. 629–639, Jul. 2018, doi: 10.4208/cicp.OA-2017-0213.

[112] S. Chmiela, A. Tkatchenko, H. E. Sauceda, I. Poltavsky, K. T. Schütt, and K.-R. Müller, "Machine learning of accurate energy-conserving molecular force fields," *Sci. Adv.*, vol. 3, no. 5, p. e1603015, May 2017, doi: 10.1126/sciadv.1603015.

[113] K. Yao, J. E. Herr, S. N. Brown, and J. Parkhill, "Intrinsic Bond Energies from a Bonds-in-Molecules Neural Network," *J. Phys. Chem. Lett.*, vol. 8, no. 12, pp. 2689–2694, Jun. 2017, doi: 10.1021/acs.jpclett.7b01072.

[114] J. Behler and M. Parrinello, "Generalized Neural-Network Representation of High-Dimensional Potential-Energy Surfaces," *Phys. Rev. Lett.*, vol. 98, no. 14, p. 146401, Apr. 2007, doi: 10.1103/PhysRevLett.98.146401.

[115] G. Pan, P. Chen, H. Yan, and Y. Lu, "A DFT accurate machine learning description of molten ZnCl2 and its mixtures: 1. Potential development and properties prediction of molten ZnCl2," *Comput. Mater. Sci.*, vol. 185, p. 109955, Dec. 2020, doi: 10.1016/j.commatsci.2020.109955.

[116] W. Liang, G. Lu, and J. Yu, "Theoretical prediction on the local structure and transport properties of molten alkali chlorides by deep potentials," *J. Mater. Sci. Technol.*, vol. 75, pp. 78–85, Jun. 2021, doi: 10.1016/j.jmst.2020.09.040.

[117] Q.-J. Li, E. Küçükbenli, S. Lam, B. Khaykovich, E. Kaxiras, and J. Li, "Development of robust neural-network interatomic potential for molten salt," *Cell Reports Phys. Sci.*, vol. 2, no. 3, p. 100359, Mar. 2021, doi:

10.1016/j.xcrp.2021.100359.

[118] W. Liang, J. Wu, H. Ni, G. Lu, and J. Yu, “First-principles molecular dynamics simulations on the local structure and thermo-kinetic properties of molten magnesium chloride,” *J. Mol. Liq.*, vol. 298, p. 112063, 2020, doi: 10.1016/j.molliq.2019.112063.

[119] H. O. Nam, A. Bengtson, K. Vörtler, S. Saha, R. Sakidja, and D. Morgan, “First-principles molecular dynamics modeling of the molten fluoride salt with Cr solute,” *J. Nucl. Mater.*, vol. 449, no. 1–3, pp. 148–157, 2014, doi: 10.1016/j.jnucmat.2014.03.014.

[120] L. Zhang, J. Han, H. Wang, W. A. Saidi, R. Car, and W. E, “End-to-end Symmetry Preserving Inter-atomic Potential Energy Model for Finite and Extended Systems,” *32nd Conf. Neural Inf. Process. Syst. (NeurIPS 2018), Montréal, Canada.*, vol. 2018-Decem, pp. 4441–4451, May 2018, Accessed: Mar. 09, 2021. [Online]. Available: http://www.deepmd.org/database/deeppot-se-data/.

[121] G. Henkelman and H. Jónsson, “Improved tangent estimate in the nudged elastic band method for finding minimum energy paths and saddle points,” *J. Chem. Phys.*, vol. 113, no. 22, pp. 9978–9985, 2000, doi: 10.1063/1.1323224.

[122] G. Henkelman, B. P. Uberuaga, and H. Jónsson, “Climbing image nudged elastic band method for finding saddle points and minimum energy paths,” *J. Chem. Phys.*, vol. 113, no. 22, pp. 9901–9904, 2000, doi: 10.1063/1.1329672.

[123] J. Kästner and P. Sherwood, “Superlinearly converging dimer method for

transition state search," *J. Chem. Phys.*, vol. 128, no. 1, p. 014106, Jan. 2008, doi: 10.1063/1.2815812.

[124] G. Henkelman and H. Jónsson, "A dimer method for finding saddle points on high dimensional potential surfaces using only first derivatives," *J. Chem. Phys.*, vol. 111, no. 15, pp. 7010–7022, 1999, doi: 10.1063/1.480097.

[125] S. Baroni, S. De Gironcoli, A. Dal Corso, and P. Giannozzi, "Phonons and related crystal properties from density-functional perturbation theory," *Reviews of Modern Physics*. 2001, doi: 10.1103/RevModPhys.73.515.

[126] S. Curtarolo, G. L. W. Hart, M. B. Nardelli, N. Mingo, S. Sanvito, and O. Levy, "The high-throughput highway to computational materials design," *Nat. Mater.*, vol. 12, no. 3, pp. 191–201, 2013, doi: 10.1038/nmat3568.

[127] A. Jain *et al.*, "A high-throughput infrastructure for density functional theory calculations," *Comput. Mater. Sci.*, vol. 50, no. 8, pp. 2295–2310, 2011, doi: 10.1016/j.commatsci.2011.02.023.

[128] O. Levy, G. L. W. Hart, and S. Curtarolo, "Uncovering compounds by synergy of cluster expansion and high-throughput methods," *J. Am. Chem. Soc.*, vol. 132, no. 13, pp. 4830–4833, 2010, doi: 10.1021/ja9105623.

[129] K. F. Garrity, J. W. Bennett, K. M. Rabe, and D. Vanderbilt, "Pseudopotentials for high-throughput DFT calculations," *Comput. Mater. Sci.*, vol. 81, pp. 446–452, 2014, doi: 10.1016/j.commatsci.2013.08.053.

[130] W. Setyawan and S. Curtarolo, "High-throughput electronic band structure

calculations: Challenges and tools," *Comput. Mater. Sci.*, vol. 49, no. 2, pp. 299–312, 2010, doi: 10.1016/j.commatsci.2010.05.010.

[131] D. Morgan, G. Ceder, and S. Curtarolo, "High-throughput and data mining with ab initio methods," *Meas. Sci. Technol.*, vol. 16, no. 1, pp. 296–301, 2005, doi: 10.1088/0957-0233/16/1/039.

[132] S. Maintz, V. L. Deringer, A. L. Tchougréeff, and R. Dronskowski, "LOBSTER: A tool to extract chemical bonding from plane-wave based DFT," *J. Comput. Chem.*, vol. 37, no. 11, pp. 1030–1035, 2016, doi: 10.1002/jcc.24300.

[133] R. Dronskowski and P. E. Blöchl, "Crystal orbital hamilton populations (COHP). Energy-resolved visualization of chemical bonding in solids based on density-functional calculations," *J. Phys. Chem.*, vol. 97, no. 33, pp. 8617–8624, 1993, doi: 10.1021/j100135a014.

[134] V. L. Deringer, A. L. Tchougréeff, and R. Dronskowski, "Crystal orbital Hamilton population (COHP) analysis as projected from plane-wave basis sets," *J. Phys. Chem. A*, vol. 115, no. 21, pp. 5461–5466, 2011, doi: 10.1021/jp202489s.

[135] S. Maintz, V. L. Deringer, A. L. Tchougréeff, and R. Dronskowski, "Analytic projection from plane-wave and PAW wavefunctions and application to chemical-bonding analysis in solids," *J. Comput. Chem.*, vol. 34, no. 29, pp. 2557–2567, 2013, doi: 10.1002/jcc.23424.

[136] S. Steinberg, J. Brgoch, G. J. Miller, and G. Meyer, "Identifying a structural preference in reduced rare-earth metal halides by combining experimental and

computational techniques," *Inorg. Chem.*, vol. 51, no. 21, pp. 11356–11364, 2012, doi: 10.1021/ic300838a.

[137] K. C. Göbgen, S. Steinberg, and R. Dronskowski, "Revisiting the Si-Te System: SiTe 2 Finally Found by Means of Experimental and Quantum-Chemical Techniques," *Inorg. Chem.*, vol. 56, no. 18, pp. 11398–11405, 2017, doi: 10.1021/acs.inorgchem.7b01847.

[138] J. Li and C. Fan, "Novel metastable compounds in the Zr-B system: An ab initio evolutionary study," *Phys. Chem. Chem. Phys.*, vol. 17, no. 2, pp. 1180–1188, 2015, doi: 10.1039/c4cp04185b.

[139] S. Steinberg and R. Dronskowski, "The Crystal Orbital Hamilton Population (COHP) Method as a Tool to Visualize and Analyze Chemical Bonding in Intermetallic Compounds," *Crystals*, vol. 8, no. 5, p. 225, May 2018, doi: 10.3390/cryst8050225.

[140] R. Babar and M. Kabir, "Transition Metal and Vacancy Defect Complexes in Phosphorene: A Spintronic Perspective," *J. Phys. Chem. C*, vol. 120, no. 27, pp. 14991–15000, 2016, doi: 10.1021/acs.jpcc.6b05069.

[141] Z. T. Y. Liu, D. Gall, and S. V. Khare, "Electronic and bonding analysis of hardness in pyrite-type transition-metal pernitrides," *Phys. Rev. B - Condens. Matter Mater. Phys.*, vol. 90, no. 13, pp. 1–11, 2014, doi: 10.1103/PhysRevB.90.134102.

[142] G. Cocco, L. Schiffini, A. Lucci, and C. Antonione, "RDF analysis of structural

evolution during the primary crystallization of the Fe40Ni38Mo4B18 glassy alloy," *J. Non. Cryst. Solids*, vol. 50, no. 3, pp. 359–369, 1982, doi: 10.1016/0022-3093(82)90096-5.

[143] B. G. Levine, J. E. Stone, and A. Kohlmeyer, "Fast analysis of molecular dynamics trajectories with graphics processing units-Radial distribution function histogramming," *J. Comput. Phys.*, vol. 230, no. 9, pp. 3556–3569, 2011, doi: 10.1016/j.jcp.2011.01.048.

[144] S. Tovey *et al.*, "DFT Accurate Interatomic Potential for Molten NaCl from Machine Learning," *J. Phys. Chem. C*, 2020, doi: 10.1021/acs.jpcc.0c08870.

[145] P. A. Egelstaff, *An Introduction to the Liquid State*, 2nd Editio. Elsevier, 1967.

[146] N. H. March and M. P. Tosi, *Introduction to Liquid State Physics*. WORLD SCIENTIFIC, 2002.

[147] C. Hoheisel, *Theoretical Treatment of Liquids and Liquid Mixtures*. New York: Elsevier, Amsterdam, 1993.

[148] J. P. Hansen and I. R. McDonald, *Theory of Simple Liquids*, 2nd Editio. Elsevier, 2006.

[149] M. Mouas, J. G. Gasser, S. Hellal, B. Grosdidier, A. Makradi, and S. Belouettar, "Diffusion and viscosity of liquid tin: Green-Kubo relationship-based calculations from molecular dynamics simulations," *J. Chem. Phys.*, vol. 136, no. 9, 2012, doi: 10.1063/1.3687243.

[150] S. T. Lin, M. Blanco, and W. A. Goddard, "The two-phase model for calculating

thermodynamic properties of liquids from molecular dynamics: Validation for the phase diagram of Lennard-Jones fluids," *J. Chem. Phys.*, vol. 119, no. 22, pp. 11792–11805, 2003, doi: 10.1063/1.1624057.

[151] S.-T. Lin, P. K. Maiti, and W. A. Goddard, "Two-Phase Thermodynamic Model for Efficient and Accurate Absolute Entropy of Water from Molecular Dynamics Simulations," *J. Phys. Chem. B*, vol. 114, no. 24, pp. 8191–8198, Jun. 2010, doi: 10.1021/jp103120q.

[152] T. A. Pascal, S. T. Lin, and W. A. Goddard, "Thermodynamics of liquids: Standard molar entropies and heat capacities of common solvents from 2PT molecular dynamics," *Phys. Chem. Chem. Phys.*, vol. 13, no. 1, pp. 169–181, 2011, doi: 10.1039/c0cp01549k.

[153] D. Eisenberg and W. Kauzmann, *The Structure and Properties of Water*. Oxford University Press, 2005.

[154] J. C. Jamieson and C. Olinger., "Zirconium: phases and compressibility to 120 kilobars," *High Temp. Press.*, vol. 5, pp. 123–131, 1973, [Online]. Available: https://htracyhall.org/ocr/HTH-Archives/Cabinet 8/Drawer 4 (MP-OL)/(Olinger, B.) (Oliver, B.G.) (Oliver, M.R.) (linked)/(Olinger, B.) (Oliver, B.G.) (Oliver, M.R.)-133_OCR.pdf.

[155] "Neutron Cross Section for all the elements in the Periodic Table." https://periodictable.com/Properties/A/NeutronCrossSection.html (accessed Dec. 21, 2019).

[156] H. Okamoto, “The Bi-Zr (Bismuth-Zirconium) system,” *Bull. Alloy Phase Diagrams*, vol. 11, no. 3, pp. 295–297, 1990, doi: 10.1007/BF03029301.

[157] E. R. Van Artsdalen and I. S. Yaffe, “Electrical conductance and density of molten salt systems: KCl-LiCl, KCl-NaCl and KCl-KI,” *J. Phys. Chem.*, vol. 59, no. 2, pp. 118–127, 1955, doi: 10.1021/j150524a007.

[158] G. J. Janz, C. B. Allen, N. P. Bansal, R. M. Murphy, and R. P. T. Tomkins, “PHYSICAL PROPERTIES DATA COMPILATIONS RELEVANT TO ENERGY STORAGE - 2. MOLTEN SALTS: DATA ON SINGLE AND MULTI-COMPONENT SALT SYSTEMS.,” *Natl. Bur. Stand. Natl. Stand. Ref. Data Ser.*, 1979.

[159] I. Okada, H. Okano, H. Ohtaki, and R. Takagi, “Structural determination of a molten (Li-K)Cl mixture of the eutectic composition by x-ray diffraction and molecular dynamics simulation,” *Chem. Phys. Lett.*, vol. 100, no. 5, pp. 436–441, Aug. 1983, doi: 10.1016/0009-2614(83)87344-8.

[160] S. K. Gill *et al.*, “Connections between the Speciation and Solubility of Ni(II) and Co(II) in Molten ZnCl 2,” *J. Phys. Chem. B*, vol. 124, no. 7, pp. 1253–1258, Feb. 2020, doi: 10.1021/acs.jpcb.0c00195.

[161] B. R. Sundheim and G. Harrington, “Absorption Spectrum of NiCl 2 in Molten LiCl/KCl,” *J. Chem. Phys.*, vol. 31, no. 3, pp. 700–701, Sep. 1959, doi: 10.1063/1.1730448.

[162] E. Ed Vitz, J. M. Moore, J. Shorb, X. Prat-Resina, T. Wendorff, and Hahn Adam,

"Heat Capacity and Microscopic Changes," *Chemical Education Digital Library*. https://chem.libretexts.org/Bookshelves/General_Chemistry/Book%3A_ChemPRIME_(Moore_et_al.)/15%3A_Thermodynamics-_Atoms_Molecules_and_Energy/15.03%3A_Heat_Capacity_and_Microscopic_Changes (accessed Mar. 25, 2021).

[163] J.-Y. Kim, S.-E. Bae, D.-H. Kim, Y. S. Choi, J.-W. Yeon, and K. Song, "High-Temperature Viscosity Measurement of LiCl-KCl Molten Salts Comprising Actinides and Lanthanides," *Bull. Korean Chem. Soc.*, vol. 33, no. 11, pp. 3871–3874, Nov. 2012, doi: 10.5012/bkcs.2012.33.11.3871.

[164] Q.-L. Cao, F. Tu, L. Xue, and F.-H. Wang, "Assessing relationships between self-diffusion coefficient and viscosity in Ni-Al alloys based on the pair distribution function," *J. Appl. Phys.*, vol. 126, no. 10, p. 105108, Sep. 2019, doi: 10.1063/1.5109598.

[165] J. Brillo, A. I. Pommrich, and A. Meyer, "Relation between Self-Diffusion and Viscosity in Dense Liquids: New Experimental Results from Electrostatic Levitation," 2011, doi: 10.1103/PhysRevLett.107.165902.